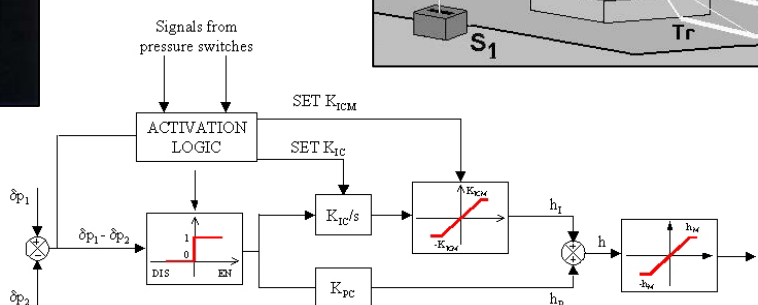
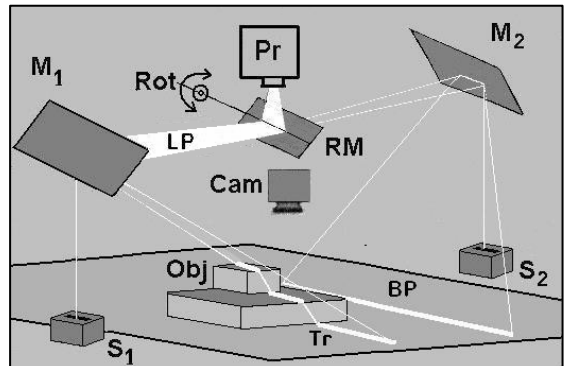
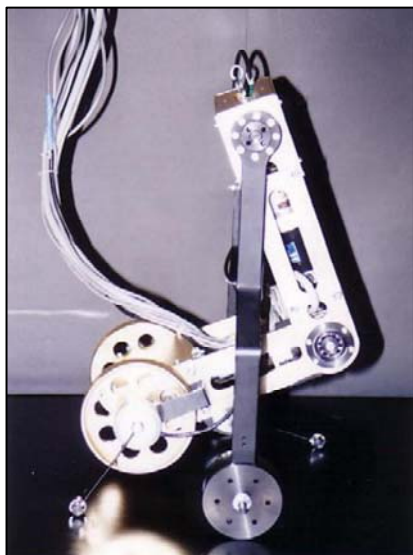


International Journal of Mechanics and Control

Honorary Editor: Guido Belforte

Editor: Andrea Manuello Bertetto



Editorial Board of the
International Journal of Mechanics and Control

Published by Levrotto&Bella – Torino – Italy E.C.

Honorary editors

Guido Belforte

Atlas Akhmetzyanov
V.A.Trapeznikov Institute of Control Sciences
of Russian Academy of Sciences
Moscow – Russia

Domenico Appendino
Prima Industrie
Torino – Italy

Kenji Araki
Saitama University
Shimo Okubo, Urawa
Saitama – Japan

Guido Belforte
Technical University – Politecnico di Torino
Torino – Italy

Bruno A. Boley
Columbia University,
New York – USA

Marco Ceccarelli
LARM at DIMSAT
University of Cassino
Cassino – Italy

Amalia Ercoli Finzi
Technical University – Politecnico di Milano
Milano – Italy

Carlo Ferraresi
Technical University – Politecnico di Torino
Torino – Italy

Anindya Ghoshal
Arizona State University
Tempe – Arizona – USA

Nunziatino Gualtieri
Space System Group
Alenia Spazio
Torino – Italy

Alexandre Ivanov
Technical University – Politecnico di Torino
Torino – Italy

Giovanni Jacazio
Technical University – Politecnico di Torino
Torino – Italy

Takashi Kawamura
Shinshu University
Nagano – Japan

Kazy Yamafuji

Editor: Andrea Manuello Bertetto

General Secretariat: Elvio Bonisoli

Kin Huat Low
School of Mechanical and Aerospace Engineering
Nanyang Technological University
Singapore

Andrea Manuello Bertetto
University of Cagliari
Cagliari – Italy

Stamos Papastergiou
Jet Joint Undertaking
Abingdon – United Kingdom

Mihailo Ristic
Imperial College
London – United Kingdom

János Somló
Technical University of Budapest
Budapest – Hungary

Jozef Suchý
Faculty of Natural Science
Banská Bystrica – Slovakia

Federico Thomas
Instituto de Robótica e Informática Industrial
(CSIC-UPC)
Barcelona – Espana

Lubomir Uher
Institute of Control Theory and Robotics
Bratislava – Slovakia

Furio Vatta
Technical University – Politecnico di Torino
Torino – Italy

Vladimir Viktorov
Technical University – Politecnico di Torino
Torino – Italy

Kazy Yamafuji
University of Electro-Communications
Tokyo – Japan

Official Torino Italy Court Registration
n.5390, 5th May 2000

Deposito presso il Tribunale di Torino
numero 5390 del 5 maggio 2000
Direttore responsabile:

Andrea Manuello Bertetto

International Journal of Mechanics and Control

Editor: **Andrea Manuello Bertetto**

Honorary editors: **Guido Belforte**
Kazy Yamafuji

General Secretariat: **Elvio Bonisoli**

The Journal is addressed to scientists and engineers who work in the fields of mechanics (mechanics, machines, systems, control, structures). It is edited in Turin (Northern Italy) by Levrotto&Bella Co., with an international board of editors. It will have not advertising.

Turin has a great and long tradition in mechanics and automation of mechanical systems. The journal would will to satisfy the needs of young research workers of having their work published on a qualified paper in a short time, and of the public need to read the results of researches as fast as possible.

Interested parties will be University Departments, Private or Public Research Centres, Innovative Industries.

Aims and scope

The *International Journal of Mechanics and Control* publishes as rapidly as possible manuscripts of high standards. It aims at providing a fast means of exchange of ideas among workers in Mechanics, at offering an effective method of bringing new results quickly to the public and at establishing an informal vehicle for the discussion of ideas that may still in the formative stages.

Language: English

International Journal of Mechanics and Control will publish both scientific and applied contributions. The scope of the journal includes theoretical and computational methods, their applications and experimental procedures used to validate the theoretical foundations. The research reported in the journal will address the issues of new formulations, solution, algorithms, computational efficiency, analytical and computational kinematics synthesis, system dynamics, structures, flexibility effects, control, optimisation, real-time simulation, reliability and durability. Fields such as vehicle dynamics, aerospace technology, robotics and mechatronics, machine dynamics, crashworthiness, biomechanics, computer graphics, or system identification are also covered by the journal.

Please address contributions to

Prof. Guido Belforte
Prof. Andrea Manuello Bertetto
PhD Eng. Elvio Bonisoli

Dept. of Mechanics
Technical University - Politecnico di Torino
C.so Duca degli Abruzzi, 24.
10129 - Torino - Italy - E.C.

www.jomac.it
e_mail: jomac@polito.it

Subscription information

Subscription order must be sent to
the publisher:

Libreria Editrice Universitaria
Levrotto&Bella
2/E via Pigafetta – 10129 Torino – Italy

www.levrotto-bella.net
e_mail: info@levrotto-bella.net
tel. +39.011.5097367
+39.011.5083690
fax +39.011.504025

ROBOTS DRIVEN BY PARALLEL BICYCLES

Kazuo Yamafuji*, Maria Q. Feng** and Takashi Kawamura***

* University of Electro-Communications, Japan, 156-0043

** Dept. of Civil and Environmental Engineering, University of California, Irvine, CA 92697-2175 USA

*** Dept. of Functional Machinery and Mechanics, Shinshu University, 3-15-1 Tokida Ueda, Nagano, Japan, 386-8565

ABSTRACT

This paper reviews the research, development, and application of robots driven by parallel bicycles, referred to as PB robots, including six prototypes developed by the authors. The first one, developed in 1986, is composed of a pair of coaxial wheels and an inverted pendulum body standing on the wheel axis. As the wheels move toward a target, the pendulum body must be stabilized to maintain its upright posture. Two mechanisms are developed for controlling the pendulum posture: one controls the lower end of the pendulum, while the other displaces an additional mass (arm) to counterbalance the pendulum. The latter resembles a tumbler. Simple but effective control rules are proposed. If the PB robot is equipped with a pair of arms, one of them can be used to perform a task, while the other to control the posture of the body. The PB robots can be transformed into different configurations for different applications. Upon presenting a variety of mechanisms, control algorithms, and prototype development, this paper reviews the applications of PB robots including the first successful commercialization by Segway in personal transporters and the most notable application in the mobile mechanism of humanoids by TOYOTA.

Keywords: parallel bicycle, robot, inverted pendulum, posture control, tumbler, transformation, personal transporters, humanoid.

1 INTRODUCTION

Posture control of an inverted pendulum has long been one of the research interests in control engineering [1]. The authors started research on a unicycle with an inverted pendulum body in 1985 through computer simulation [2] and experiments [3]. Although the developed unicycle pendulum could hold the standing upright posture for 12-13 seconds, it lacked robustness when the wheel was driven to a target. By improving the design of the unicycle mechanisms and increasing the microcomputer speed, the authors achieved stabilization of the unicycle robot with a high robustness [4-7].

In 1986, the authors shifted research to a PB robot that consisted of a pair of coaxial wheels and an inverted pendulum body. The wheels were installed on the both sides of the pivot axis of the inverted pendulum. The side view of a PB is the same as the unicycle, but the PB is obviously simpler because of its stability in the transverse direction. Later arms were added on the upper PB body for the posture control, so that the wheels can be independently driven to a target. Furthermore, the PB robots were transformed into different configurations for performing different tasks. This paper reviews the research and development of a variety of PB robots and then their applications in personal transporters and humanoids.

Contact author: Kazuo Yamafuji

3-10-14 Matsubara, Setagaya, Tokyo 156-0043, Japan
E-mail: kazyama@r2.dion.ne.jp

2 POSTURE CONTROL OF PB ROBOTS: PROTOTYPES P-1 AND P-2

For holding an inverted pendulum or a PB robot at its upright position, there are two kinds of control mechanisms as illustrated in Figure 1 [8]. One is to move the fulcrum of the pendulum forward or backward depending on its inclination (Figure 1(a)). The other is to counterbalance the fall-down moment by rotating or displacing an additional mass (arm) to the opposite direction of the inclination (Figure 1(b)). The former controls the posture by means of moving the fulcrum with a wire or wheels, while the latter utilizes the inertial force of the additional mass. Yamafuji and Feng [9] and Yamafuji and Kawamura [10] developed prototype PB robots P-1 and P-2 in 1986, respectively controlled by these two mechanisms.

2.1 PROTOTYPES P-1 AND P-2

Figure 2 shows P-2, whose inverted pendulum body is pivoted by the wheel axis between the two wheels. The axis is driven by DC servomotor 1 through reduction gears. A single arm with a weight is suspended inside the upper body and driven by DC servomotor 2 for controlling the posture of the pendulum body. In order to detect the inclinational angle of the body with respect to the floor, a magnetic rotary encoder is installed, as shown in Figure 2, from which two reference rods are extended contacting the floor. The PB robot was controlled by a personal computer (CPU i8086, 4MHz) and the control software is written in C-language. This prototype is referred to as P-1 when the arm is removed and the body posture is controlled by moving the wheels, as described in Figure 1(a).

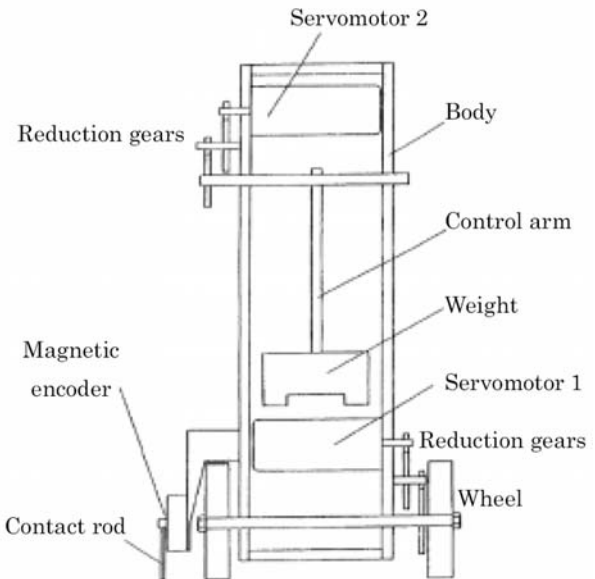


Figure 2 Parallel Bicycle Prototype P-1.

2.2 POSTURE CONTROL OF P-1 USING WHEELS

The authors succeeded in stabilizing the P-1 robot body by moving the wheels (without utilizing the arm). The postural stability of the robot was experimentally demonstrated [10, 11]. P-1 is modeled by an inverted pendulum shown in Figure 3 and the equation of motion is given in Equation (1) assuming a small inclinational angle of the body.

$$J\ddot{\theta}_1(t) + C\dot{\theta}_1(t) - mgl\theta_1(t) = U(t) \quad (1)$$

where J is inertial moment of the pendulum around the rotation center, θ_1 is inclinational angle, C is coefficient of viscous friction, m is mass, g is gravity acceleration, l is length, and $U(t)$ is control input.

Utilizing the proportional control law and considering the time delay T in the control system, the control input is determined as shown in Equation (2),

$$U(t) = -\xi K\theta_1(t-T) \quad (2)$$

where K is proportional gain, ξ is torque conversion coefficient of the motor, and T is the time delay. From Equation (1) and Taylor expansion of Equation (2), Equation (3) is derived by neglecting the higher order terms.

$$J\ddot{\theta}_1(t) + (C - K\xi T)\dot{\theta}_1(t) + (K\xi - mgl)\theta_1(t) = 0 \quad (3)$$

According to the Routh-Hurwitz's criterion, the system is stable as long as Equation (4) is satisfied [10].

$$\frac{mgl}{\xi} < K < \frac{C}{\xi T} \quad (4)$$

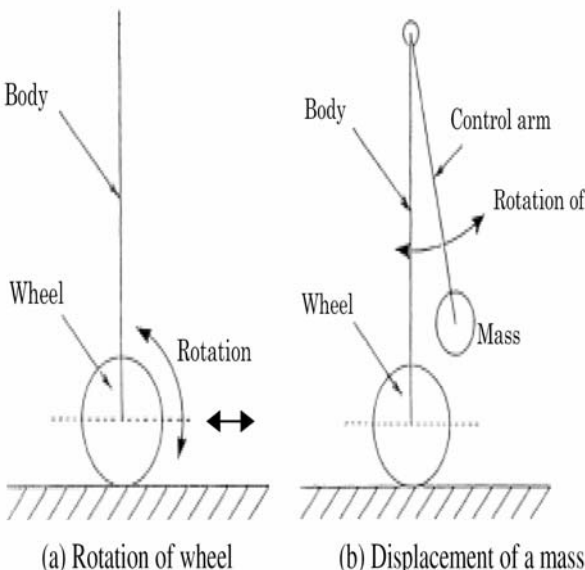


Figure 1 Control methods for PB robots.

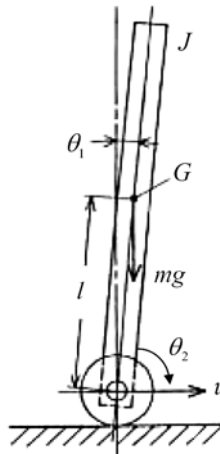
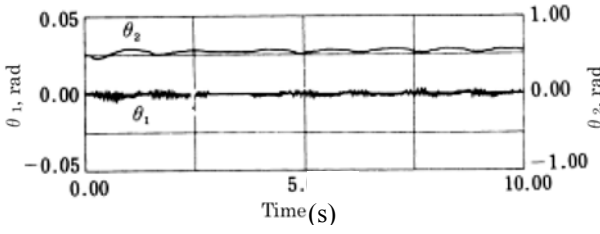


Figure 3 Model of P-1.



(a) Time history of θ_1 and θ_2

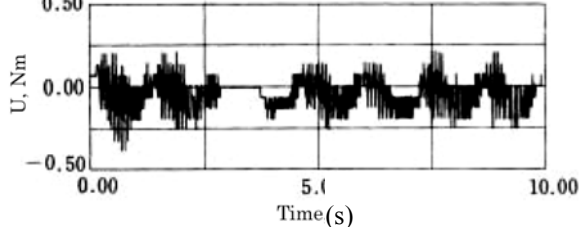


Figure 4 Experimental result at $T_s = 3$ ms, $K = 10.0$.

Equation (4) implies that the lower limit of K is constant but the upper limit varies depending on T .

Using the sampling interval T_s as the time delay T , feedback gain K is computed according to Equation (4), with which experiments were conducted. Figure 4(a) shows plots of the time histories of the inclinational angle θ_1 of the body and rotational angle θ_2 of the wheels measured from the experiment at $T_s = 3$ ms and $K = 10.0$. It is demonstrated that the inclinational angle of the robot body can be maintained within a small range. The control input is shown in Figure 4(b).

A large number of feedback gain K values are tested for the control performance and stability. The experimental results are plotted in Figure 5, together with the stability boundaries of K calculated by Equation (4) as a function of time delay. Although some discrepancies exist between the experimental and analytical boundaries (due to, e.g., neglecting of the higher order terms in Equation (3)), Equation (4) does provide a good guidance for selecting K .

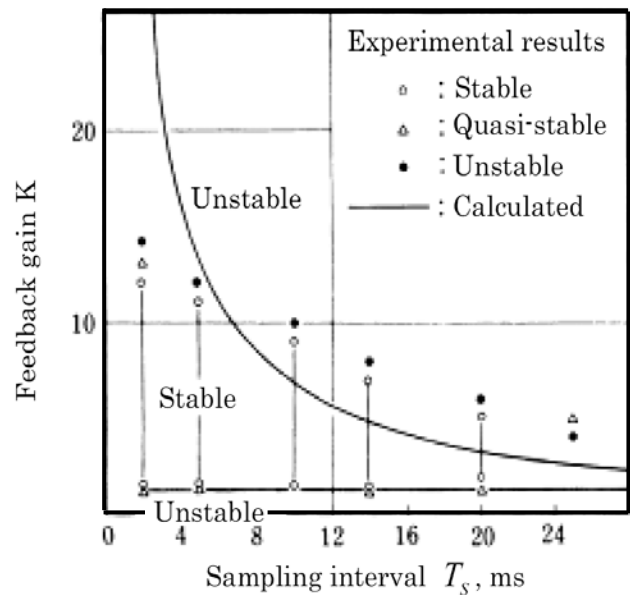


Figure 5 Relations between feedback gain and sampling interval.

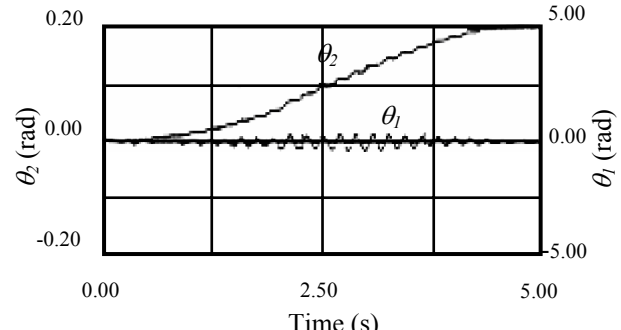


Figure 6 Experimental results from posture and driving control.

Furthermore, Yamafuji, Feng and Kawamura [9-11] succeeded in controlling the wheels to drive the robot to a target location and at the same time to control the posture of the pendulum body. Figure 6 shows experimental results of driving the robot to a target as plotted in θ_2 , while maintaining the robot body upright as plotted in θ_1 [10]. Prototype P-1 was patented [12] in 1996. Since prototype P-1 cannot turn because of its coaxial wheels, Yamafuji, Miyagawa and Kawamura [13] developed its variation which has double axles equipped a wheel on each axle. The study results of prototype P-2 [9] is not presented in this paper since it is similar to P-3 as follows.



Figure 7 PB robot with arms: P-3.

3 POSTURE RESTORATION OF PB ROBOT: PROTOTYPE P-3

In 1988 Hirabayashi and Yamafuji [14] developed a prototype PB robot, P-3. As shown in Figure 7, P-3 is equipped with double arms on the both side of the inverted pendulum body, resembling a human being. The arms are driven by a motor and the wheels are driven by a different motor. Since the body posture is controlled by the double arms, the wheels can be independently used for locomotion.

3.1 PRINCIPLE OF POSTURE RESTORATION USING ARMS

P-3 is modeled by double inverted links and wheels as shown in Figure 8(a). In this model, it is more convenient to consider the compound center of gravity of the robot as a variable parameter, rather than the inclinational angles of the links.

In order to stabilize the posture of the robot body, a restoration torque must be generated by moving the compound center of gravity of the robot. The concept is the same as restoration of a tumbler's posture as shown in Figure 8(b) [14]. If r_t is the distance between center of curvature of the tumbler and center of gravity, its projection on the floor is

$$X_{gt} = r_t \sin(\Delta\theta_t) \cong r_t \Delta\theta_t \quad (5)$$

where, $\Delta\theta_t = \pi/2 - \theta_t$, X_{gt} is projection of r_t on the floor, and $\Delta\theta_t$ is inclinational angle of the tumbler.

The restoration torque about the contact point against the tumbler of mass M_t is the product of the distance X_{gt} and the gravity force $M_t g$ as follows:

$$T_{rct} = M_t g X_{gt} = M_t r_t g \Delta\theta_t \quad (6)$$

Namely, if the restoration torque T_{rct} proportional to the body's inclinational angle $\Delta\theta_t$ can be generated, the robot's posture can be restored based on the principle of the tumbler.

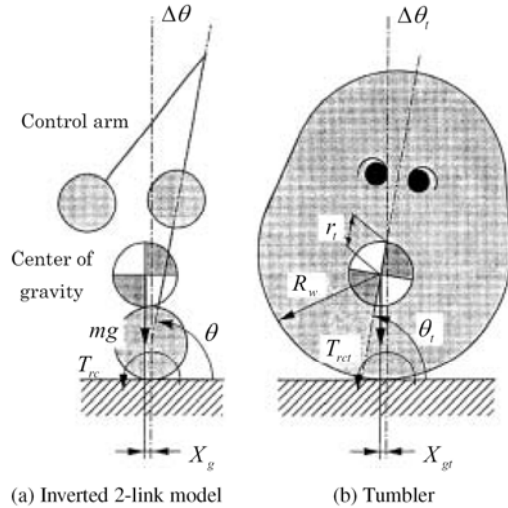


Figure 8 Comparison of posture restoration of an inverted 2-link model and a tumbler.

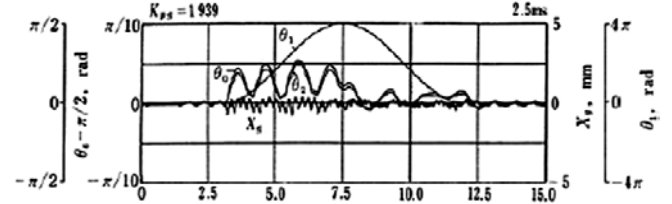


Figure 9 Locomotion on a slope using the CGFC control.

Applying this principle to the PB robot with double arms, the compound center of gravity of the system proportional to the inclined angle can be generated by rotating the arms as shown in Figure 8(a).

3.2 COMPOUND CENTER OF GRAVITY FEEDBACK CONTROL

In order to stabilize the PB robot posture, the compound center of gravity feedback control rule (CGFC) was developed [14]. The CGFC input is given by Equation (7).

$$U_2 = U_{pgc} + U_{gc} \quad (7)$$

Where, U_{pgc} is control input to restore the compound center of gravity of the robot back to the equilibrium position (namely, the contact point of the robot with the ground), and U_{gc} is for gravity compensation.

Experimental study was performed to examine the effectiveness of this control rule. Figure 9 shows an experimental result from a round trip made by P-3 on a slope of 10° [14]. P-3 maintained a high level of stability during the trip as demonstrated in the small (less than 1.0

mm) displacement X_g of the center of gravity. Maximum speed and acceleration were 194.8 mm/s and 163.2 mm/s², respectively [15]. In the figure, θ_0 is body inclination angle, θ_1 is rotational angle of the wheels, θ_2 is rotational angle of the arms, and X_g is displacement of the compound center of gravity from the contact point. Figure 10 demonstrates P-3 successfully ascending on a slope of an unknown shape with a maximum slope of 30° [16].

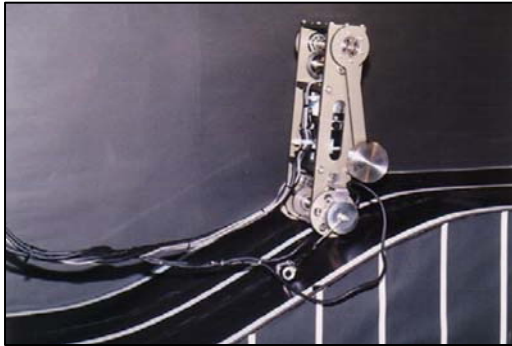


Figure 10 P-3 ascending on an unknown slope.

3.3 DYNAMIC COMPENSATION

The posture restoration control presented in Section 3.2 is based on the static equilibrium, and thus is suitable when the PB robot is moving in a constant speed or a very low acceleration. When the PB robot accelerates or decelerates, dynamic compensation becomes necessary [17, 18]. When the robot moves in acceleration $R_w \dot{\theta}_1$ the dynamic equilibrium of the inertial torque T_i and the gravity torque T_g exerting on the robot is expressed by Equation (8) [18],

$$T_i + T_g = -(m_1 + m_2)R_w Y_g \ddot{\theta}_1 + (m_1 + m_2)g X_g = 0 \quad (8)$$

$$\text{Thus } X_g = \frac{R_w Y_g}{g} \ddot{\theta}_1 \cong K \ddot{\theta}_1 \quad (9)$$

where R_w is radius of the wheel, $\ddot{\theta}_1$ is the acceleration of the wheel, m_1 is the mass of the body, m_2 is the mass of the arms, and (X_g, Y_g) is the compound center of gravity.

The CGFC rule with the dynamic compensation is given by Equation (10).

$$U_2 = U_{pgm} + U_{gc} \quad (10)$$

where:

$$U_{pgm} = -K_{pg} (X_0 - X_{off} + X_{mv}) - K_{dg} \dot{X}_g$$

$$X_{mv} = K \ddot{\theta}_{1r} = \frac{R_w Y_g}{g} \ddot{\theta}_{1r}$$

The above $\ddot{\theta}_{1r}$ is computed using the reference drive path indicating the acceleration and deceleration intervals, and the inertial torque is compensated in a feed-forward manner. Figures 11(a) and (b) show experimental results

when the robot was driven at a maximum acceleration of 6.52 m/s² through a distance of 700 mm, demonstrating the effectiveness of the dynamic compensation [18].

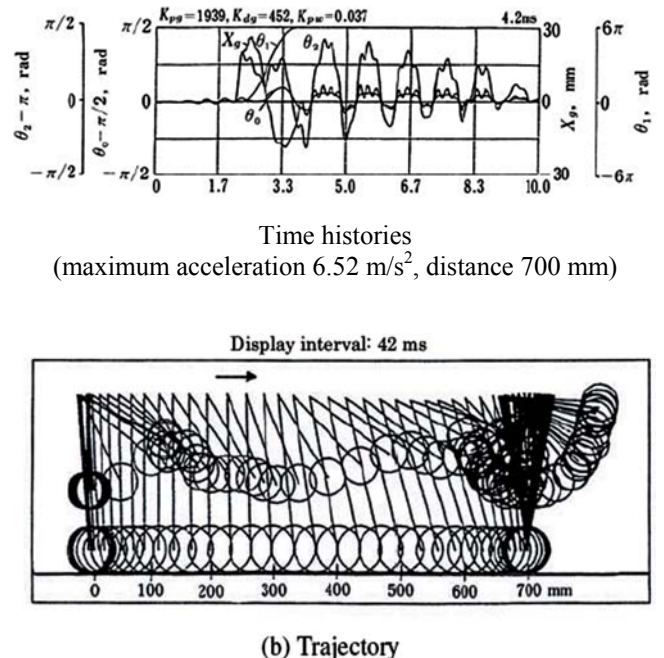


Figure 11 P-3 Experimental results of CGFC control with dynamic compensation.

The CGFC rule developed in this study for controlling the PB robots is based on the principle of tumbler's posture restoration and can be applied to other robots or objects having an unstable posture. When the arms are used to stabilize the posture, the wheels can be driven to a destination independently from the robot's posture [14, 18].

4 TRANSFORMATION OF PB ROBOTS: PROTOTYPES P-4 THROUGH P-6

The authors also proposed several patented transformations of the basic PB robot P-3 [19, 20]. Some of them were developed into prototypes P-4 through P-6 for performing different tasks.

4.1 PROTOTYPE P-4

In addition to the body, arms and wheels in a basic PB robot (such as P-3), legs and arms can be added as new modules. Using these modules, two types of PB robots, the arm-leg model and the leg-leg model, can be constituted as illustrated in Figure 12.

The arm-leg model shown in Figure 12(b) can emulate human postures of standing and sitting. This model was developed into prototype P-4. Figure 13 shows the change from a standing to a sitting posture of P-4 from experiments [20]. P-4 can also bounce and sift as well as a rabbit. It is experimentally found that P-4 can jump 4 mm high and 13 mm long [20].

4.2 PROTOTYPES P-5 AND P-6

The authors further explored the possibility of using one arm to stabilize the PB robot body and the other arm to perform specific tasks, such as manufacturing, rescue, and entertainment [21, 22]. The compact size of a PB robot, in comparison with a four-wheeled vehicle or a human being, gives the PB robot more advantages to move and work in a narrow and limited space [21].

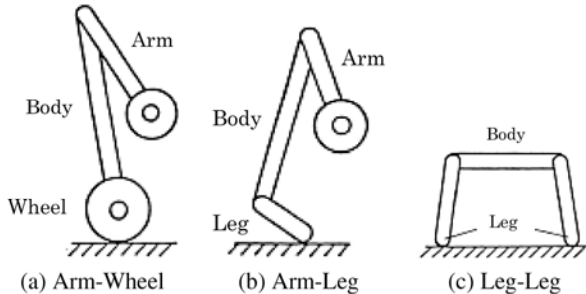


Figure 12 Transformations of PB robots.

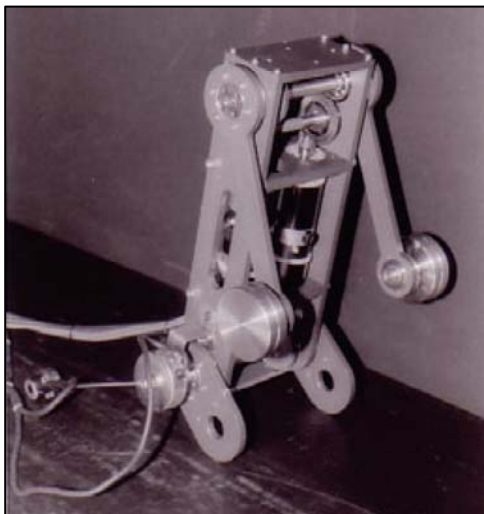


Figure 13 P-4 changing posture from standing to sitting.

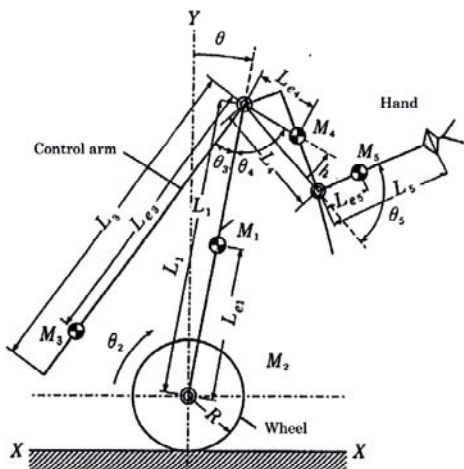


Figure 14 P-5 with a working hand and a control arm.

Figure 14 shows a model of the prototype P-5 robot with a working hand developed by Yamafuji et al. [23, 24]. The hand has four degrees of freedom of motion, two of which are actuated by shape memory alloys (SMA). In addition, a control arm with a counter weight is equipped to control the stability of the pendulum body. Furthermore, a wheel can be added to the lower end of the control arm to transform into a three-wheeled vehicle for increased stability [23, 24]. In case the robot loses its stability and falls down, it can stand up from the fallen posture by moving the control arm, as demonstrated in the experimental results in Figure 15 [23].

In the prototype P-6 robot [25, 26], a back joint is added in addition to the wheeled arms, and the arms can support the whole body as shown in Figure 16. P-6 can ascend and descend stairs by coordinating the control of the back joint and the arms. Figure 17 shows experimental trajectories of P-6 ascending a step of 25 cm height. P-6 can further transform itself into a four-wheeled vehicle by touching down both of the wheeled arms on the floor [26].

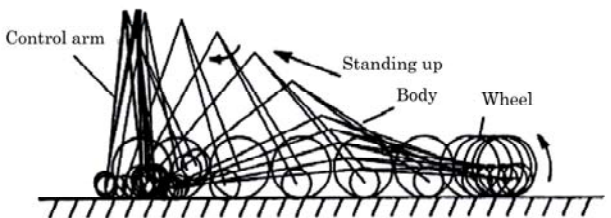


Figure 15 Experimental trajectory of P-5 standing up from a fallen posture (Display interval: 0.8 seconds).

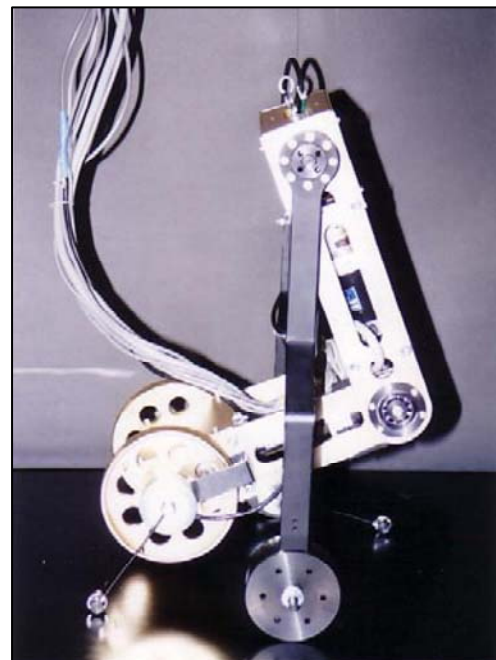


Figure 16 P-6 holding up the body using arms.

5 OTHER R&D ACTIVITIES ON PB ROBOTS

Since PB robots have simple structures and a high degree of instability, they are often used as a test bed for evaluating various kinds of control methods. Yamafuji and Feng [27] conducted experiments on P-1 and P-2 by applying nonlinear control rules [9]. Matsumoto et al. [28] installed an angular velocity detector on a PB robot and estimated the posture angle by use of a state observer. They succeeded in keeping the robot in the upright posture while driving it on an inclined plane. Lee et al. [29] succeeded in standing upright control of a PB robot using a linear self-organizing fuzzy controller. Hiraoka and Noritsugu [30, 31] investigated, by experiments and simulation, the response of an upright PB robot against initial disturbances and applied a sliding mode control to maintain the postural stability.

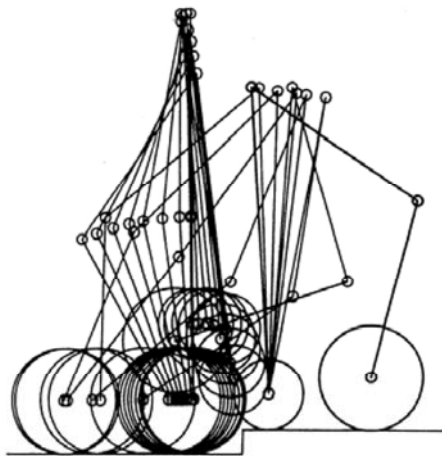


Figure 17 Experimental trajectory of P-6 ascending a step (Display interval: 0.8 seconds).

As a PB robot transformation, Matsumoto et al. [32] developed a four-wheeled vehicle by combining two PB robots (as patented by the authors [22] in 1990). Using flexible joints, their vehicle could ascend and descend stairs. Shiroma et al. [?] reported a unique system in which a PB robot carried an object in collaboration with a human worker. Hiraoka and Noritsugu [34] proposed a method to transfer an object with cooperation of multiple PB robots by controlling forces. They experimentally demonstrated a ball being carried by cooperation of two PB robots.

In December 2004, TOYOTA Motor Ltd., announced that they had developed two types of humanoid and would be demonstrated at the 2005 Nagoya International Exhibition. One is a biped robot and the other a PB based humanoid as shown in Figure 18. This PB humanoid has working hands without control arms. If the working hands handled more heavy objects, control arms would become necessary for stabilizing the body. Since PB robots have simple and inexpensive locomotion mechanisms and are easy to control in comparison with a biped robot, more PB humanoids are expected to emerge.



Figure 18 TOYOTA's two types of humanoid.



Figure 19 Sweeper.

6 COMMERCIAL APPLICATIONS OF PB ROBOTS

Industrial or commercial applications of PB robots are limited so far. In 1993, Sakurai Precision Ltd. (Japan), commercialized a P-1 type PB robot named "STANDUCK" [35] for entertainment use or as a test bed for evaluating control methods. It has a pole with an overhead weight standing upright between the wheels. In December 2001, Dean Kamen, an American inventor received publicity for commercializing Segway as a personal transporter. Segway shares the same technologies as the prototype PB robots developed by the authors (as presented earlier in this paper and its references).

In 2002, the authors developed another personal transporter named "Sweeper", which resembles a witch's broom. The first Sweeper was composed of a PB and a long pole between the wheels. A rider wearing roller skates sits on the pole and is transported by the motordriven PB. After extensive experimental study, the parallel double wheels were replaced by a single wheel as a unicycle, as shown in Figure 19. Young people can easily master the ride with 10-minute practicing, because of an advanced human interface equipped in Sweeper for intuitive control Kawaguchi et al. [36, 37] received publicity for their success in Sweeper.

7 CONCLUSIONS

A basic PB robot consists of a pair of parallel wheels and an inverted pendulum body pivoted by the wheel axis. The upright and unstable posture of the pendulum body can be controlled either by moving the wheels or rotating additional arms. This paper presented six prototype PB robots developed by the authors since 1986, including the basic PB robot, a PB robot with double control arms, a PB robot with one control arm and one working hand, and other transformations. Two simple but effective posture control algorithms were presented: one is for controlling the wheels based on the inclination angle of the body and the other is for controlling the arms to move the centre of gravity of the robot for posture restoration as a tumbler. Extensive experimental study demonstrated the effectively of these control algorithms. In addition, this paper also reviewed research and development activities on PB robots by other researchers and inventors [8, 38]. Due to their simple structures and posture instability, PB robots often serve as a test bed for evaluating control methods.

Finally, this paper reviewed applications of PB robots in personal transporters including the Segway and the Sweeper. Considering their compact size, simple and inexpensive locomotion structure, and the easy control, in comparison with four-wheeled vehicles or biped humanoids, more industrial and commercial applications of the PB robots are expected.

REFERENCES

- [1] S. Mori, N. Nishihara and K. Furuta, "Control of an Unstable Mechanical System," Int. Journal of Control, 23-5, pp. 673-692, 1976.
- [2] Q. Feng and K. Yamafuji, "Design and Simulation of a Control System of an Inverted Pendulum," Robotica, Cambridge University Press, 6-2, pp. 235-241, 1988.
- [3] K. Yamafuji and K. Inoue, "Study on the Postural Stability of a Unicycle (in Japanese)," Preprint of Annual Yamanashi Meeting of Japan Society of Mechanical Engineering (JSME), 4-6, 1986.
- [4] Z. Q. Sheng and K. Yamafuji, "Study on the Stability and Motion Control of a Unicycle (Part 1: Dynamics of a human riding unicycle and its modeling by link mechanisms)," JSME Int. Journal, Series 3, 38-2, pp. 249-259, 1995.
- [5] Z. Q. Sheng and K. Yamafuji, "Study on the Stability and Motion Control of a Unicycle (Part 2: Design and experimental results of a unicycle robot) (in Japanese)," Trans. JSME, 61-583C, pp. 1042- 1049, 1995.
- [6] Z. Q. Sheng and K. Yamafuji, "Study on the Stability and Motion Control of a Unicycle (Part 3: Characteristics of a unicycle robot)," JSME Int. Journal, Series 3, 39-3, pp. 560-568, 1996.
- [7] Z. Q. Sheng and K. Yamafuji, "Postural Stability of a Human Riding a Unicycle and Its Emulation," IEEE Trans. on Robotics and Automation, 13-5, pp. 709-720, 1997.
- [8] K. Yamafuji and T. Tanaka, R&D of Innovative Robots (in Japanese), Yokendo Publ., Tokyo, 2002.
- [9] K. Yamafuji and Q. Feng, "Study on the Postural Control of a Twin Cycle (Part 1, Design and simulation of a nonlinear control system of an inverted pendulum model) (in Japanese)," Journal of Japan Society for Precision Engineering (JSPE), 53-10, pp. 1622-1625, 1987.
- [10] K. Yamafuji and T. Kawamura, "Stability and Driving Control of a Coaxial Bicycle (in Japanese)," Trans. of JSME, 54-501C, pp. 1114-1121, 1988.
- [11] K. Yamafuji and T. Kawamura, "Stability Control of a Coaxial Bicycle (in Japanese)," Journal of Robotic Society of Japan (RSJ), 7-4, pp. 338-343, 1989.
- [12] K. Yamafuji and K. Yoshida, Japanese Patent, No.2530652, 1987.
- [13] K. Yamafuji and Y. Miyagawa, T. Kawamura, "Design and Steering Control of the Parallel Bicycle (in Japanese)," Trans. of JSME, 55- 513C, pp. 1229-1233, 1989.
- [14] T. Hirabayashi and K. Yamafuji, "Posture and Driving Control of a Variable Structure Type Parallel Bicycle (1st Report, Upright posture and driving control of an arm-wheel model) (in Japanese)," ibid., 56-523C, pp. 721-730, 1990.
- [15] T. Hirabayashi and K. Yamafuji, "Posture and Driving Control of a Variable Structure Type Parallel Bicycle (4th Report, Motion control of the control arm-wheel model) (in Japanese)," ibid., 58-545C, pp. 193-199, 1992.
- [16] T. Hirabayashi and K. Yamafuji, "Posture and Driving Control of a Variable-Structure Type Parallel Bicycle (6th Report, Driving control of the control arm-wheel model on a slope whose shape is not known) (in Japanese)," ibid., 59-563C, pp. 2185-2190, 1993.
- [17] T. Hirabayashi and K. Yamafuji, "Posture and Driving Control of a Variable-Structure Type Parallel Bicycle (3rd Report, Dynamic analysis of a control arm-wheel model) (in Japanese)," ibid., 57-539C, pp. 2328-22335, 1991.
- [18] T. Hirabayashi and K. Yamafuji, "Posture and Driving Control of a Variable Structure Type Parallel Bicycle (5th Report, High speed drive of the arm-wheel model) (in Japanese)," ibid., 58-552C, pp. 2501-2506, 1992.

- [19] H. Kanai and K. Yamafuji, "Posture Change and Locomotion by Jump of the Control Arm-Leg Model of the Variable-Structure Robot (in Japanese)," Trans. of JSME, 57-39C, pp. 2336-2341, 1991.
- [20] T. Hirabayashi and K. Yamafuji, "Control of the Variable-Structure Type Locomotive Robot (Walking forms and controlling methods of the leg-leg type)," JSME Int. Journal, Series 3, 35-4, pp. 598, 1992.
- [21] K. Yamafuji, "The Robots for Service Use Based on the Parallel Bicycles (in Japanese)," Mechanical Automation, 20-11, pp. 113- 118, 1989.
- [22] K. Yamafuji and T. Naruse, Japanese Patent, No.2772972, 1998.
- [23] K. Yamafuji and A. Koshiyama, "Posture and Motion Control of the Variable Structure Type Parallel Bicycle (2nd Report, Standing up and fall down by using torque changing method) (in Japanese)" Trans. of JSME, 57-539C, pp. 2285-2290, 1991.
- [24] K. Yamafuji, A. Koshiyama, T. Misawa and S. Okuda, "Posture and Motion Control of the Variable Structure Type Parallel Bicycle (3rd Report, Development of a working arm, control methods and experimental results) (in Japanese)," ibid., 59-564C, pp. 2368-2375, 1993.
- [25] T. Yasui and K. Yamafuji, "Motion Control of a Parallel Bicycle Type Mobile Robot with a Control Arm and Body Composed of Three Links (in Japanese)," ibid., 57-538C, pp. 1904-1909, 1991.
- [26] Y. Momoi and K. Yamafuji, "Motion Control of a Parallel Bicycle Type Mobile Robot with a Control Arm and Body Composed of Three Links (2nd Report, Driving control) (in Japanese)," ibid., 57-541C, pp. 2938-2943, 1991.
- [27] K. Yamafuji and Q. Feng, "Study on the Postural Control of a Twin-Cycle(Part 2, Experimental results) (in Japanese)," Journal of JSPE, 54-9, pp. 1759-1764, 1988.
- [28] O. Matsumoto, S. Kajita and K. Tani, "Estimation and Control of the Attitude of a Dynamic Mobile Robot Using Internal Sensors (in Japanese)," Journal of RSJ, 8-5, pp. 541-550, 1990.
- [29] Y. N. Lee, T. W. Kim and I. H. Suh, "A look-up Table-based Selforganizing Fuzzy Plus Linear Controller," Mechatronics Journal, 4-1, pp. 71-90, 1994.
- [30] N. Hiraoka and T. Noritsugu, "Posture Control of a Parallel Biwheel Vehicle Driven with a Stepping Motor," Proc. of 2nd Japan-France Congress on Mechatronics, 2, pp. 7-10, 1994.
- [31] N. Hiraoka and T. Noritsugu, "Closed-Loop Posture Control of Parallel Biwheel Vehicle Driven with a Stepping Motor (in Japanese)," Trans. of JSME, 61-592C, pp. 4638-4645, 1991.
- [32] O. Matsumoto, S. Kajita, K. Tani et al., "A Four-Wheeled Robot to Pass over Steps by Changing Running Control Modes (in Japanese)," Journal of RSJ, 13-6, pp. 822-829, 1995.
- [33] N. Shiroma, O. Matsumoto and K. Tani, "Cooperative behaviour of a mechanically unstable mobile robot for object transportation," JSME Int. Journal, Series 3, 42-4, pp. 965-973, 1999.
- [34] N. Hiraoka and T. Noritsugu, "Reaction Force Control of a Parallel Biwheel Vehicle Driven with a Stepping Motor," Proc. of 3rd Int. Conf. on Advanced Mechatronics, Okayama, 2, pp. 698-703, 1998.
- [35] K. Yamafuji, R&D in Universities and the Rights of Intellectual Property, University of Electro-Communications News (in Japanese), October/November, 23, 2000.
- [36] K. Kawaguchi, T. Tanaka, K. Yamafuji and T. Uehara, "Sweeper: New Vehicle Modeled on a Magic Broom (1st Report, Concept and development of a prototype) (in Japanese)," Proc. of 10th Annual Conf. of Kanto Branch of JSME, pp. 411-412, 2003.
- [37] K. Kawaguchi, T. Tanaka, K. Yamafuji and T. Uehara, "Sweeper: New Vehicle Modeled on a Magic Broom (2nd Report, Human interface for intuitive control) (in Japanese)," Proc. of 2004 JSME Conf. on Robotics and Mechatronics, 2P2-H-13, 1-2, 2004.
- [38] K. Yamafuji, Robots A to Z (in Japanese), Ohmsha Publ., Tokyo, 1995.

LOCOMOTION PERFORMANCE EVALUATION OF AN ALL-TERRAIN ROVER

Mario M. Foglia*

Giulio Reina**

*Dipartimento di Ingegneria Gestionale e Meccanica, Politecnico di Bari, Bari, Italy

**Dipartimento di Ingegneria dell'Innovazione, Università del Salento, Lecce, Italy

ABSTRACT

In the last few years, mobile robots are increasingly being used in natural outdoor terrain for applications such as forestry, mining, rescuing, precision farming, and planetary exploration. Future tasks will require robotic vehicles to travel over longer distances through challenging terrain, with limited human supervision. To accomplish this objective, a higher degree of mobility will be primarily required, ensuring, at the same time, the safety of the vehicle. In this paper, a robot with advanced mobility features is presented and its locomotion performance is evaluated, following an analytical approach. The proposed vehicle features an independently controlled 4-wheel-drive/4-wheel-steer architecture that allows the robot to perform maneuvers such as turn-on-the-spot and crab motion. It also employs a passive rocker-type suspension system, improving the ability to traverse uneven terrain, while ensuring good traction performance. An overview of modeling techniques for rover-like vehicles is introduced. First, a method for formulating a classical kinematic model of an articulated vehicle is presented. Next, a method for expressing a quasi-static model of forces acting on the robot is described. Note that quasi-static models are appropriate due to the relative low speed and acceleration of those vehicles. Two optimization methods are also proposed to control the rover's motion, minimizing slip and power consumption, respectively. These models are used to reproduce the behavior of the robot in typical obstacle-climbing scenarios, pointing to the advantages compared with conventional architectures.

Keywords: rough-terrain robotics, articulated suspension system, rover modeling, locomotion performance

1 INTRODUCTION

For mobile robots driving across natural outdoor terrain, it is critical to employ an efficient and reliable locomotion system. The success of rough-terrain missions greatly depends on the ability of this system to effectively traverse whatever terrain is encountered by the robot. Different locomotion solutions have been proposed, including wheel with suspension, leg mechanisms, tracks, hopping, and snake-like systems. All the major types of mobility systems can be broadly classified under the following three categories [1]:

Contact author: G. Reina

Dipartimento di Ingegneria dell'Innovazione,
Università del Salento, via Arnesano, 73100 Lecce, Italy
E-mail: giulio.reina@unisalento.it

- Wheeled systems:
 - Rocker-bogie suspension and its derivates, e.g., NASA's twin Mars rovers Spirit and Opportunity [2], and the Shrimp [3]
 - Wheeled structures, e.g., Nomad [4], Lunakhod, and Marsokhod [5]
- Tracked systems:
 - Linked tracks, e.g., Tanks and Urban II [6]
 - Rigid tracks, e.g., Nanokhod [7]
 - Suspended tracks, e.g., Elastic Loop Mobility System [8]
- Legged systems: e.g., Dante II [9]

Walking robots potentially represent the best locomotion system on rugged terrain, overcoming most of the problems affecting either wheeled or tracked robots. However, legged robots face a number of challenges. Many of these

challenges stem from the large number of degrees of freedom required by legged systems that make their cost of building higher relative to those with wheels or tracks; walking mechanisms are also more complex and thus more prone to failure. Furthermore, control algorithms became more involved and optimal control of walking machines is still an active area of research.

There has long been a belief that tracks have better mobility than wheels. Tracked vehicles have demonstrated their better performance especially for very soft terrain as deep mud and loose sand, obstacles of a size that can get jammed between wheels, and for crevasses. However, they get the higher mobility at a cost of greater complexity, lower drive efficiency and higher power-to-weight ratio. The steering is obtained by “skid” steering, i.e. by differential driving of the two tracks. The lateral forces generated during skid steering are considerable, requiring stronger structural support than traditional steering. Friction within the tracks themselves dissipates energy whenever the vehicle turns because the treads must slip against the ground. Because of the large amount of skidding during a turn, the exact center of rotation of the robot is hard to predict and the exact change in position and orientation is also subject to variations, depending on the ground friction. Therefore, the dead-reckoning ability of tracked vehicle is poor. In terms of power efficiency, this approach is reasonable efficient on low friction surface but extremely inefficient otherwise. Finally, tracks are also vulnerable to dust and debris between the wheels and the track.

The wheel has been by far the most popular locomotion mechanism in mobile robotics for several practical reasons. Wheeled robots are mechanically simple and easy to construct. The payload weight-to-mechanism ratio is also favorable. Both legged and tracked systems generally require more complex and heavier hardware than wheeled systems designed to carry the same payload. The principal disadvantage of wheels is that, on uneven terrain, they may perform poorly. As a rule, a wheeled vehicle has trouble if the height of the object it must surmount approaches the radius of the wheels. In order to overcome this issue, a suspension system may be used to allow all wheels to maintain ground contact. Although the details of automotive suspensions used today are widely varied, they all use some form of spring and shock combination to provide good control and a relatively comfortable ride to the driver. Most suspensions are designed for high-speed control over mostly smooth surfaces, but more importantly, they are designed for human driven vehicles. In spite of their popularity and notable performance in race cars and off-road vehicles, there are very few sprung suspension systems adopted in mobile robotics. Springs mainly address rider comfort and control issues in vehicles that travel more than about 8 m/s. Below that speed, they are actually an impediment to mobility since they change the force each wheel exerts on the ground, as obstacles are negotiated. A four-wheeled conventional independent suspension vehicle appears to keep all wheels equally on the ground, but the

wheels that are on the bumps, being lifted, are carrying more weight than the other wheels. This reduces the traction of the lightly loaded wheels. The better solution, at low speeds, is to allow some of the wheels to rise, relative to the chassis, over bumps without changing the weight distribution or changing it as little as possible. This objective can be achieved using an articulated, passive suspension system [10], usually referred to as rocker-bogie suspension system.

In this paper, a mobile robot is presented for applications on rough terrain, built in collaboration between the Università del Salento and the Politecnico di Bari, and named Dune. Dune, shown in Figure 1, is an all-wheel-drive independent steering robot, employing a rocker suspension system to enhance its mobility and traction performance on uneven terrain. According to this suspension design, the drive wheels of either side of the vehicle are connected longitudinally by a rigid link, called rocker arm. Each one of the two rockers is pivoted to the main frame of the vehicle through the axis of a differential gearbox, whose input gear is attached to the chassis (see Figure 2). This configuration allows the rocker arms to pivot when any wheel tries to go higher or lower than the rest. This passive pivoting action keeps the load on all four wheels almost equal, increasing mobility simply by maintaining driving and braking action on all wheels at all times. Moreover, the mechanical differential constraints the pitch angle of the chassis to be half of the pitch angle of either side rocker. This pitch averaging effectively reduces the pitching motion of the chassis, maintaining it at a more level pose, as either side of the suspension system travels over obstacles. This is beneficial in vehicles under camera control, and, in general, a fully autonomous sensor driven robot can benefit from less rocking motion of the main chassis.

The paper also presents an overview of modeling techniques for rover-like robot operating on rough terrain. These models can be used as a basis for advanced control and motion planning methods to improve a vehicle's mobility. Firstly, a method for formulating a classical kinematic model of a rover is presented. Secondly, a method for expressing a quasi-static model of forces acting on the vehicle is described. Note that quasi-static models



Figure 1 The rover Dune.

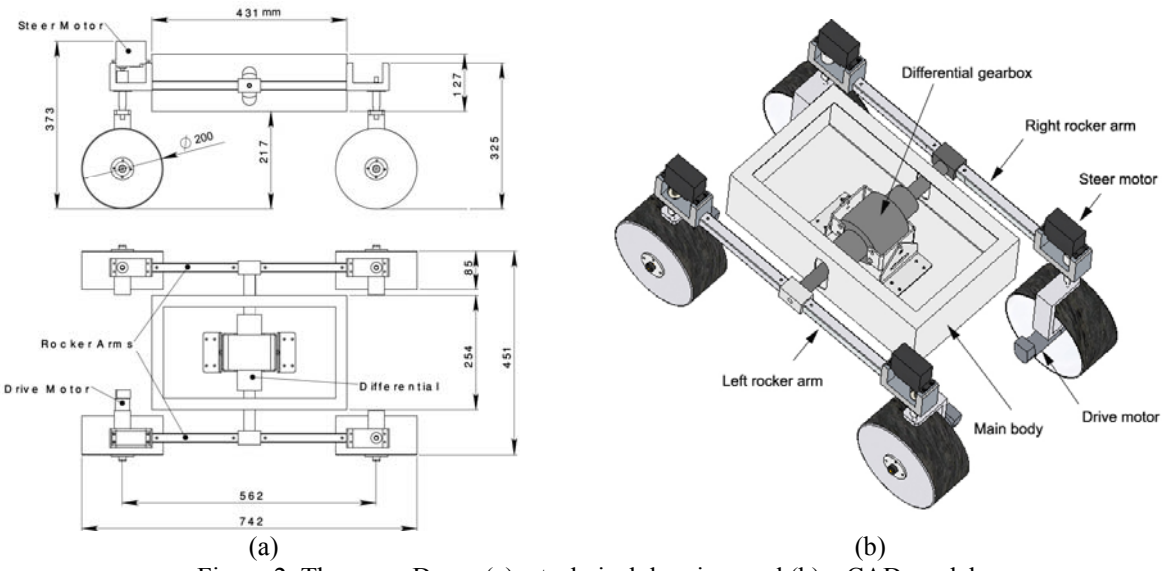


Figure 2 The rover Dune: (a) a technical drawing, and (b) a CAD model.

are appropriate due to the relative low speed of those vehicles. These models are computationally simple, and thus practical for on-board implementation. Based on these models, the motion performance of the rover can be analyzed, demonstrating its advantages over conventional vehicles in various challenging situations. Specifically, two typical scenarios are considered. In the first scenario, the rover traverses over an obstacle of increasing height up to one and half the wheel diameter. The second scenario deals with the negotiation of a slope in presence of obstacles. One fundamental issue connected with the control of over-constrained rovers, i.e. having more independent motors than degrees of freedom, is that the actual speeds and steering angles of the wheels have to match perfectly. Even small discrepancies will result in the wheels “fighting” each other. This phenomenon can be observed in many early Sports Utility Vehicles (SUVs) in four-wheel drive mode on high-traction ground. However, when the SUV drives on slippery ground, such as sand, then this effect is less noticeable. One method for reducing this effect and the associated wheel slippage in over-constrained mobile robots is to adopt an appropriate control algorithm. Here, two optimization methods are described and evaluated, which aims to minimize wheel slip and power consumption, respectively.

In the reminder of this paper, the rover Dune is described in more detail in Section 2. Description of rover modeling techniques is provided in Section 3. Next, a mobility analysis and comparison with a vehicle, equipped with a conventional spring suspension system, is discussed in Section 4. Finally, conclusions are drawn in Section 5.

2 THE ROVER DUNE

Dune is an independently controlled 4-wheel-drive/4-wheel-steer vehicle. This configuration provides a high degree of maneuvering, allowing the robot to perform

special maneuvers such as crab and turn-on the spot motion, as shown in Figure 3. The rover also employs a four-wheel passive suspension system, called rocker suspension that connects the four wheels to the body of the rover. An internal differential gearbox provides connection with the left and the right side rockers to the rest of the vehicle. Figure 2 shows the mechanical details of this design. The primary role of the suspension system is to ensure that all four wheels remain in contact with the ground all the times, despite one wheel moving higher or lower than the others, avoiding a very soft spring suspension. Ground pressure is uniformed between all wheels, maximizing traction and the rover's ability to climb obstacles. This is extremely important in soft terrain where excessive ground pressure can result in the vehicle sinking into the driving surface. The mechanical differential also serves to mediate the difference in ground terrain between both sides of the rover, allowing the main body to see only half of the disturbance. Overall, the rocker suspension system provides remarkable mobility over obstacles, allowing the rover to safely traverse rocks over one and half its wheel diameter [10], whereas a 4-wheeled vehicle with conventional suspension may only be able to climb one half its wheel diameter, as demonstrated later in Section 4.

The rover's size and mass properties are collected in Table I. A 2 kg NiCad battery pack provides about 100 Wh of energy; peak driving speed is 150 cm/s on flat ground. Dune's control and acquisition architecture is based on a NI CompactRIO embedded system, which incorporates a real-time processor with reconfigurable FPGA, and hot-swappable I/O modules for direct connection to sensors and actuators, according to the general scheme shown in Figure 4. The controller features a 10/100 Mb/s Ethernet port, which allows wireless communication over the network using an onboard router, for mult-client remote control or monitoring. The sensor suite is composed of optical

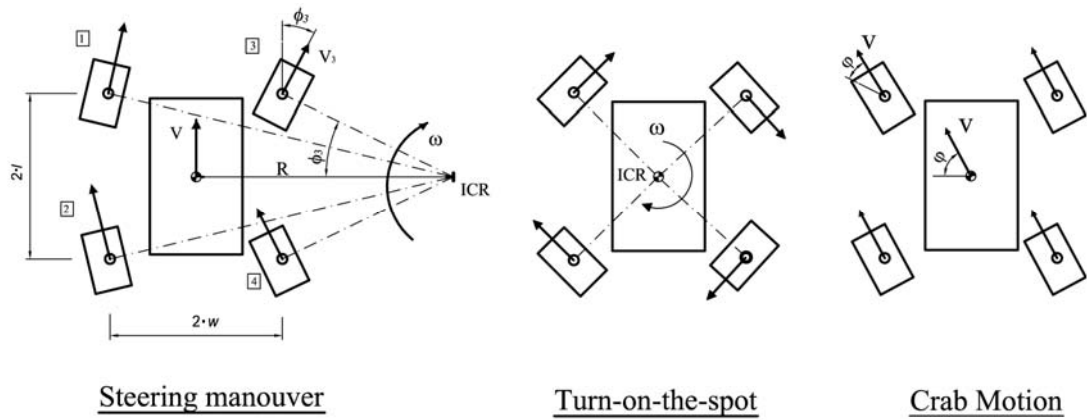


Figure 3 Feasible maneuvers for the rover Dune.

encoders and potentiometers, to measure, respectively, the wheel angular velocities and the wheel steering angles, of potentiometers to estimate the rocker suspension angles, and of an inertial unit, composed of a three-axis gyroscope and of a three-axis accelerometer, to estimate vehicle tilt and attitude.

Those sensors are essential for position estimation and accurate control during operation. The vehicle is also equipped with ammeters to monitor the electrical current absorbed by each motor. Since electrical current is known to be roughly proportional to torque, the latter sensors can be used to gather information about wheel-terrain interaction and give an estimate of wheel tangential forces.

3 ROVER MODELING

In this section, two rover modeling techniques are presented and briefly described. The first is a classical kinematic model for articulated mobile robots. The second is a quasi-static model of forces acting on the rover.

3.1 ROVER KINEMATIC MODEL

Kinematic analysis is an important aspect of rover mobility prediction. Here, a forward kinematics model is presented that extends the classical approach, proposed by Denavit and Hartenberg in [11] for industrial robots, to the case of mobile robots featuring an articulated suspension system.

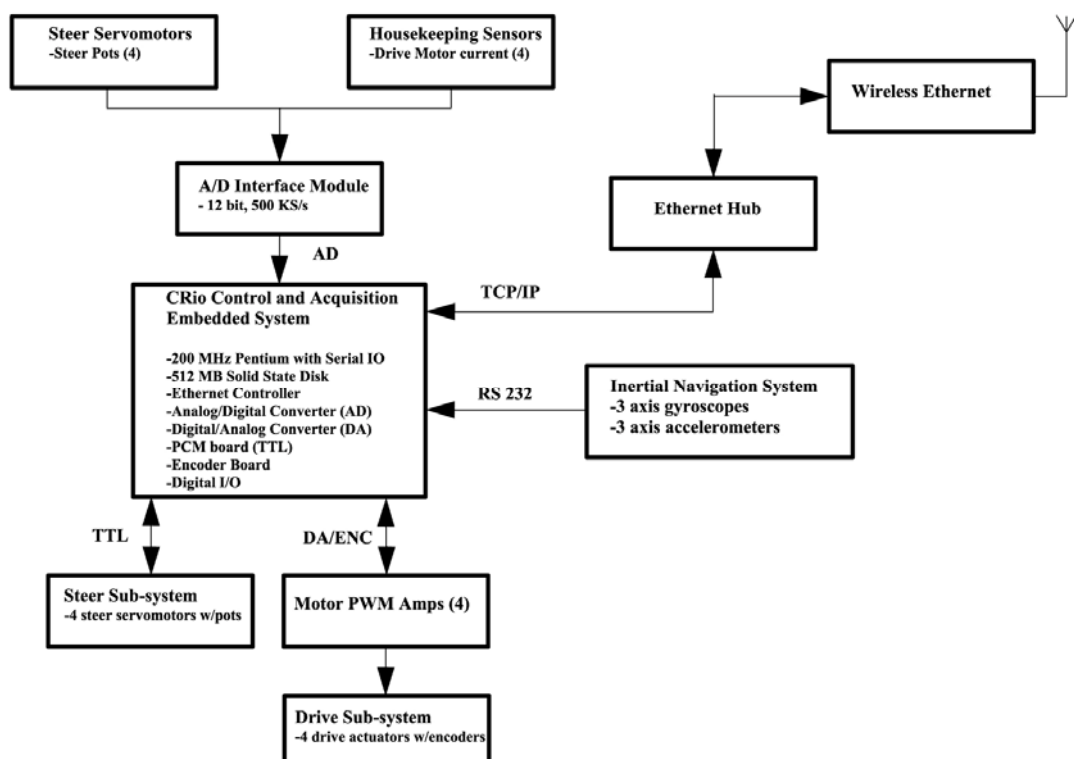


Figure 4 Control and acquisition architecture.

Table I - Dune's properties

| | |
|------------------|----------------------------------|
| Dimensions | $0.74 \times 0.45 \times 0.32$ m |
| Wheel Diameter | 0.20 m |
| Ground clearance | 0.21 m |
| Total mass | 16 kg |
| Structure | 10 kg |
| Batteries | 2 kg |
| Motors | 2 kg |
| Computer System | 2 kg |
| Max speed | 150 cm/s |

We start by defining a set of coordinate frames for our vehicle Dune. These frames are illustrated in Figure 5(a) for the left side of the rover that consists of Wheel 1, Wheel 2, and left arm rocker. The right side is not shown but it is assigned similar frames. The subscripts for the coordinates frames are as follows: V refers to the rover frame passing through its center of mass, D refers to the differential, S_i refers to the steering wheels with $i=1, \dots, 4$, A_i denotes the wheel i with $i=1, \dots, 4$. The frames were chosen for consistency with Denavit-Hartenberg notation [12]. Each coordinate frame represents one step in the kinematic chain from the rover's reference frame to one wheel. For example, the kinematic chain to Wheel 1 is: V→D→S₁→A₁ or the path to Wheel 4 is V→D→S₄→A₄. Other quantities shown in Figure 5(a) are steering angles ϕ_i and rocker angles β_i . Note that in the vehicle's reference frame the following kinematic constraint holds due to the presence of the mechanical differential, $\beta'_L = -\beta'_R = \beta$. In Table II, the D-H parameters corresponding to various coordinate frames are collected. The four D-H parameters associated with each frame characterize the transformation from a previous frame following the kinematics chain of coordinate frames. This transformation consists of a sequence of steps composed of a rotation λ about the z-axis, a translation d along the z-axis, a translation a along the x-axis, and finally a rotation α about the x-axis. The transformation from a coordinate frame i to a previous frame $i-1$ is expressed by the homogeneous matrix

$$T_i^{i-1} = \begin{pmatrix} \cos \lambda_i & -\sin \lambda_i \cdot \cos \alpha_i & \sin \lambda_i \cdot \sin \alpha_i & a_i \cdot \cos \lambda_i \\ \sin \lambda_i & \cos \lambda_i \cdot \cos \alpha_i & -\cos \lambda_i \cdot \sin \alpha_i & a_i \cdot \sin \lambda_i \\ 0 & \sin \alpha_i & \cos \alpha_i & d_i \\ 0 & 0 & 0 & 1 \end{pmatrix} \quad (1)$$

Where λ_i , d_i , a_i and α_i are the D-H parameters given for coordinate frame i . All the parameters are collected in Table II. For instance, the parameters λ_D , d_D , a_D and α_D characterize the transformation from rover's reference frame to differential reference frame. Thus, the motion of each wheel relative to its coordinate frame can now be referred to the rover's reference frame V by a sequence of transformation matrices based on D-H parameters. For example, the transformation from Wheel 1 axle to frame V

is obtained by cascading the transformations along the kinematics chain of coordinate frames

$$T_{A_1}^V = T_D^V \cdot T_{S_1}^D \cdot T_{A_1}^{S_1} \quad (2)$$

The vehicle attitude with respect to the ground reference system can be expressed in terms of Euler angles. In our system the RPY or ZYX convention is chosen. Figure 5(b) shows the three Euler angles ϕ , θ , ψ , which are usually referred to as *roll*, *pitch* and *yaw*, respectively [13]. A final transformation is needed from the vehicle coordinate frame to the ground coordinate frame, defined as

$$T_V^G = \begin{pmatrix} c\psi \cdot c\theta & c\psi \cdot s\theta \cdot s\phi - s\psi \cdot c\phi & c\psi \cdot s\theta \cdot c\phi + s\psi \cdot s\phi & p_x \\ s\psi \cdot c\theta & s\psi \cdot s\theta \cdot s\phi + c\psi \cdot c\phi & s\psi \cdot s\theta \cdot c\phi - c\psi \cdot s\phi & p_y \\ -s\theta & c\theta \cdot c\phi & c\theta \cdot s\phi & p_z \\ 0 & 0 & 0 & 1 \end{pmatrix} \quad (3)$$

here c and s , refer to \cos and \sin , respectively. To fully define the rover configuration in the ground coordinate frame, eight parameters are required: the position of the center of mass of the body $p_c = (p_x, p_y, p_z)$, the orientation of the rover body (ϕ, θ, ψ), and the configuration parameters of the rocker mechanism in the ground reference frame (β_R, β_L).

The inverse kinematics problem involves computing the orientation of the rover body and the configuration of the rover suspension, given the shape of the terrain and the position of the center of the body p_c . To this aim, a wheel-

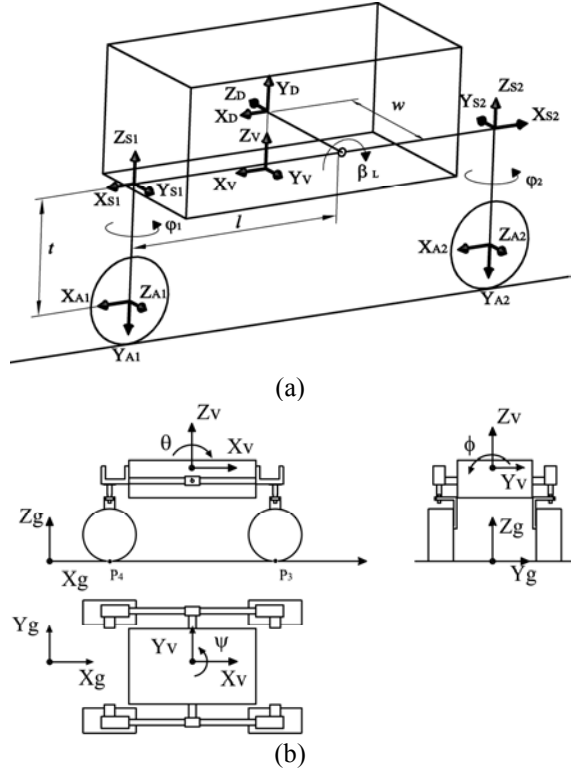


Figure 5 Coordinate frames (a), and the RPY Euler angles for the rover Dune (b).

Table II - D-H parameters for primary coordinate frames

| Frame | λ_i (deg) | d_i (mm) | a_i (mm) | α_i (deg) |
|----------------|----------------------|------------|------------|------------------|
| D | 0 | 0 | 0 | 90 |
| S ₁ | β | - w | l | -90 |
| A ₁ | φ_1 | - t | 0 | -90 |
| S ₂ | $180+\beta$ | - w | l | 90 |
| A ₂ | $180+\varphi_2$ | - t | 0 | -90 |
| S ₃ | - β | w | l | -90 |
| A ₃ | φ_3 | - t | 0 | -90 |
| S ₄ | $180-\beta$ | w | l | 90 |
| A ₄ | $180+\varphi_4$ | - t | 0 | -90 |

terrain contact model is required. It is assumed that each wheel makes contact with the terrain at a single point, denoted with P_i , $i = 1, \dots, 4$. This is a reasonable assumption for vehicles with rigid wheels (such as currently planned Mars rovers) moving on firm terrain. Note that a toroidal wheel model is assumed, which allows one to simulate a single contact point with terrain even in presence of lateral inclination of the robot. For vehicles moving on deformable terrain, distributed wheel-terrain contact stresses can be resolved to resultant forces at a single point.

In general, a wheel-terrain contact force exists at each point P_i and is denoted with $f_i = [f_{t,i}, f_{l,i}, f_{n,i}]^T$ (see Figure 6, for a planar schematization). The vector is expressed in the wheel-soil contact frame, and can be decomposed into a tractive and lateral force $f_{t,i}$ and $f_{l,i}$, respectively, tangent to the wheel-terrain contact plane, and a normal force $f_{n,i}$ normal to the wheel-terrain contact plane. It is assumed that there are no moments acting at the wheel-terrain interface. The angle γ_i measures the inclination between the horizontal and the wheel-terrain contact plane i .

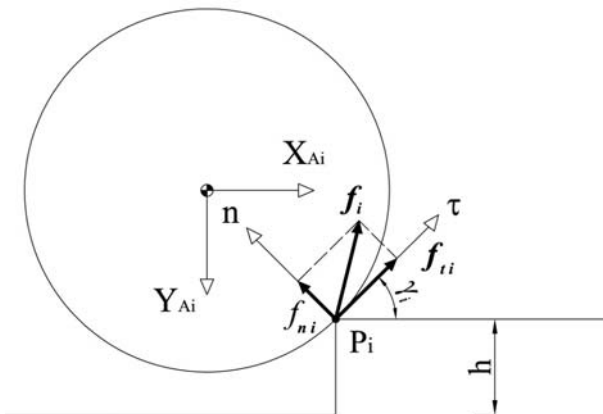


Figure 6 Wheel-terrain contact model (plane schematization).

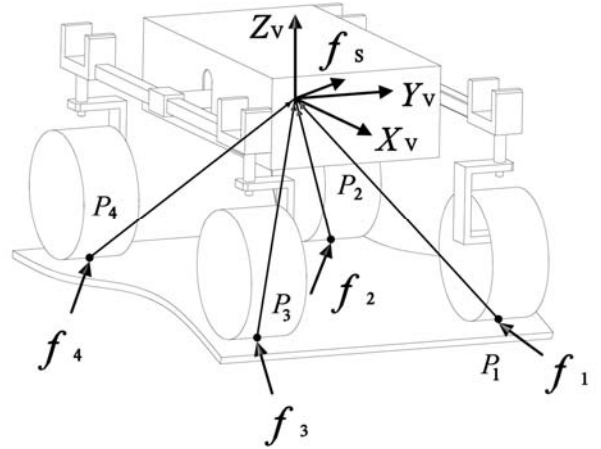


Figure 7 Force analysis for a four-wheeled rover.

For a vehicle with m unique wheel-terrain contact points, at least $m-1$ kinematic loop closure equations can be written [14]. If we consider the i -th wheel contact points P_i , expressed in the ground reference system,

$$P_i = \begin{bmatrix} P_i^x \\ P_i^y \\ P_i^z \end{bmatrix} = T_{A_i}^V \cdot P_i^w = T_{A_i}^V \cdot \begin{bmatrix} R \cdot \sin \gamma_i \\ 0 \\ R \cdot \cos \gamma_i \end{bmatrix} \quad (4)$$

these equations can be obtained for our rover via the differences of the z -components of the four contact points

$$P_4^z = P_3^z - \cos \phi \cdot (2 \cdot l \cdot \sin \beta_R + R \cdot (\cos \gamma_4 - \cos \gamma_3)) \quad (5)$$

$$P_4^z = P_2^z - \cos \phi \cdot (t \cdot (\cos \beta_R - \cos \beta_L) + l \cdot (\sin \beta_R - \sin \beta_L) + R \cdot (\cos \gamma_4 - \cos \gamma_2)) - 2 \cdot w \cdot \sin \phi \quad (6)$$

$$P_4^z = P_1^z - \cos \phi \cdot (t \cdot (\cos \beta_R - \cos \beta_L) + l \cdot (\sin \beta_R + \sin \beta_L) + R \cdot (\cos \gamma_4 - \cos \gamma_1)) - 2 \cdot w \cdot \sin \phi \quad (7)$$

being R the radius of the wheel. Due to the presence of the mechanical differential in this system, an additional equation can be written relating the pitch θ to the angles β_R and β_L

$$\theta = \frac{\beta_R + \beta_L}{2} \quad (8)$$

In summary, inputs to the inverse kinematics problem are assumed to be a terrain elevation map (i.e., P_i and γ_i for each wheel), the position p_c of the rover center, and the rover heading ψ . Position and heading are taken as inputs since the goal of kinematic analysis is often to predict the traversability and stability at a given point in the terrain map. These inputs reduce the number of unknown parameters to four, which can be determined by solving the nonlinear system of equations (5)-(8). Numerical techniques such as Newton's method and steepest descent can be applied to this problem, although convergence is not guaranteed since the terrain elevation map is generally not represented by a continuously differentiable function [15].

3.2 ROVER FORCE ANALYSIS

Force analysis is another important aspect of rover mobility prediction. The speed of an autonomous vehicle on rough terrain must be limited in order to avoid shocks and for safety reasons. Furthermore, the computational cost is usually quite high (image processing, path planning, obstacle avoidance, etc.) and the onboard processing power is limited. This requires the rover to move slowly. In this range of speeds (typically 5 to 20 cm/s) and accelerations (typically 0.05 to 0.1% of g), the dynamic contributions can be neglected and a quasi-static model is appropriate. Such a model can be solved for contact forces and motor torques knowing the pose of the robot and the wheel-ground contact points.

Figure 7 is a diagram of a four-wheel mobile robot on uneven terrain. The vectors f_i represent the wheel-terrain interaction forces. The position vectors p_i are directed from the wheel terrain contact points to the rover center of mass. The vector f_s at the rover center of mass represents the summed effects of gravitational forces, inertial forces, forces due to manipulation, and forces due to interaction with the environment or other robots. Note that rover links, wheel and body masses are lumped at the center of mass. Note also that f_s can possess a user-defined component in the direction of desired motion. A set of quasi-static force balance equations for the rover shown in Figure 7 can be written as

$$\left[\begin{array}{c|c} I & \dots \\ \hline 0 & -p_1^z & p_1^y \\ p_1^z & 0 & -p_1^x \\ -p_1^y & p_1^x & 0 \end{array} \right] \left[\begin{array}{c|c} I & \\ \hline 0 & -p_4^z & p_4^y \\ p_4^z & 0 & -p_4^x \\ -p_4^y & p_4^x & 0 \end{array} \right] \begin{bmatrix} f_1 \\ \vdots \\ f_4 \end{bmatrix} = f_s \quad (9)$$

Where I represents a 3×3 identity matrix. This set of equations can be written in compact matrix form as:

$$G \cdot x = f_s \quad (10)$$

Equation (10) is usually referred to as the force distribution equation [16]. It consists of a set of 6 equations in 12 unknowns. Thus, the force analysis problem is under constrained and there exists an infinite set of f_i that balances the body vector f_s . In general, a system with m contact points possesses $2(m-1)$ degrees of redundancy. Solution methods of the distribution equations have been discussed in [17], [18], [19], where a solution x is found that optimizes a user-defined criteria. In order to reproduce the physical behavior of the robot, the optimization criterion should reflect the control strategy implemented onboard. For example, in [18] and [19], a solution to maximize traction was obtained by imposing equal friction coefficients on all wheels. The idea was to have the ratio of tangential and normal forces (see Figure 6) as low as possible by selecting the correct set of torques. However, direct measurement of the normal forces and the contact angles is difficult, making a similar control strategy very expensive in practice. In this paper, two optimization criteria are discussed and compared, based on the indirect

measurement of the tangential forces, which are roughly proportional to the electrical currents of the wheel motors[13]. This approach is easy to implement using inexpensive on-board ammeters.

3.2.1 Optimization criteria

The first method is aimed to minimize slippage. The fundamental problem for over-constrained rovers is that each wheel is controlled independently in a closed-loop manner, resulting in one wheel speeding up while another wheel slowing down to get up its speed set point, under different loading profiles. This produces slippage and tendency to sideslip as the suspension system traverses over obstacles. One way to reduce the occurrence of slippage is that of minimizing the differences between the tractive efforts produced by the robot's wheels. An objective function for optimization of the force distribution equations can be defined as

$$O_1 = \min \left(\sum (f_{t,i} - \bar{f}_t)^2 \right) \quad (11)$$

where $f_{t,i}$ is the tractive effort of the wheel i , expressed in the wheel reference frame, and \bar{f}_t is the mean of all $f_{t,i}$. A second optimization criterion for minimum power consumption can be developed based on the fact that the power consumed by a DC motor-driven wheeled vehicle using PWM amplifiers can be estimated by

$$P = \frac{r \cdot s^2 \cdot R^2}{K_t^2} \sum (f_{t,i})^2 \quad (12)$$

where $f_{t,i}$ is the i -th tractive force, r is the motor resistance, K_t is the motor torque constant, s is the motor gear ratio, and R is the wheel radius. Thus, to minimize power consumption, the control algorithm should seek to minimize the cost function

$$O_2 = \min(P) \quad (13)$$

In general, the smaller the objective function, the lower the likelihood of slippage or power consumption. We can formally state the optimization problem as follows: Minimize O_1 or O_2 subject to the equality constraint (10) and to the physical constraints of the system. One such

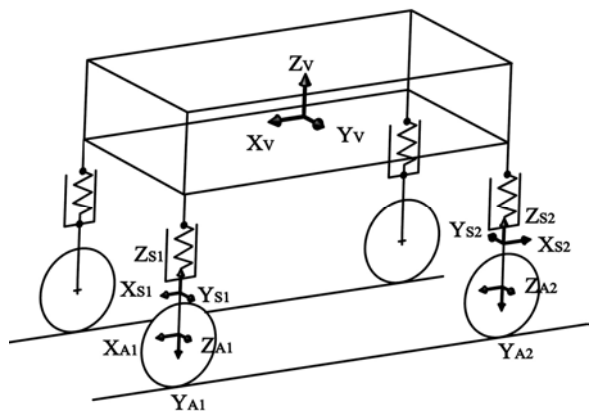


Figure 8 A conventional vehicle equipped with a spring suspension system.

constraint is that all rover wheels should remain in contact with the terrain. This can be expressed by ensuring that all wheel-terrain normal forces $f_{n,i}$ remain positive

$$f_{n,i} > 0 \quad i = 1, \dots, 4 \quad (14)$$

The second constraint is that the wheel torques must remain within the saturation limits of the actuator

$$\tau_{min} < (f_{t,i} \cdot R) < \tau_{max} \quad i = 1, \dots, 4 \quad (15)$$

The third is that the tractive force exerted on the terrain must not exceed the maximum force that the terrain can bear. The simplest approximation of this constraint is a Coulomb friction model

$$f_{t,i} < \mu \cdot f_{n,i} \quad i = 1, \dots, 4 \quad (16)$$

where μ is the wheel-terrain force coefficient. This approximation is reasonable for rigid wheels traveling over rigid terrain. For a generic rigid wheel on deformable terrain, the maximum shear strength of the terrain can be computed by the Coulomb-Mohr theory as

$$F_{max} = A \cdot (c + \sigma \cdot \tan \phi_t) \quad (17)$$

where A is the projected wheel area, c is the terrain cohesion, σ is the normal stress at the wheel-terrain interface, and ϕ_t is the internal friction angle [21]. Thus, the terrain strength constraint can be written for deformable terrain as

$$f_{t,i} < F_{max} \quad i = 1, \dots, 4 \quad (18)$$

Failure to find a vector x that satisfies (10) implies that the rover can not move in the direction of desired motion. Conversely, a large space of solution for x implies that the terrain is highly traversable. Thus, force analysis is an important part of rover traversability evaluation and it can be employed to develop efficient control algorithms on rough terrain.

4 MOBILITY ANALYSIS

In this section, the locomotion performance of the rover Dune is compared through simulations with a geometrically equivalent vehicle, employing a conventional spring-type suspension system. For simplicity, the comparative suspension is modeled as composed of four linear spring elements that constrain the wheels to move vertically with respect to the vehicle frame, as shown schematically in Figure 8. The spring rate is chosen to ensure a wheel travel of 35% of wheel radius under nominal working conditions, i.e. robot traveling on a flat surface. This is a typical value for off-road applications [22]. The obstacle-climbing ability of the two architectures is evaluated in terms of required friction coefficient and motor torque, change in load ratio, and power consumption. Inputs to the simulations are the vertical components of the wheel contact points P_i and angles γ_i . Their knowledge allows, firstly, the inverse kinematic problem, expressed by (5)-(8), to be solved, and, secondly, the wheel contact forces to be evaluated using (10). Simulations are run using both optimization criteria,

described in previous Section 3.2. The vector f_s at the rover center of mass is limited to the weight force of the rover. Two typical scenarios are considered. In the first simulation, the rover traverses over an obstacle of height up to one and half of the wheel diameter. In the second simulation, Dune drives up to a slope, while traversing simultaneously over obstacles.

4.1 OBSTACLE-CLIMBING ABILITY

The behavior of the two types of robot architecture is analyzed during the traverse of a large single rock, when one wheel of the rover, i.e., left front Wheel 1, rises higher than the other three wheels that remain approximately in contact with the ground plane. The rock is modeled for simplicity as a step-obstacle, which, however, represents a worst-case condition. The height of the rock is initially set as half of the wheel radius ($h = 50$ mm). Figure 9 shows the variation of the contact angle γ_1 (refer to Figure 6 for more details), during the entire climbing stage. The initial peak

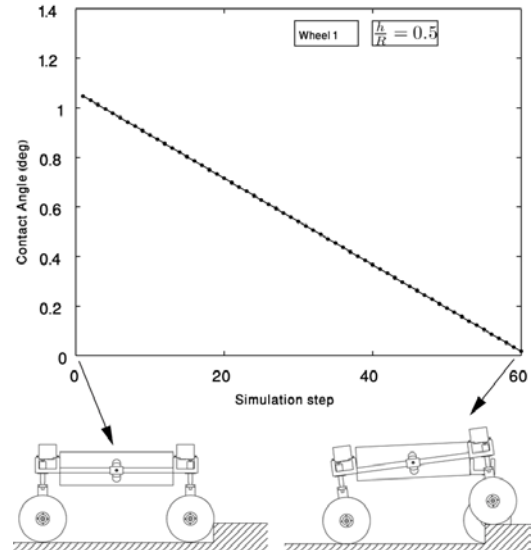


Figure 9 Change in the contact angle of Wheel 1 during step-climbing.

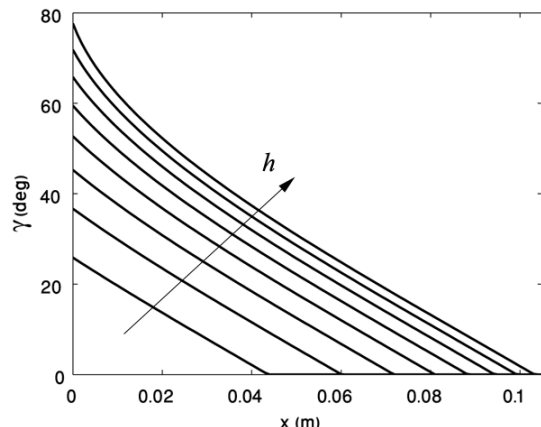


Figure 10 Change in the contact angle of Wheel 1 during step-climbing.

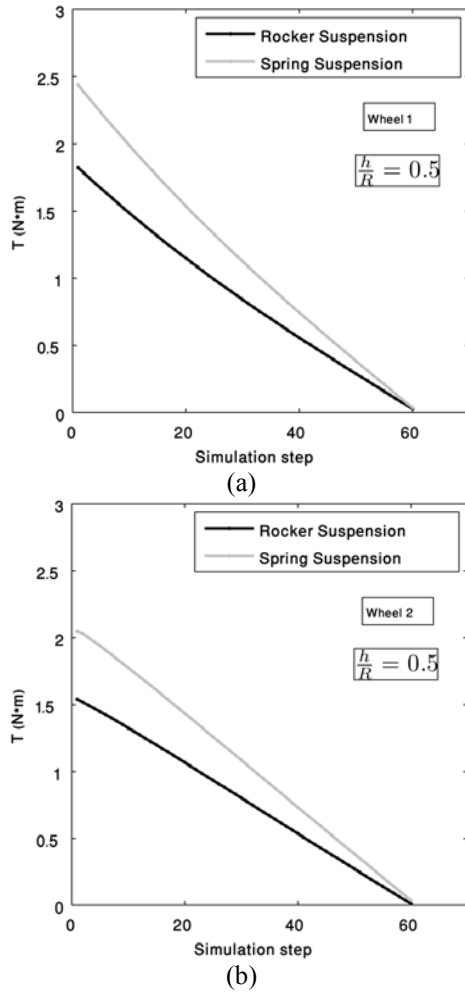


Figure 11 Torque demand for Wheel 1 (a) and Wheel 2 (b), during the step-climbing operation. Note that the slip minimization-based optimization was used in the simulation.

γ_1^{\max} corresponds to Wheel 1 in contact with the vertical wall of the step

$$\gamma_1^{\max} = \arccos\left(1 - \frac{h}{R}\right) \quad (19)$$

whereas γ_1 nulls out when Wheel 1 is on the top of the step. If γ_1 is plotted against the longitudinal displacement of the vehicle rear axis for increasing values of h and constant speed of the robot, as shown in Figure 10, the curves can be approximated by linear equations without losing much accuracy. This suggests a more physics-based interpretation of the diagram in Figure 9 as a function of time instead of simulation step.

4.1.1 Slip minimization-based optimization

Firstly, the slip minimization based optimization approach is adopted. The simulation results are collected in the following Figure 11 and Figure 12. Specifically, the torque required by Wheel 1 and Wheel 2 during the climbing maneuver is shown in Figure 11(a) and Figure 11(b), respectively. Note that these two wheels carry most of the

tractive effort, whereas the torques developed by the remaining wheels are negligible and omitted for readability's sake. The rocker-type suspension ensures a lower torque demand than the spring-type system, during the entire maneuver. This is beneficial for a robot, allowing smaller and lighter drive-motors to be used. The difference between the two suspension solutions can be explained when considering Figure 12, where the change in the load ratio of the four wheels is shown. The rocker-type suspension provides a better and more uniform weight distribution, whereas, in the spring-type solution, climbing Wheel 1 and cross-coupled Wheel 3 are rapidly loaded, and Wheel 2 and Wheel 3 are accordingly unloaded. The advantage of using a rocker type suspension system is clearly demonstrated in terms of better traction performance. In general, the tractive thrust that a soil can support increases with increasing normal force. The lower the vertical load, the worse the traction ability. The effectiveness of the rocker suspension is still confirmed, when considering the minimum friction coefficient required to traverse the obstacle, i.e. $\mu = f_t/f_n$. The smaller the friction coefficient, the better the climbing ability of the system. If we focus on the worst-case condition at the beginning of the climbing stage, the rocker suspension requires a friction coefficient of $\mu=0.60$ against a value of $\mu=0.67$, needed by the spring suspension. Additionally, the rocker-type system provides lower power consumption ($P/k_p = 568 \text{ N}^2$, see Table IV for more details), when compared with the spring system ($P/k_p = 1014 \text{ N}^2$).

4.1.2 Power consumption-based optimization

Secondly, the climbing performance of the two suspension systems is evaluated optimizing the power consumption. The torque required by Wheel 1 and Wheel 2 is shown in Figure 13(a) and Figure 13(b), respectively. The rocker-type suspension still outperforms the spring counterpart. Again, the variation in the weight distribution is favorable for the rocker suspension. The results are very similar to those obtained for the slip-based optimization (see Figure 12) and they are omitted here. When considering the minimum friction coefficient required to traverse the obstacle, the rocker suspension requires a friction coefficient of $\mu=0.82$ against a value of $\mu=0.89$, needed by the spring suspension. Overall, the advantage of adopting the rocker-type suspension in terms of traction performance and climbing ability is confirmed.

Finally, Table IV collects the results of a side by side comparison between the two proposed optimization methods. As expected, the power consumption-based optimization ensures longer autonomy ($P/k_p = 528 \text{ N}^2$).

However, the slip minimization based approach offers a better trade-off solution between the best climbing ability ($\mu=0.6$) and a slightly increased power demand ($P/k_p = 568 \text{ N}^2$) of 7.5% with respect to the alternative method. Therefore, the slip minimization-based optimization is

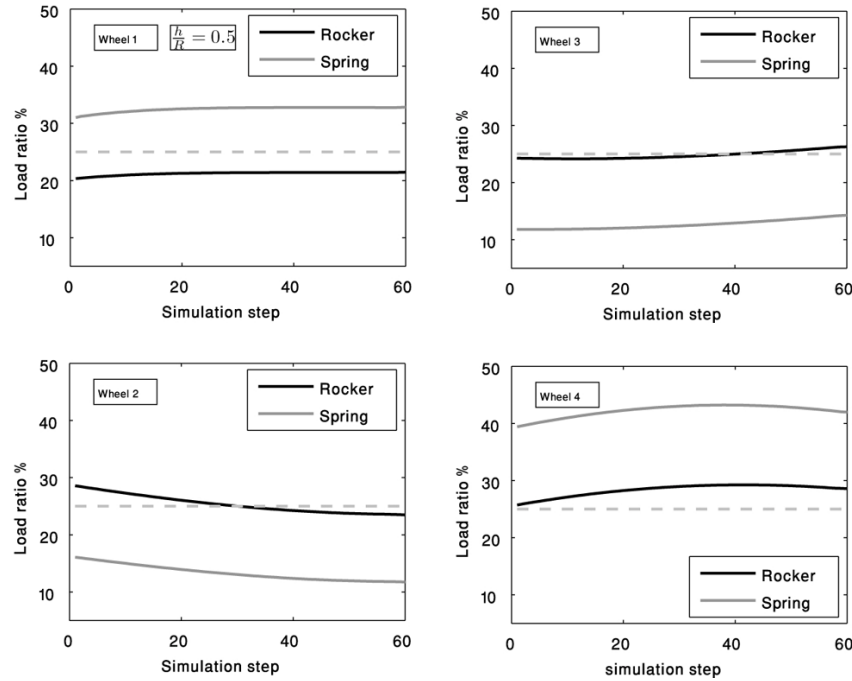


Figure 12 Wheel load ratio variation during the step-climbing stage. It should be noted that the load ratio refers to the normal force estimated in the wheel frame, i.e. $f_{n,i}$.

chosen as the best control strategy, and adopted in all the following simulations.

The step-climbing analysis of the rocker suspension system is extended increasing the height of the obstacle progressively up to 300% of the wheel radius. We refer to the final stage of the climbing maneuver when Wheel 1 is on the top of the step. Figure 14(a) shows the change in the roll and pitch angles of the rover as function of the obstacle height. While both solutions provide similar results with a slightly larger roll angle for the spring-type system, the rocker suspension clearly ensures a better weight distribution. This is demonstrated by Figure 14(b) where the change in the wheel load ratio is shown for increasing rock height. The rocker suspension confirms its good performance, maximizing the traction performance and improving the rollover stability of the vehicle. Even with an obstacle as much height as one and half of the wheel diameter ($h = 300$ mm), all wheels still keep in contact with the ground and Wheel 1, which results in the “lightest” wheel, keeps almost half of its nominal traction power. More detailed results are collected in Table III. Conversely, if a conventional spring suspension system is employed, obstacles of small dimension will result in large variations of weight distribution. Wheel 1 and the rear wheel of the opposite side, namely Wheel 4, are rapidly loaded while weight is shifted from the remaining two wheels, Wheel 2 and 3, until they lose contact with the ground. This happens for a rock height of about 90% of the wheel radius ($h = 88$ mm), resulting in a reduction of almost half of the vehicle tractive power and in an impending instability condition of the robot.

In general, conventional suspension systems greatly reduce the load and therefore the traction on wheels that are

extended to lie below the level of the other wheels. This increases the load and traction of any one raised wheel. The rocker avoids this by having a chassis supported on a central pivot, which ensures equal distribution of load on all wheels, and therefore equal traction on each wheel. If a stiff suspension system is used, the chassis will be considerably deflected, when any one of the wheel is deflected. A reduction of weight shift to an extended or retracted wheel and the reduction of body movement can be achieved by using low rate springs to support the body on the wheels. However, this method would result in an undesirable low oscillation frequency, usually referred to as “too soft a suspension”.

4.2 SLOPE TRAVERSE

In this second scenario, the rover climbs over a bump with one wheel, while simultaneously driving uphill. A slope of 10 deg is initially set, varying the height of the obstacle up to 100% of the wheel diameter. The results are shown in Figure 15(a). For readability’s sake, only the wheel of either configuration, which experiences the maximum reduction in vertical load, is shown, i.e. the wheel that surmounts the obstacle in the rocker system, and the wheel that is extended below the level of the others in the spring counterpart. Once again, the rocker suspension system ensures a more uniform weight distribution as the vehicle conforms to the terrain morphology. Obstacle negotiation using a conventional suspension system is bounded by a maximum obstacle height of 72 mm (72% of wheel radius). For this step height, the vertical load acting on Wheel 2 nulls out and the wheel loses contact with the ground.

Finally, an analysis of weight distribution on the same wheels is shown in Figure 15(b) by varying the slope

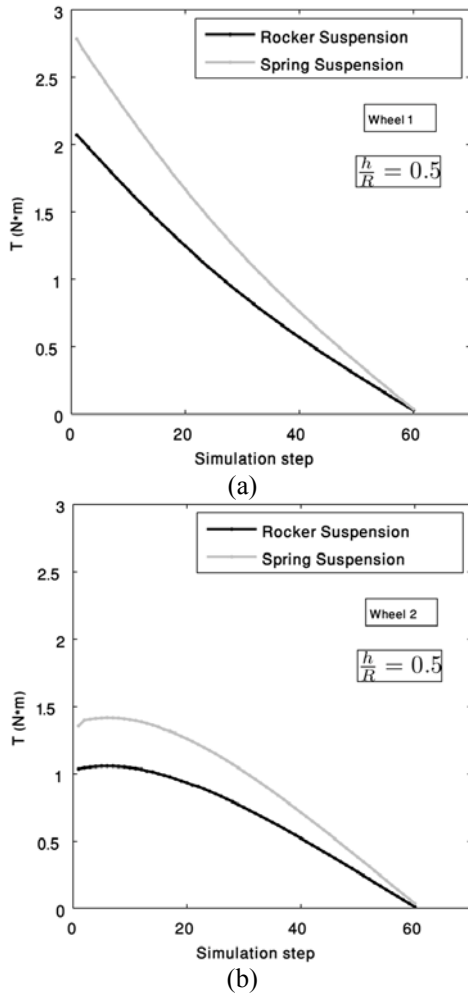


Figure 13 Torque requirement for Wheel 1 (a) and Wheel 2 (b) during a complete step climbing operation. Note that the power consumption-based optimization was used in the simulation.

inclination and keeping a constant obstacle height of 50 mm (50% of wheel radius). Again, the rocker suspension provides the best results, allowing the vehicle to traverse steeper slopes with respect to the conventional vehicle, which, conversely, is able to drive only up to a 25-degree inclination, when Wheel 2 loses contact with the ground.

5 CONCLUSIONS

This paper evaluated the locomotion performance of a robot endowed with advanced mobility features to traverse natural outdoor terrain. The vehicle adopted an independently controlled 4-wheel-drive/4-wheel-steer architecture, and employed a passive rocker-type suspension system to improve its ability to climb up obstacles, while ensuring good traction and stability performance. A comparison with a conventional vehicle adopting a spring-type suspension was performed through simulations, using a kinematic and force model that demonstrated its advantages and overall better performance.

REFERENCES

- [1] Sandin P., *Robot Mechanisms and Mechanical Devices*, McGraw Hill, New York, NY, 2003.
- [2] Maimone M., Johnson A., Willson R., and Matthies L., Autonomous navigation results from the Mars exploration rover (MER) mission, *Intern. Symp. Experimental Robot*, Singapore, 2004.
- [3] Siegwart R., Lamon P., Estier T., Lauria M., and Piguet R., Innovative design for wheeled locomotion in rough terrain, *J. Robot. Auton. Syst.*, Vol. 40, pp. 151-162, 2003.
- [4] Moorehead S., Simmons R., Apostolopoulos D., and Whittaker W.L., Autonomous Navigation Field Results of a Planetary Analog Robot in Antarctica, *Intern. Symp. on Artificial Intelligence, Robotics and Automation in Space*, 1999.
- [5] Christian D., Wettergreen D., Bualat M., Schwehr K., Tucker D., Zbinden E., Field Experiments with the Ames Marsokhod Rover, *Field and Service Robotics Conference*, Canberra, Australia, 1997.
- [6] Matthies L. et al, A portable, autonomous, urban reconnaissance robot, *Robotics and Autonomous Systems*, Vol. 40, No. 2-3, 2002, pp. 163-172.
- [7] Klinkner S., Lee C., Wagner C., Hlawatsch W., Schreyer A., Röser H., Destination Moon and beyond for the Microrover Nanokhod, *DGLR International Symposium*, Bremen, Germany, 2007.
- [8] Melzer K. and Swanson G., Performance Evaluation of a Second-Generation Elastic Loop Mobility System, *WES Technical Report*, M-74-7, 1974.
- [9] Bares J. and Wettergreen D., Dante II: Technical Description, Results and Lessons Learned, *Intern. Journal of Robotics Research*, Vol. 18, No. 7, pp. 621-649, 1999.
- [10] Bickler D., Roving over Mars, *Mechanical Engineering Magazine*, American Society of Mechanical Engineers, 1998.
- [11] Denavit J. and Hartenberg R., A kinematic notation for Lower-Pair Mechanisms based on Matrices, *ASME J. Applied Mechanics*, Vol. 22, pp. 215-222, 1955.
- [12] Tarokh M., McDermott G., Hayati S. and Hung J., Kinematic Modeling of a High Mobility Mars Rover, *IEEE Intern. Conference on Robotics and Automation*, pp. 992-998, 1999.
- [13] Reina, G., Rough Terrain Mobile Robot Localization and Traversability with Applications to Planetary Explorations, *PhD Thesis*, Politecnico of Bari, Italy, 2004.
- [14] Eckhardt H., *Kinematic Design of Machines and Mechanisms*, McGraw-Hill, New York, NY, 1989.
- [15] Hacot H., Analysis and Traction Control of a Rocker-Bogie Planetary Rover, *M.S. Thesis*, Massachusetts Institute of Technology, Cambridge, MA, 1998.

- [16] Kumar V., Waldron K., Force Distribution in Closed Kinematic Chains, *IEEE Transactions on Robotics and Automation*, Vol. 4, No. 6, pp. 657-644, 1988.
- [17] Sreenivasan S., Actively Coordinated Wheeled Vehicle Systems, *PhD Thesis*, Ohio State University, Columbus, OH, 1994.
- [18] Iagnemma K., Rough-terrain Mobile Robot Planning and Control with Application to Planetary Exploration, *PhD Thesis*, MIT, Cambridge, MA, 2001.
- [19] Thueer T., Krebs A., and Siegwart R., Comprehensive Locomotion Performance Evaluation of All-Terrain Robots, *IEEE/RSJ Inter. Conf. on Intelligent Robots and Systems*, Beijing, China, 2006.
- [20] Ojeda L., Cruz D., Reina G., and Borenstein J., Current-based Slippage Detection and Correction for Mobile Robots and Planetary Rovers, *IEEE Transactions on Robotics*, Vol. 22, No. 2, pp. 366-378, 2006.
- [21] Bekker G., *Introduction to Terrain-Vehicle Systems*, University of Michigan Press, 1969.
- [22] Wong J., *Theory of Ground Vehicles*, Wiley-Interscience, New York, NY, 2001.

Table III - Comparison between rocker and spring suspension system in terms of step-climbing ability ($h/R = 0.5$). Method 1 refers to the slip minimization-based optimization, whereas Method 2 to the power consumption-based approach. Note that the constant k_p is defined as $k_p = (r \cdot s^2 \cdot R^2) / K_t^2$, see (12) for more detail

| Suspension type | Method 1 | | | | Method 2 | | | |
|-----------------|---------------|---------------|-------|-----------------------------------|---------------|---------------|-------|-----------------------------------|
| | τ_1 (Nm) | τ_2 (Nm) | μ | $\frac{P}{k_p}$ (N ²) | τ_1 (Nm) | τ_2 (Nm) | μ | $\frac{P}{k_p}$ (N ²) |
| Rocker | 18.2 | 15.4 | 0.60 | 568 | 20.1 | 10.4 | 0.82 | 528 |
| Spring | 24.3 | 20.6 | 0.67 | 1014 | 27.8 | 13.6 | 0.89 | 956 |

Table IV - Change in wheel weight distribution for increasing step-height. See Figure 14 for detailed results. ΔW_i is defined as the percentage relative variation of vertical load of wheel i with respect to the case of uniform weight distribution and the vehicle traveling on a horizontal plane

| Rock height (mm) | Rocker suspension | | | | Spring suspension | | | |
|------------------|-------------------|------------------|------------------|------------------|-------------------|------------------|------------------|-----------|
| | ΔW_1 (%) | ΔW_2 (%) | ΔW_3 (%) | ΔW_4 (%) | ΔW_1 (%) | ΔW_2 (%) | ΔW_3 (%) | W_4 (%) |
| 10 | -2.6 | -0.1 | 1.1 | 2.1 | 9.1 | -11.8 | -8.20 | 10.8 |
| 20 | -5.7 | -1.3 | 2.2 | 5.2 | 18.3 | -23.7 | -16.4 | 21.6 |
| 30 | -8.4 | -2.4 | 3.3 | 8.3 | 27.5 | -35.5 | -24.8 | 32.3 |
| 40 | -11.8 | -4.6 | 4.4 | 11.1 | 36.7 | -47.4 | -33.2 | 43.0 |
| 50 | -14.1 | -5.8 | 5.4 | 13.4 | 45.9 | -59.2 | -41.8 | 53.7 |
| 60 | -17.3 | -7.0 | 6.6 | 16.4 | 55.2 | -71.0 | -50.6 | 64.3 |
| 70 | -19.5 | -8.2 | 7.8 | 18.6 | 64.6 | -82.8 | -59.5 | 74.9 |
| 80 | -21.6 | -9.4 | 8.4 | 21.1 | 74.0 | -94.6 | -68.7 | 85.5 |
| 90 | -24.6 | -10.6 | 9.6 | 23.6 | 77.9 | -99.3 | -72.5 | 89.8 |
| 100 | -27.6 | -11.8 | 25.5 | | | | | |
| 110 | -30.4 | -12.0 | 27.5 | | | | | |
| 130 | -36.9 | -15.4 | 30.3 | | | | | |
| 160 | -39.6 | -17.9 | 33.4 | | | | | |
| 190 | -42.6 | -22.3 | 38.9 | | | | | |
| 220 | -47.7 | 26.6 | 46.4 | | | | | |
| 240 | -51.4 | -28.7 | 48.5 | | | | | |
| 260 | -54.8 | -29.7 | 52.4 | | | | | |
| 280 | -58.7 | -30.1 | 57.8 | | | | | |
| 300 | -62.3 | -30.8 | 60.6 | | | | | |

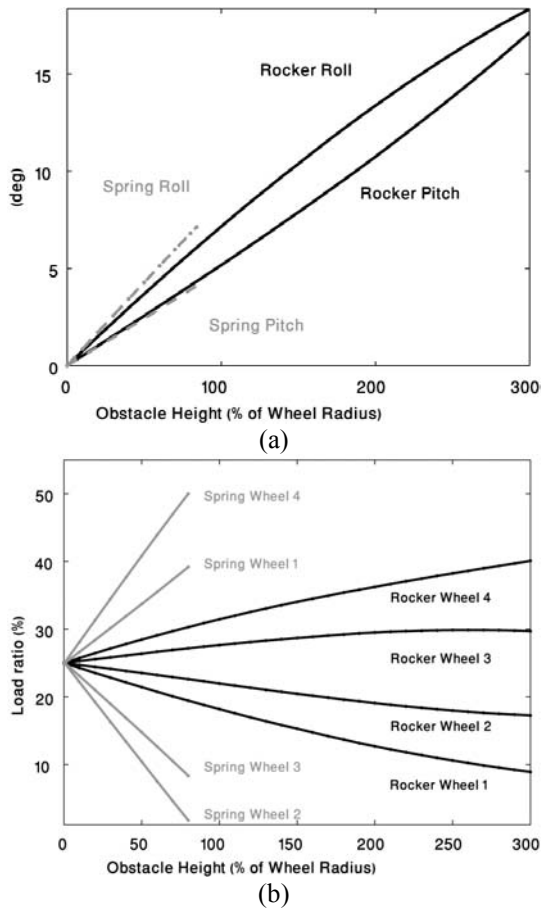


Figure 14 Step-climbing ability for increasing obstacle height: (a) tilt, and (b) weight distribution. Note that the pitch angle is negative and here its absolute value is plotted for simplicity.

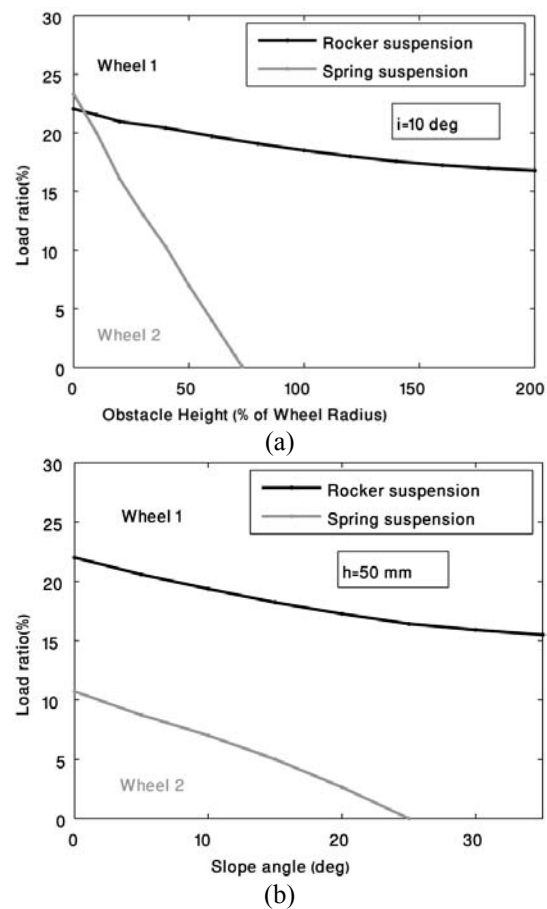


Figure 15 Slope traverse: variation in load ratio. Case (a): constant slope of 10 deg with increasing step height, Case (b): constant rock height of 50 mm with increasing slope inclination.

INPUT SHAPING FOR SLOSH-FREE MOVING CONTAINERS WITH LIQUID

Peter Hubinský Thomas Pospiech

Slovak University of Technology in Bratislava, Slovakia
Faculty of Electrical Engineering and Information Technology
Institute of Control and Industrial Informatics

ABSTRACT

This paper describes a method for slosh-free moving of containers with liquid. It shows, by means of experimental results, that a container filled with liquid can be regarded as a damped pendulum. With respect to the industrial application, a feed-forward control is used to transfer the container in horizontal direction without sloshing. The principle structure, calculations, time duration and the robustness of the three basic types of input shaper are described and compared to each other. Finally, a possibility of integration into a drive control and the principle software implementation are presented.

Keywords: liquid container transfer, elimination of residual vibration, input signal shaping, robustness

1 PROBLEM COMPILATION

If state-of-the-art filling systems for liquid food as for example milk or yogurt are regarded, it stands out that those systems are operated in a fully automated way and the complete working process is running without any impact of persons. The process is controlled by numerous sensors and various actuators.

For the actual function of these systems, two main requirements must be fulfilled next to the procedural challenges as for example cleaning the container before the liquid is filled in: On the one hand, the container must be filled with the corresponding liquid and on the other hand it must be sealed afterwards.

In industrial application, two basic concepts for an operation mode are distinguished from each other: continuous and discontinuous operation.

During continuous operation, the containers are conveyed on conveyor belts. The single working stations or production steps, as for example container cleaning, filling and sealing do not stop the conveyor belt i.e. they are carried along with the containers. The mechanical and electrical efforts of such machines are significant and thus correspondingly cost-intensive.

With discontinuous (clocked) machines, the above mentioned operation steps are static. The conveying belt with the containers must be stopped and started for every filling sequence.



Figure 1 Discontinuous filling plant [OYSTAR Gasti].

This modular and economic design is opposed by a critical operational range. After the containers have been filled with the corresponding liquid, several operation sequences pass by until they are sealed. The critical area is the result of starting and stopping the conveyor belt which leads to the liquids in the containers being initiated to move. If this movement becomes too heavy, the liquid spills over the containers. As soon as the cup seam is contaminated (in this case by the liquid), the cap cannot be sealed any more onto the cups respectively the containers cannot be hermetically

Contact author: Doc. Ing. Peter Hubinský, PhD.

Slovenská Technická Univerzita,
Bratislava Ilkovičova 3,
E-mail: hubak@elf.stuba.sk

sealed. Apart from that, figure 1 indicates that this operational area is sterile and therefore spilled liquid would imply increased cleaning efforts.

On the other hand a maximum production output is always aspired, which leads to a minimum process (moving) period. Together with the actual filling procedure (feeding the liquid into the container), this time is the longest process period with those kinds of lines.

The specified problem can therefore be summarized as follows: Directly after stopping the conveyor belt, the liquid must be calm which means it must not perform any movements (resonance!). Furthermore, a maximum deflection of the liquid within the container at a minimum process period must not be exceeded.

2 EXPERIMENTAL SET-UP

The experimental set-up represents the “practical” foundation for model verification, parameter identification and testing of control methods.

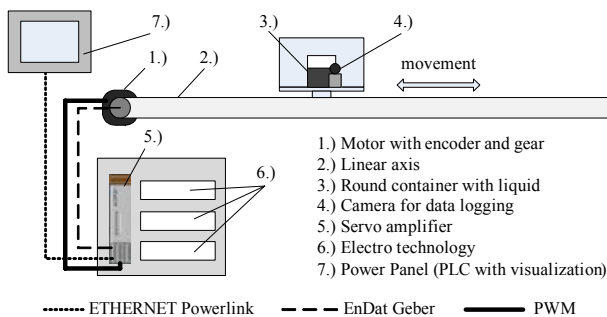


Figure 2 Scheme of experimental set-up.

This test set-up has a total length l of 2500 mm and allows for traverse paths of at most 1900 mm. In order to achieve the highest level of precision and dynamics with positioning or traversing, all utilised components are purchased from leading industrial manufacturers. The communication between the PLC and the servo amplifier is 1.2 ms, that means, in this cycle time the electrically commutated synchronous motor gets new reference values from the PLC via the servo amplifier. The positioning of the container is indirectly measured by the encoder system of the servo motor. Deformations of the tooth belt in the linear axis can be neglected. That means, also the actual velocity and acceleration are calculated in the servo amplifier based on the signal from the encoder system. The accuracy of the complete electromechanical part is about ± 0.1 mm.

As for the measurement of the liquid surface, a vision system is used. The camera sends the pictures online via USB to a PC with 100 fps (frames per second, meaning 100 Hz sampling rate). The resolution of measuring the liquid surface is about 0.1 mm (depending on the geometry of the utilized container, meaning the area of interest).

3 MODEL ANALYSIS

Related works [1]-[3] show that liquid sloshing in a three-dimensional container can be approximated as a two-dimensional phenomenon if the observed liquids possess the following characteristics:

- no modification of viscosity caused by temperature T , pressure p , time t ,
- density ρ is constant (incompressible liquid),
- newton-fluid (no shearing stress occurs [1],[2]).

A further assumption is that no deformations occur at the outside walls of the container, i.e. the geometry of the containers is steep and not flexible.

3.1 MODELING

According to the assumption above the liquid sloshing phenomenon can be deduced as a damped pendulum-model [3] and [4].

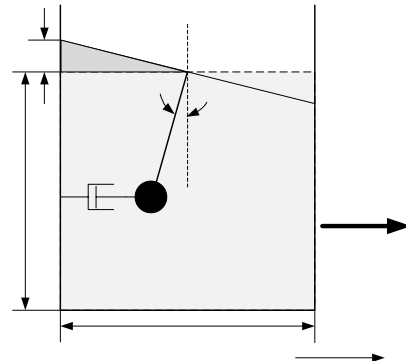


Figure 3 Approximated model of container with liquids.

The equation of motion deviated from this figure can be expressed in the following formula:

$$J \frac{d^2\theta}{dt^2} = -c \cdot l^2 \cdot \frac{d\theta}{dt} \cdot \cos^2 \theta - m \cdot g \cdot l \cdot \sin \theta + m \cdot a_x \cdot l \cdot \cos \theta \quad (1)$$

A corresponding correlation between the deflection h_s and the angle Θ can be extracted from figure 3 and results in:

$$h_s = \frac{L}{2} \cdot \tan(\theta) \quad (2)$$

with,

| | |
|----------|--|
| J | Mass moment of inertia ($J = m \cdot l^2$) |
| Θ | Deviation angle of the surface of the liquid |
| a_x | Acceleration of the container ($a_x = \ddot{x}$) |
| g | Acceleration of gravity |
| h_s | Deviation at the left cup wall |
| m | Liquid's mass |
| L | Diameter of cup |
| c | Parameter of viscosity |
| l | Pendulum length (virtually) |

All above listed parameters can be measured in a relative simple way except c and l .

The non-linear, inhomogenous second order differential equation (1) and (2) can be approximated for smaller angles of θ in the following way:

$$\ddot{\theta} = -\frac{c}{m}\dot{\theta} - \frac{g}{l} \cdot \theta + \frac{1}{l}\ddot{x} \quad (3)$$

$$h_s = \frac{L}{2} \cdot \theta \quad (4)$$

The transfer function $G_{FLC}(s)$ can now be extracted from those equations by applying the Laplace transformation in the picture area.

$$G_{FLC}(s) = \frac{H_s(s)}{A(s)} = \frac{K \cdot \omega_0^2}{s^2 + 2 \cdot D \cdot \omega_0 \cdot s + \omega_0^2} \quad (5)$$

with the parameters:

$$a(t) = \ddot{x}(t), \quad K = \frac{L}{2 \cdot g}$$

$$\omega_0 = \sqrt{\frac{g}{l}}, \quad D = \frac{c}{2 \cdot m} \cdot \sqrt{\frac{l}{g}} \quad (6)$$

3.2 IDENTIFICATION OF PARAMETERS

If the parameters in (6) are regarded, it becomes obvious that there are too many unknowns without the corresponding test series. The following parameters can be identified without major difficulties:

K: Since the gravity acceleration of $9,81 \text{ m/s}^2$ is known, merely the container's diameter L must be measured.

m: The liquid's mass can be determined by weighing directly or via the volume.

According to [3] and [5], there is an interesting theoretical correlation between filling level h , container's diameter L and the natural frequency f_n :

$$f_n = \frac{\sqrt{g \cdot \left(\frac{\pi}{L}\right) \cdot \tanh\left(\left(\frac{\pi}{L}\right) \cdot h\right)}}{2 \cdot \pi} \quad (7)$$

If thereby the diameter of the container is assumed as known, the natural frequency against the filling level of the liquid is received as the following figure shows:

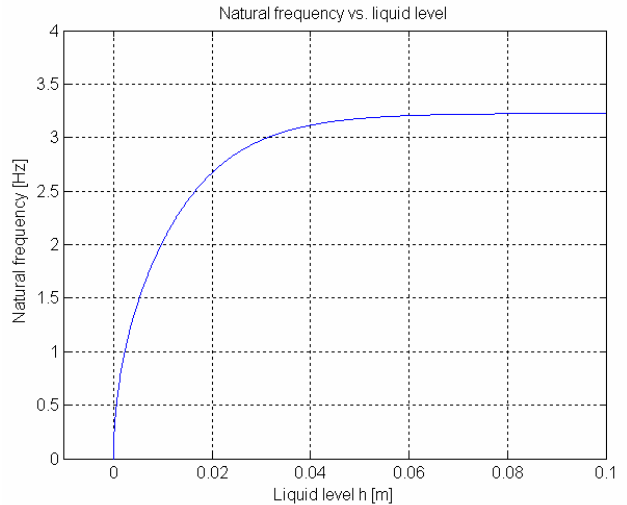


Figure 4 Natural frequency against the liquid level (diameter of the container $L=0,075 \text{ m}$).

For the identification of the parameters angular frequency ω_0 and system damping D , an impulse response of the system gives enough oscillations for analysing, as the following picture shows.

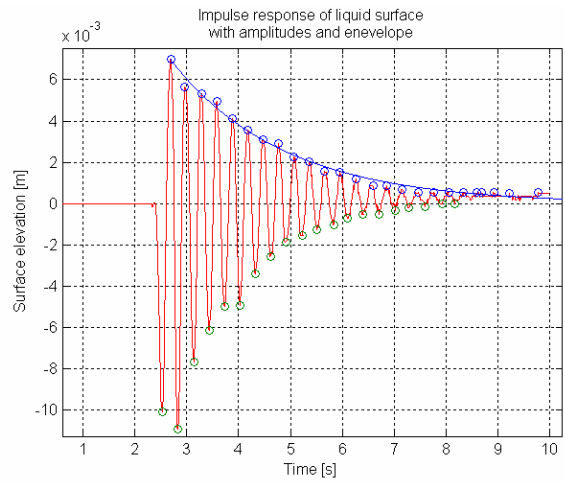


Figure 5 Impulse response of the system $a = 2 \text{ m/s}^2$ to $v = 0.2 \text{ m/s}$.

The logarithmic decrement Λ is the logarithmical amplitude ratio of two sequential amplitudes:

$$\Lambda = \ln \left| \frac{A_{k+1}}{A_k} \right| \quad (8)$$

The system damping can now be directly calculated from this according to [6]:

$$D = \frac{1}{\sqrt{1 + \left(\frac{\pi}{\Lambda}\right)^2}} \quad (9)$$

In such kind of a second order system the distances of the oscillation amplitudes are constant (see figure 5). The periodic time of the damped system is calculated from the time period T_d of two consecutive amplitudes as follows:

$$T_d = t_{k+1} - t_k \quad (10)$$

Resulting from that, the natural frequency and the angular frequency of the damped system can afterwards directly be calculated.

$$f_d = \frac{1}{T_d} \quad (11)$$

Next to the impulse response, figure 5 additionally shows the average envelope of the amplitude $h_{env}(t)$. With this average envelope, measuring errors, for example, can be detected and evaluated. Furthermore, this curve provides an even better overview. The following equation shows the calculation used for this purpose:

$$h_{env}(t) = A_1 \cdot e^{-\delta \cdot t} \quad (12)$$

whereas,

$$\delta = \frac{\Lambda}{T_d} \quad (13)$$

If now the natural angular frequency is converted into the natural frequency, the measured values can be controlled by comparing the value f_0 (here: $f_0 = 3,26 \text{ Hz}$) at a liquid filling level (here: $h = 0,055 \text{ m}$) to figure 4. As a result, it can be put on record that the theoretically and experimentally collected values sufficiently correspond.

The single parameters from (6) can be calculated without any difficulties. The table below gives a summarising overview for this purpose.

Table I – Overview of system parameters (here: water)

| Parameter | Value | Unit |
|-------------------------------|--------|-----------------------------|
| Gain, K | 0,0038 | s^2 |
| Gravitation, g | 9,81 | m/s^2 |
| Lenght of pendulum, l | 0,023 | m |
| Angular frequency, ω_0 | 20,51 | rad/s |
| Damping, D | 0,035 | - |
| Mass, m | 0,243 | kg |
| Coefficient of viscosity, c | 0,829 | $\text{mPa} \cdot \text{s}$ |
| Diameter container, L | 0,075 | m |
| Liquid level, h | 0,055 | m |

4 INPUT SHAPING

The basis of all algorithms in this area is spectral conditioning of the control signal in that way that any spectral component close to the natural frequency of the controlled mechanic system is eliminated. In turn, the idea of input shaping is to convolute the control signal at specific points of time by Dirac impulses. The figure below shows the impact of the impulses on an oscillatory system as a transfer function according to (5):

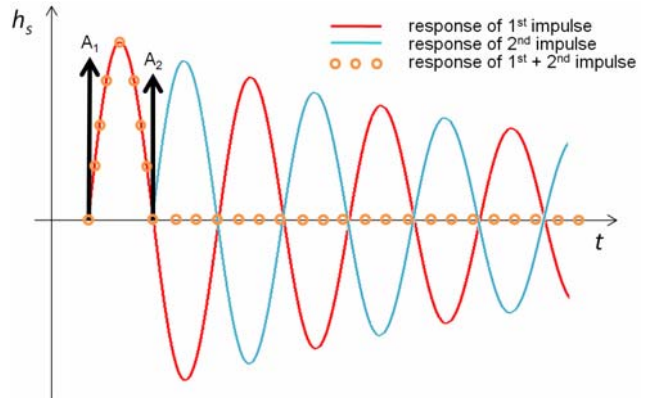


Figure 6 Impulse responses of a second order oscillatory system.

After the second impulse, the overlapping of the two oscillations results in elimination so that no residual oscillations remain afterwards.

According to [7] and [8], the impulse system responses can be calculated as follows:

$$\sum_i^n A_i \cdot e^{-j \cdot D \cdot \omega_0 \cdot t_i} = 0 \quad (14)$$

and to obtain a normalized result:

$$\sum_{i=1}^n A_i = 1 \quad (15)$$

After at least two impulses, equation (14) can be set to zero, which in turn shows the elimination of the oscillation.

These facts allow for deviating different types of input shapers.

4.1 ZV INPUT SHAPER

According to [7]-[10], the ZV input shaper (zero vibration input shaper) possesses a minimum amount of two impulses and thus shows the shortest delay of control time.

Upon calculation of (14) and considering (15), the amplitude and time values for this input shaper result in:

$$A_1 = \frac{k}{1+k} \quad (16)$$

$$A_2 = \frac{1}{1+k}$$

with

$$k = e^{\frac{D \cdot \pi}{\sqrt{1-D^2}}} \quad (17)$$

and

$$t_1 = 0$$

$$t_2 = \frac{T_D}{2} \quad (18)$$

The amplitude and time values at last solely depend on the periodic time of the damped system T_D and on the damping D . If now (any) input variable is convoluted by those two impulses, the oscillations will be eliminated after the second impulse due to the filtered reference variable. The figure below shows the principle functionality of the convolution (here: $\Delta t = T_D/2$).

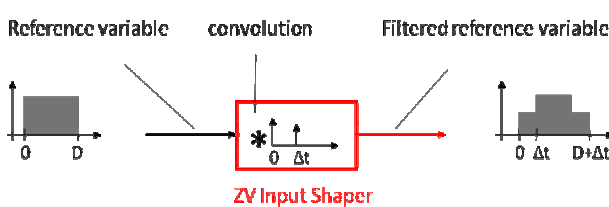


Figure 7 Principle functionality of the ZV input shaper (deformation of the acceleration profile).

If now the input signal, filtered via the ZV shaper respectively acceleration profile is regarded, it turns out that the control period is prolonged against the original signal (here: rectangular shape) by half a periodic time.

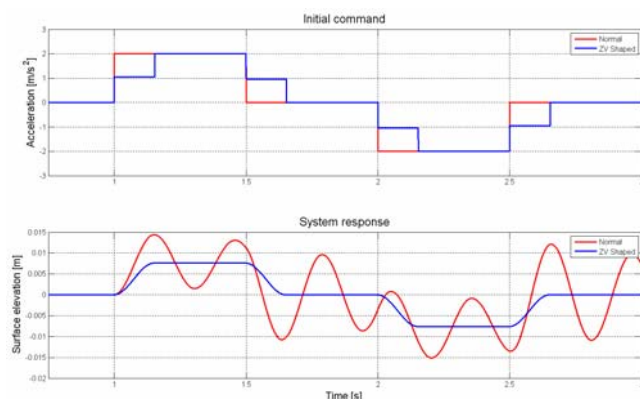


Figure 8 Acceleration with ZV shaper, filtered and system response (deflection of the surface of the liquid).

This figure indicates that the deflection of the liquid does not show any oscillations any more. The advantage of this method is that already during acceleration phase, any natural frequencies are eliminated. Thus, there are no longer any oscillations at a constant speed ($a = 0$). The ZV shaper is the fastest input shaper (with the shortest duration

time) but also the one with the most sensitivity to modeling errors or changing frequency during the process (\rightarrow residual vibrations).

4.2 ZVD INPUT SHAPER

According to [7], [9] and [10] the ZVD input shaper is an extended version of the ZV shaper. In this respect, two interpretations form the basis for this theory. The ZVD input shaper receives its name from an additional condition (D for derivative \rightarrow zero vibration and derivative).

$$\frac{d}{d\omega} \sum_i^n A_i \cdot e^{-j \cdot D \cdot \omega_0 \cdot t_i} = 0 \quad (19)$$

In consideration of (15), (19) results in three amplitudes with different amplitude values and time values:

$$\begin{aligned} A_1 &= \frac{1}{(1+k)^2} \\ A_2 &= \frac{2 \cdot k}{(1+k)^2} \\ A_3 &= \frac{k^2}{(1+k)^2} \end{aligned} \quad (20)$$

and

$$t_1 = 0$$

$$t_2 = \frac{T_D}{2} \quad (21)$$

$$t_3 = T_D$$

A convolution by two ZV shapers gives a further interpretation of the present issue. The following figure is to point this out.

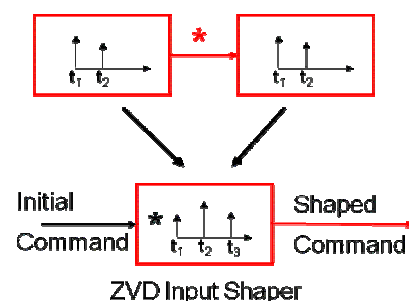


Figure 9 Generation of the ZVD input shaper.

Equation (21) shows that, with the ZVD shaper, the control period is prolonged compared to the original reference input variable by the period T_D .

The figure below shows a corresponding acceleration profile and the system response resulting from this profile. Furthermore a 10% error in system frequency is simulated here. Moreover, the ZV shaper is compared to the ZVD shaper.

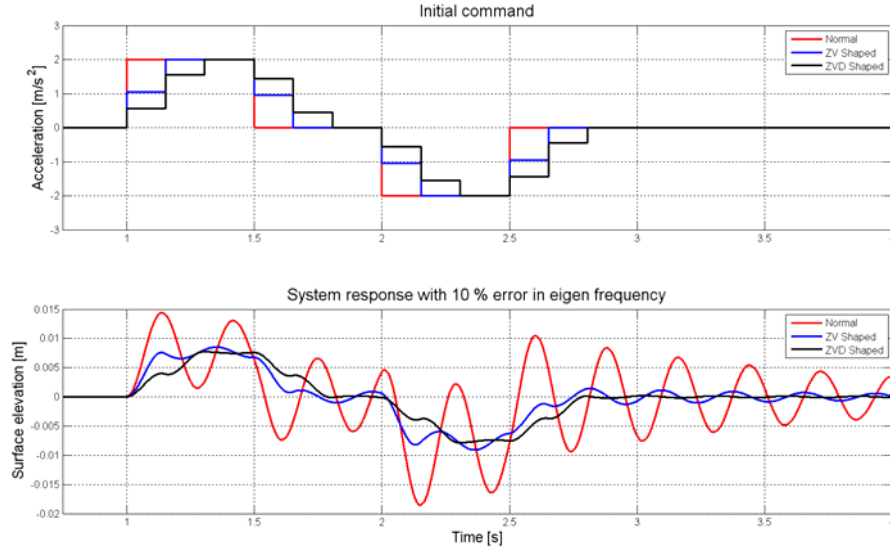


Figure 10 Comparison of ZV shaper and ZVD shaper at a 10% error in the system's frequency.

This figure clearly shows that the ZVD shaper is more robust than the ZV shaper, at least with this example with a modelling error in the natural frequency. Those two types of input shapers show the basic idea serving as a foundation for this method. Next to those two shapers, there is a range of other variations. The next one briefly shown is the EI input shaper.

4.3 EI INPUT SHAPER

The so-called EI shaper (extra insensitive) being defined in [7], [9] and [10] is a self-evident version of the two above described input shapers. This version is based on the assumptions that the natural frequency cannot be exactly measured or that it changes during the operating process. With the ZV shaper as well as with the ZVD shaper, the input shaper design is directly laid out on the system's natural frequency. With the EI shaper, nearby frequencies (ω_{low} and ω_{high}) are used for designing it and the residual oscillation is limited.

$$\begin{aligned} \sum_i^n A_i \cdot e^{-j \cdot D \cdot \omega_0 \cdot t_i} &= \text{limited} \\ \sum_i^n A_i \cdot e^{-j \cdot D \cdot \omega_{low} \cdot t_i} &= 0 \\ \sum_i^n A_i \cdot e^{-j \cdot D \cdot \omega_{high} \cdot t_i} &= 0 \end{aligned} \quad (22)$$

The EI input shaper can also be interpreted from a convolution of two ZV shapers, whereas the second impulse is different due to ω_{low} and ω_{high} . The following figure shows this relation.

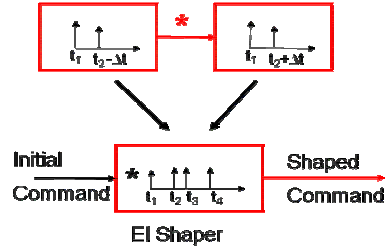


Figure 11 Principle generation of the EI shaper.

If those three types of input shapers are compared to each other with regard to robustness, surely the EI shaper shows the best behaviour in this regard, provided that the system frequency really changes and that a (known!) residual oscillation can be tolerated. The duration time of the ZVD and the EI Shaper are nearly the same.

The figure below shows a direct comparison in form of the input shaper sensitivity curves.

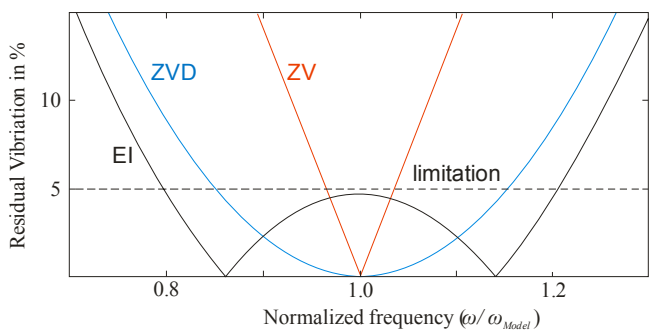


Figure 12 Comparison of ZV-, ZVD- and EI shaper with regard to change in natural frequency.

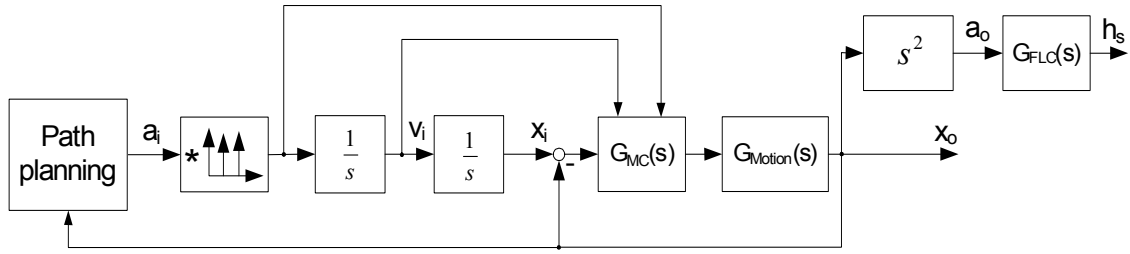


Figure 13 Integration of an input shaper at a drive control.

4.4 INTEGRATION AND IMPLEMENTATION OF INPUT SHAPER

As the previous sections show, all input shapers may be regarded as a kind of pre-filter in respect of the reference variable of the acceleration.

Modern industrial servo amplifiers offer the possibility to modify speed and acceleration during positioning. Figure 13 shows the integration of an input shaper at a common drive control. Often, path planning and other calculations are made by means of a PLC, which afterwards sends new values of position, velocity and acceleration to the servo amplifier or motion control system. The meanings of the blocks for the transfer functions in figure 13 are:

$GMC(s)$: servo amplifier or motion control

$GMotion(s)$: mechanical plant (gear, tooth belt)

$GFLC(s)$: liquid in the container (5)

In the calculations above the transfer functions $GMC(s)$ and $GMotion(s)$ were to be handled as ideal with “1”!

Implementing an input shaper on a PLC should not cause major difficulties since implementation is very similar to a digital filter (for example FIR filter).

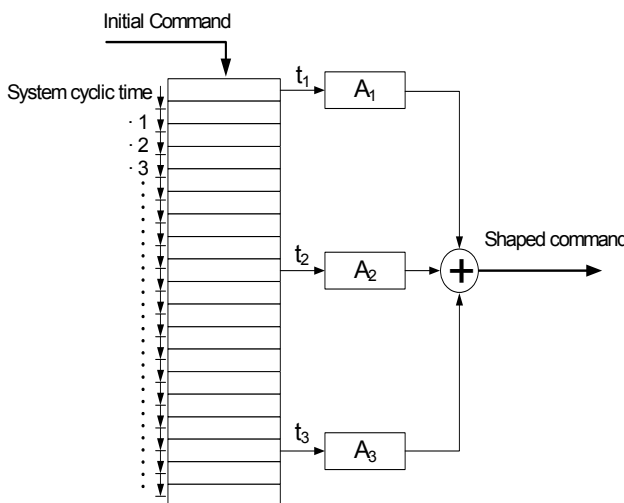


Figure 14 Implementation principle of a ZVD input shaper.

With some memory capacity, which depends on the filter running time (and thus also depends on the natural frequency of the system to be eliminated), some kind of shift-register can be established. With every loop of the

system, the deterministic PLC shifts the present original set point by one position backwards. The system loop can be adjusted to a multiple of the bus system time (here: $400 \mu s$). With the PLC used in the present case, the system loop is at least $1.2 ms$. This minimum temporal resolution should be sufficient here. Any Jitter error caused by the bus-cycle and system-cycle can be disregarded in this process. Reasons are that the internal clock depends on the bus clock of this system and also on the Ethernet POWERLINK connection used for this case and that internal clock and bus clock are synchronised. Depending on the chosen input shaper, the temporal positions of the multipliers can then be defined for the related amplitude value.

With this method of implementation, nearly any signal can be used as an input variable. This filtered signal is transferred to the servo amplifier as a new input variable, respectively as a preset acceleration profile. As also described in [8], this method can be referred to as a so-called online operation. The source of the actual reference input variable is left open though. The source could be, for example, an operator or a virtual axis with electronic cam disk function. Thus, such an implementation does not imply any restrictions.

5 CONCLUSION

The aim of the paper is the presentation of a method for a slosh-free movement of open containers filled with liquids (here: water). In the first part of the paper, modeling and parameter identification of the liquid behavior in the container are included and the experimental results are also verified. Afterwards, the concept of input shaping is shown. The three different basic shapers ZV, ZVD and EI are introduced and compared to each other. It is shown that the ZV shapers have the smallest duration time but also the most sensitivity against modeling errors. The ZVD and EI shaper are more robust regarding this issue but the duration time is about twice as long in respect of the periodic time of the system.

In the end it is shown how to integrate such kind of pre-filters into an available drive control. Also a basic approach is shown of how to realize and implement an input shaper into software.

REFERENCES

- [1] Siekmann, Thamsen; Strömungslehre, 2nd edition, Springer 2008.
- [2] Oertel Herbert jr., Strömungsmechanik, Vieweg, 2004.
- [3] Ken'ichi Yano, Kazuhiko Terashima 2001, Robust Liquid Container Transfer Control for Complete Sloshing Suppression, Control Systems Technology, IEEE Transactions on Volume 9, Issue 3, pp. 483 – 493, May 2001.
- [4] Feddema, J. T., C. R. Dohrmann, G. G. Parker, R. D. Robinett, V. J. Romero, and D. J. Schmitt D1997E: "Control for sloshfree motion of an open container." IEEE Control Systems, 17:1, pp. 29–36.
- [5] Mattias Grundelius; Methods for Control of Liquid Slosh, Department of Automatic Control Lund Institute of Technology, 2001.
- [6] H. Lutz, W. Wendt, Taschenbuch der Regelungstechnik, 2. Auflage, Verlag Harri Deutsch, 1998.
- [7] William Singhose, Warren Seering, Command Generation for Dynamic Systems, August 19, 2006
- [8] Hubinský, P., Vranka, B., Jurišica, L., Genetic algorithm based method of elimination of residual oscillation in mechatronic systems, Kybernetika Journal, 2005.
- [9] Tarunraj Singh, Dept. of Mech. & Aero. Eng., University of Buffalo, William Singhose Dept. of Mech. Eng., Georgia Institute of Technology, Tutorial on Input Shaping/Time Delay Control of Maneuvering Flexible Structures.
- [10] Singhose W.; Comand Generation for flexible systems; PhD-Thesis; S.B.M.E., Massachusetts Institute of technology, 1990 M.S.M.E., Stanford University, 1992.

IMPROVING THE DYNAMIC PERFORMANCE OF REDUNDANT ELECTROHYDRAULIC SERVOACTUATORS

G. Jacazio L. Gastaldi

Politecnico di Torino

ABSTRACT

To counteract the variations of servovalve offsets in redundant electrohydraulic servosystems different solutions have been taken, but limited use has been done of techniques based on the injection of compensation signals into the servovalves such to reduce the difference between the pressure differentials across the control lines of the two servoactuators. A research activity has thus been performed in which different equalization techniques have been examined and their relative merits have been assessed. An optimal equalization control strategy has then been devised, capable of minimizing the force fighting between two redundant servoactuators and the appropriate authority limit to the equalization signals has been determined such to prevent unacceptable uncommanded movements in case of failure of a component of the equalization loop.

Keywords: aerospace engineering, redundant servoactuators, equalisation techniques, flight control system, fly-by-wire

1 ELECTROHYDRAULIC SERVOACTUATORS AND FLY-BY-WIRE SYSTEMS

As it is well known, fly-by-wire flight control systems use electrical signalling to relay the pilot commands from the cockpit controls to flight control computers (FCCs) that issue the commands to the flight control actuators and accept from them the electrical feedback signals. In order to ensure the necessary redundancy, two actuators are normally used in primary flight controls to drive the same aerodynamic control surface, with each actuator interfacing with one or more FCCs. In some particular applications three actuators were connected to the same flight control surface, though this configuration has been used only when deemed absolutely necessary since it increases the system complexity. The present paper will thus deal with the typical case of two hydraulic actuators driving an aerodynamic control surface.

Contact author: Giovanni Jacazio¹, Laura Gastaldi²

¹ Department of Mechanics - Politecnico di Torino
Corso Duca degli Abruzzi, 24 10129 Torino
E-mail: giovanni.jacazio@polito.it

² Department of Mechanics - Politecnico di Torino
Corso Duca degli Abruzzi, 24 10129 Torino
E-mail: laura.gastaldi@polito.it

When two hydraulic actuators are connected to the same aerodynamic control surface, a very important design issue is to guarantee that no conflict originates between the two actuators such to impair the flight control system performance.

This is particularly critical when the servoactuators hold the flight control surface at a certain fixed position under rapidly varying loads, such as those occurring when the flying aircraft is subjected to gusts or turbulence.

Over the years different design solutions have been worked out for redundant electrohydraulic servoactuators and have been implemented into operational aircraft. The main critical issues to be addressed have been: input signal mismatch, control valve offset, difference between supply pressures of the two hydraulic systems interfacing with the actuators, system robustness following failures and, of course, overall system complexity. Though generalization is often a risky business, still it is possible to state that the different configurations of redundant electrohydraulic servoactuators for flight control systems can be grouped in the following four categories.

Active/standby systems. In these systems one of the two actuators connected to the same flight control surface is active while the second one is in standby. In case the operating actuator fails, the other one is activated and ensures an unabated operation.

Single flow control valve. In these systems the flows to the two hydraulic actuators are simultaneously controlled by two sections of a single control valve.

Reduction to the sensitivity to the control valve offsets.

In these systems appropriate actions are taken to reduce the offsets of the control valve and hence the associated mismatch between the actuator forces.

Equalization between the two electrohydraulic servoactuators. In these systems sensors are introduced to measure the differences between the two servoactuators parameters and appropriate control laws are defined to correct those differences.

These four types of architectures will be discussed in the following and the results of a research activity aimed at defining an optimal and robust equalization technique will be presented.

2 LOAD DISTRIBUTION BETWEEN PARALLEL SERVOACTUATORS

When two electrohydraulic servoactuators are connected to the same flight control surface, the forces developed by the two actuators are summed and the problem of ensuring an even load sharing between the two actuators arises. The force developed by an actuator is a function of the pressures acting on the two sides of the actuator piston, and when the actuator is stationary, the pressure differential across the two control valve ports, and thus across the two actuator sides, changes very rapidly with the change of the input signal of the control valve. The valves used to control the pressurized fluid flow to flight control actuators typically consist of closed-center spool valves with very high pressure gains around null so that a large pressure differential, and therefore a large actuator force, is created as a result of small spool displacements. In general, close-center spool valves have a pressure gain that brings about the full pressure differential for a spool displacement equal to 3-5% of maximum. In spool type control valves the spool displacement is generally proportional to the input signal, therefore 3 to 5 % of maximum input signal to the control valve is sufficient to generate the full pressure differential in a no-flow condition.

The flow control valves commonly used in electrohydraulic servoactuators for flight control systems are two-stage electrohydraulic servovalves (EHSVs) which use an internal hydraulic amplifier to convert the electrical input signal into valve spool displacement. Servovalves offer several advantages: they have a limited cost, weight little, require a very small electrical input power (in the 0.1 W range), and they have a large chip shear capability: if the valve spool is stuck in one position due to a debris, the pressure differential between the two sides of the control valve spool created by the internal hydraulic amplifier generates a large force on the spool to break it loose. A problem associated with servovalves is their offset, that can greatly differ from one servovalve to another and that can change with life and with the operating conditions. The

servovalve offset is typically considered as the sum of two contributions: the null bias and the null shift. The null bias is the difference between electrical null (zero input current) and hydraulic null (zero pressure differential) under standard operating conditions: supply and return pressures at their rated values, standard ambient temperature, valve mounted on a stationary structure. The typical value of null bias is 3 to 4% of the rated input current and may increase a little at the end of the operating life. The null shift is a temporary variation of null bias with changing operating and environmental conditions and may be as high as 10% of the rated input current. Worst of all the null shift is not a deterministic effect; two nominally equal servovalves may exhibit different null shifts, and also in the opposite directions, with the same change of operating and environmental conditions. It thus turns out that under an adverse combination of null bias and shift, the resulting total servovalve offset can reach 15% of the rated input current.

This particular behaviour of the servovalves has always been a critical issue and high performance light-weight proportional valves, known as direct drive valves (DDVs) within the aerospace community, have also been applied as flow control devices for electrohydraulic servoactuators. DDVs use the force developed by a proportional solenoid to drive the valve spool and do not rely on an internal hydraulic amplifier. This configuration leads to several advantages: reduced offset, lower internal leakage, lower probability of a hardover failure, but it has critical drawbacks. First of all, a much greater electrical input power is required (in the 3 - 5 W range), then, greater weight, reduced chip shear capability and high cost. Moreover, DDVs require an internal spool position feedback loop and often also a spool velocity loop nested within the spool position loop to ensure a high dynamic response with adequate stability. Although DDVs have been used in recent applications, EHSVs are still the preferred choice as flow control valves in electrohydraulic flight control systems, especially considering their low electrical power consumption. The 3-5 W power required by DDVs is apparently little, but when one considers the electrical drivers of several DDVs all tightly packed within a flight control computer, that power consumption and the associated thermal dissipation may become a concern for the electronic designers.

Let us now consider two electrohydraulic servoactuators driving a flight control surface as shown in the concept block diagram of Figure 1. Each servoactuator consists of a linear hydraulic actuator, a flow control valve, a solenoid valve, a shutoff/bypass valve and a control electronics; a position transducer inside the hydraulic actuator provides the feedback signal to the control electronics to close the position control loop. The actuator control electronics receives the position command for the flight control surface from the section of the flight control computer that processes the signals from the cockpit controls and from the aircraft sensors and generates the control signal to the

control valve according to a proper control law, thereby modulating the flow/pressures to the hydraulic actuator as required to respond to the pilot inputs and to the variable loads on the aerodynamic surface. The actuator control electronics also generates an on/off electrical signal (arming signal) to a solenoid valve; when the solenoid valve is energized, a high pressure pilot signal is ported to a shutoff / bypass valve which causes this valve spool to move into a position such to connect the ports of the control valve to the two sides of the hydraulic actuator, thus enabling the actuation system operation. If the arming signal is off and the solenoid valve is deenergized, or if no pressure is available due to a hydraulic system failure, the pilot signal is at low pressure and the shutoff / bypass valve is switched into a position such to close the connection between the ports of the control valve and the hydraulic actuator, and to simultaneously interconnect the two sides of the actuator in order to allow a flow recirculation as a consequence of the movements imposed to the actuator from the other active actuator connected to the same flight control surface. Very often, the fluid recirculating between the two sides of the actuator passes through a restrictor providing a pressure drop which is a function of the flow rate and thus of the actuator speed. This feature is instrumental in creating a certain amount of damping to the flight control surface in case of loss of operation of both hydraulic actuators; in such a case, the flight control surface operation is lost, but the same surface automatically positions itself in the aerodynamic wake and the amount of movements around that average position is limited by the actuators damping.

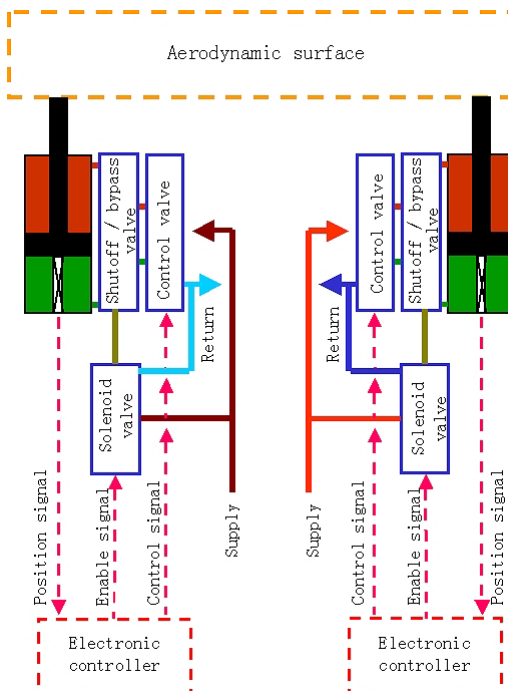


Figure 1 Concept schematic of a dual redundant electrohydraulic servoactuator.

Each of the two identical electrohydraulic servoactuators is hooked to a different aircraft hydraulic system and it is often controlled by two different control lanes, thereby leading to a dual hydraulic/quadruplex electrical architecture. With this architecture, each of the electrical components of the servoactuator (solenoid valve, control valve, position transducer) is dual electrical and accepts/transmits two electrical signals; moreover, the four position signals provided by the position transducers of the two servoactuators (two electrical signal per transducer) are exchanged among the four flight control computers (FCCs) via optoisolated links. Each FCC has thus available all position transducers signals, performs a signal consolidation according to a common logic, and perfectly identical control signals are thus issued by the FCCs to the electrical lanes of the two control valves.

We now consider the case of the two control valves actually consisting of two equal EHSVs. When a servovalve receives a control signal to move off null, a pressure differential is created between the control ports that is proportional to the magnitude of the control signal and on the servovalve pressure gain; this pressure differential is acting upon the actuator that develops a load force.

For an ideal servovalve with zero offset the control signal versus the load force is as shown in Figure 2a. If a servovalve offset is present, the curve of the actuator load force is shifted of an amount equal to the offset as shown in Figure 2b.

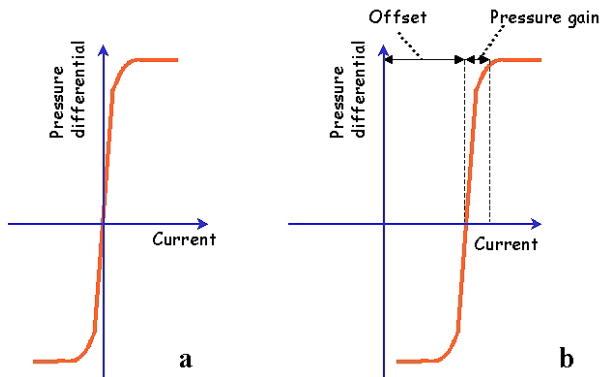


Figure 2 Servovalve control signal vs. actuator load force for a servovalve without offset (a) and with offset (b).

If only one servoactuator were driving the flight control surface, or if the two EHSVs of the two servoactuators had exactly the same offset, the presence of an offset would non originate any problem to the system operation.

As it is shown in Figure 3a, if a certain load force F_1 must be developed by sum of the two actuators controlled by two EHSVs with equal offsets, a current control signal i_1 must be created by each of the control electronics, such to create a pressure differential across the two sides of each actuator to develop a total force equal to F_1 . The control signal i_1 is equal to:

$$i_1 = i_0 + \frac{F_1}{2AG_p} \quad (1)$$

where:

- i_0 = servoactuator offset
- F_1 = load force on the flight control surface (total of the two actuators)
- A = active area of each actuator (assuming balanced area actuators)
- G_p = servoactuator pressure gain

For the simple case of a servoactuator controlled with a proportional control law, the position error is equal to the control signal divided by the proportional gain, and since this gain can normally be set sufficiently large while still maintaining the system stability, the resulting position error is low and generally acceptable. Should it be required to further reduce this error, that can be achieved by adding an integrator with a suitable gain in the control law.

If the two servoactuators driving the same flight control surface are controlled by two servo valves with offsets in opposite directions, a total load force is obtained as shown in the diagram of Figure 3b. The total load force diagram shows a region of zero force gradient in which the overall system does not respond to the control signals issued by the electronic controllers. This behaviour is totally unacceptable in flight control systems because of the resolution, frequency response and dynamic stiffness requirements.

The accuracy requirement for a servoactuator of a primary flight control system is in general not particularly stringent since the flight control servoactuator is actually a subsystem of the aircraft attitude control system that makes up the outer reference loop, and 1-2 % error is normally a requirement. In other words, the overall objective is to accurately control the roll, pitch and yaw angles of the aircraft, and the accuracy errors of the flight control servoactuators are divided by the gains of the outer reference loops. On the other hand, a very tight requirement is the resolution of the servoactuator, which is defined as the capability to respond to the command changes. The resolution requirements depend upon the aircraft category, but are most often in the range from 0.006° to 0.025° of angular deflection of the flight control surface. For the case of 60° maximum that corresponds to a servoactuator resolution between 0.01% and 0.04% of full actuator travel. Consider now the unlucky case of a dead band (Figure 3b) equal to 20% of maximum servoactuator control signal; the electronic controller gain is typically set such that the maximum servoactuator control signal is obtained for a position error equal to 4-5% of the full actuator travel, and this stems from the need to provide a suitable frequency response while maintaining an adequate stability margin. As a result, a 20% dead band for the control signal is reflected into a dead band of 0.8% to 1% of full actuator travel, which is about two orders of magnitude greater than the specified resolution.

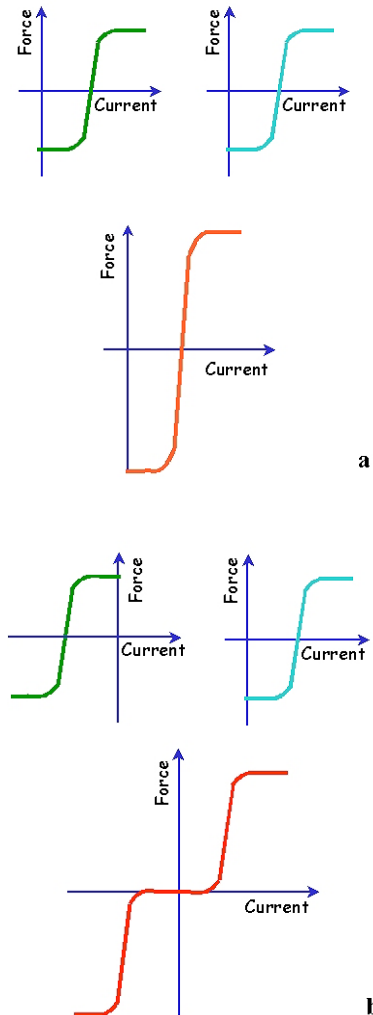


Figure 3 Total load force provided by two servoactuators connected to the same flight control surface for the cases of servoactuators controlled by servo valves with identical offsets (a), and of servoactuators controlled by servo valves with opposite offsets (b).

The dead band around the null condition also negatively affects the system frequency response to small amplitude commands introducing excessive phase lag and gain attenuation.

A second critical condition created by the dead band of the actuators load force is that the system stiffness is practically reduced to zero in that area. As a consequence, when the aircraft flight control surface is subjected to fluctuating loads originated by the atmospheric turbulence, large oscillations of the flight control surface are originated which on their turn give rise to a bumpy aircraft flight.

It is therefore clear that a flight control actuation system architecture in which two servo valve controlled electrohydraulic servoactuators driving the same flight control surface are both active is not acceptable for aircraft primary flight control systems.

3 TECHNIQUES USED FOR A BETTER LOAD SHARING OF PARALLEL SERVOACTUATORS

A solution often used to avoid the dead band in the signal versus load force diagram is to always operate one servoactuator at the time: one of the two servoactuators is operating while the second one is in a bypass mode (active / standby architecture). This solution is simple and eliminates the root cause of the dead band and has for instance been used by Airbus the fly-by-wire primary flight control actuators of their aircraft. Two main drawbacks are however associated with this architecture. First, the actuators must be overdesigned since under normal operating conditions the active actuator must be capable of driving the maximum aerodynamic load plus the load created by the standby actuator. Second, in case of a failure of the hydraulic system providing the pressure supply to the active actuator, a time delay occurs between the onset of hydraulic system failure and the instant in which the standby servoactuator is activated and takes up the control of the aerodynamic surface. This delay depends on the time necessary to positively recognize the failure, on the energization time of the solenoid valve and on the commutation time of the shutoff / bypass valve. During this time delay there is a temporary loss of control of the aerodynamic surface, which does not lead to a flight critical condition since it lasts relatively little (0.1 to 0.2 s), but can anyhow create an unpleasant sudden disturbance during the aircraft flight.

Another approach to minimize the effect of the servovalve offsets and improving the load sharing between two actuators driving a common flight control surface is that to reduce the sensitivity to the offsets by softening the pressure gain characteristics of the servovalves. As it can be seen in the diagram of Figure 4, two gain servovalves with large opposite offsets and low pressure gains do not originate a dead band in the combined load force diagram of the two actuators.

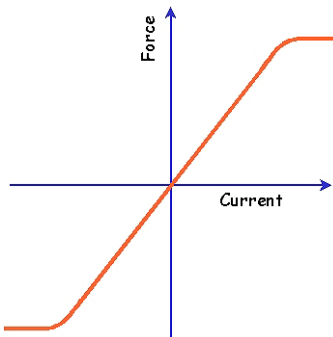


Figure 4 Total load force provided by two servoactuators connected to the same flight control surface for the case of servoactuators controlled by low pressure gain servovalves.

A reduction of the pressure gain can be obtained by overcutting the spool lands in order to achieve an open-center valve configuration. This solution is effective in eliminating the dead band of the load force diagram, but it

brings about two main disadvantages: an average low stiffness due to the low pressure gain and large internal leakages due to the open-center configuration. For these reasons, this solution had very limited applications.

A different way for obtaining an even load sharing between two hydraulic actuators driving a common aerodynamic surface consists of controlling the pressurized fluid flows to the two hydraulic actuators with a single control valve consisting of long spool sliding inside a sleeve interfacing with the two hydraulic systems and the two actuators. The valve actually consists of two sections: section I controls the flow between hydraulic system I and actuator I, while section II does the same for hydraulic system II and actuator II. A very careful and accurate machining of the spool lands allows an excellent matching between the two sections, so that equal pressure differentials are created for the two actuators as a result of a spool displacement away from null, providing that the supply pressures of the two hydraulic systems are equal. With this solution, the movement of the spool is obtained by applying appropriately controlled pressures at its two ends. Each opposite end of the spool carries an integral piston sliding inside a cylinder whose two chambers are connected to the control ports of a servovalve, as it is shown in the concept block diagram of Figure 5.

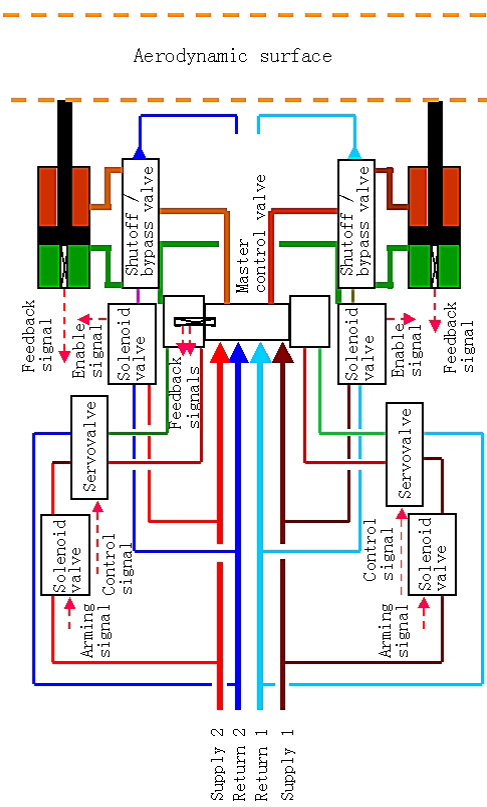


Figure 5 Concept block diagram of a system comprised of two electrohydraulic servoactuators controlled by a common dual section flow control valve.

The position of the main control valve spool is measured by a position transducer that provides a feedback signal used to close a main control valve position loop. The two servoactuators are of a little size since they only have to control the flows resulting from the displacement of the main control valve spool, and present low pressure gains. High gains are not necessary here because the main control valve position feedback loop does not need to be particularly stiff. As it has been shown in the diagram of Figure 4, the use of servoactuators with low pressure gains minimizes the negative effects of adverse combinations of servoactuator offsets; at the same time, there is no reduction of the servoactuator stiffness since the low pressure gain only affects the stiffness of the internal position loop of the main control valve and not that of the servoactuator loop, which is ensured by the high pressure gain of the main control valve. Although this architecture is more complex, it has been widely used in fly-by-wire primary flight control systems due to its undisputable performance advantages. The primary flight control systems of the Tornado and of the F-18 are examples of application of this architecture.

The same design concept of using a single valve for modulating the flows to two hydraulic actuators can be pursued by using a direct drive valve whose spool is driven by multiple force motors. The spool position is measured by a transducer that provides the signal necessary to close the spool position feedback loop. High performance DDVs tend to be marginally stable and their stability is often improved by providing them with the capability of measuring the spool velocity and increase their internal damping by creating a spool velocity feedback loop internal to the spool position loop. Primary flight control actuation systems based on this architecture have been used in the primary flight control systems of some military aircraft such as the Eurofighter. As it has been pointed out at the beginning of paragraph 2, a DDV based architecture as the merits of an overall greater reliability and of lower internal leakages, but the much greater electrical power draw and cost may thwart their use in several applications. Moreover, the lower axial force developed on the spool by the force motors when compared to that developed by hydraulic pressure raises concerns about their ability of shearing off large debris that could remain stuck between spool and sleeve and create a spool lock.

A fourth way to improve the load sharing between two electrohydraulic servoactuators while simply using two servoactuators, with each valve controlling the flow to its own actuator, is to sense the pressure differentials across the two actuators, compare the two pressure differentials and inject compensation signals into the servoactuator currents such to equalize the actuators pressure differentials (Figure 6).

This technique is simple in principle, but its implementation is not an easy task since a careful tradeoff must be performed between the need of equalizing the actuators pressure differentials and that to avoid excessive

transient uncommanded movements in case of a failure and of the subsequent shutoff after the failure has been recognized.

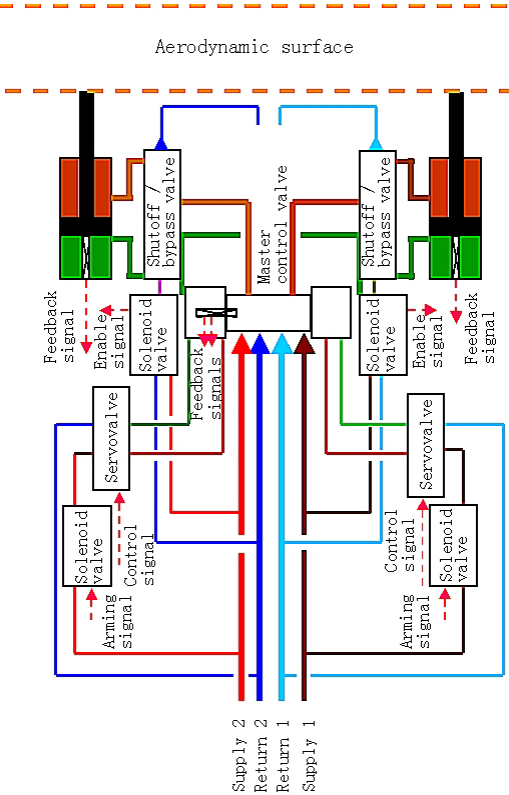


Figure 6 Concept block diagram of two electrohydraulic servoactuators with individual servoactuators (EHSVs) and differential pressure equalization.

The main areas requiring a careful scrutiny are: definition of the best strategy to change from the system null that existed prior to the failure to the system null after the failure, performance with different supply pressures of the two hydraulic systems, dynamic response and stability of the equalization loop, errors of the pressure measuring devices, maximum authority granted to the equalization loop, failure detection of the differential pressure sensors and corrective actions. Concerns about these design issues have been the main reason for a very limited application of this type of architecture to fly-by-wire flight control systems. A partial application of this architecture is found in the primary flight controls of the B2. The primary flight control servoactuators of this aircraft actually have their flows controlled by separate DDVs and differential pressure sensors are used by each servoactuator to provide a dynamic pressure feedback for improved dynamic performance. In addition, the signals of the two differential pressure sensors are compared to each other to create compensation signals to the two DDVs to reach a better load sharing between the actuators. DDVs, however, exhibit a much lower offset than EHSVs, therefore, the equalization issue is much less critical than with EHSVs.

4 OPTIMISATION OF THE CONTROL STRATEGY FOR EQUALIZING PARALLEL SERVOACTUATORS CONTROLLED BY ELECTROHYDRAULIC SERVOVALVES

As emphasized before, the purpose of the research activity presented in this paper was to define an optimized solution for achieving an even load sharing between two hydraulic actuators separately controlled by individual electrohydraulic servovalves. The merits of the solution that was eventually developed are: simple system architecture, lower cost, limited transient disturbance following a failure, possibility of operation following a seizure of a valve spool. Though the probability of a seizure of valve spool is considered very low, still the system architectures based on a single flow control valve for the two actuators (schematic of Figure 5) present multiple redundant control lanes with a common link made up by the single main control valve; a failure of this valve leads to the loss of operation of the relevant flight control surface. Controlling the actuator flows with two different control valves offers a greater survivability to the flight control system. The concept schematic for the system under study is therefore the one shown in Figure 6.

In order to define the general architecture of a control law aimed at equalizing the forces developed by two actuators controlled by electrohydraulic servovalves it is convenient to refer to a linear model of the system; the actual values of the control parameters will then be fine tuned with the use of a detailed non-linear model, that will also be used for evaluating the system performance under normal operating, degraded and failure conditions. The block diagram of the linearized mathematical model of the system is illustrated in Figure 7. The input command x_C is compared to the position feedback z to generate the position error e which is processed by a control law with a transfer function $G_1(s)$ to provide the control signals to the two servoactuators. The control signals (equal for both servoactuators) are modified by the equalization signal h , which is subtracted to the control signal of servoactuator 1 and added to the control signal of servoactuator 2; the modified control signals are then fed to digital-to-analogue converters to generate the input signals to the servoamplifiers with a gain G_A generating the controlled currents i_1 and i_2 to the servovalves. The offsets of the two servovalves are represented in the block diagram by disturbance currents i_{d1} and i_{d2} , which are added to the actual currents i_1 and i_2 . Therefore, the two servovalves will behave in response to equivalent currents $i_{V1} = i_1 + i_{d1}$ and $i_{V2} = i_2 + i_{d2}$. The remaining portion of the forward path of the control loop is the usual block diagram of a hydraulic servoactuator; $G_V(s)$ is the transfer function defining the servovalve dynamics, G_Q and G_P the servovalves flow and pressure gains, C the hydraulic capacitance of each actuator chamber with the

actuator assumed at mid position, k_L the internal leakage coefficient, A the actuator area, k the stiffness of the actuator attachment point to the underlying structure, c_V the external damping coefficient, m the total mass of the moving parts reflected to the actuators linear output. In the same block diagram δp_1 and δp_2 are the pressure differentials across the two sides of actuators 1 and 2, F_1 and F_2 the corresponding actuator forces, R the load force, y the actuators linear displacement.

The transfer function $H(s)$ of the feedback path is that of the demodulator filtering the electrical signal provided by the actuators position transducer. Fly-by-wire flight control systems typically use LVDT type position transducers because of their robustness and capability of operating in harsh environments; these transducers are supplied with a high frequency ac input voltage and require low-pass second-order filters to cancel out the alternating component of the output signal.

The two pressure differentials δp_1 and δp_2 are measured by differential pressure transducers also consisting of LVDTs measuring the displacement of a spring centered cylinder subjected to the pressure differential. The output signal of each of these transducers is therefore demodulated by a filter with a transfer function $H_p(s)$. The difference between the two pressure differential signals is then fed to the equalization control law that is indicated in the block diagram of Figure 7 with the transfer function $H_e(s)$, which is actually a complex function as it is shown in the diagram of Figure 8.

The difference $\delta p_{1-2} = \delta p_1 - \delta p_2$ between the two pressure differential signals first passes through an activation block that is commanded by the enable/disable control logic.

In order for the equalization function to be activated, both servoactuators must operate correctly and be pressurized, which condition is signalled by the pressure switches of the two servoactuators.

If both pressure switches signals are "on", an enable signal is sent to the activation block that transfers the δp_{1-2} signal to the following blocks; on the contrary, the output of the activation block is equal to zero. The δp_{1-2} signal is processed by a modified PI controller in which the gain K_{IC} of the integral part of the controller is varied with time when the equalization logic is activated, starting from an initial large value at switch-on to a smaller one after the initial equalization transient has settled. The integrator output signal is saturated to maximum / minimum values; the saturation limits are enabled if both pressure switches signals are "on"; on the contrary they are set to zero. The output signals h_I and h_P from the integral and proportional controllers are summed up, the resulting equalization signal h is saturated to a maximum/minimum limit and injected with the appropriate sign into the summing points of the forward paths of the two servoactuators control loops.

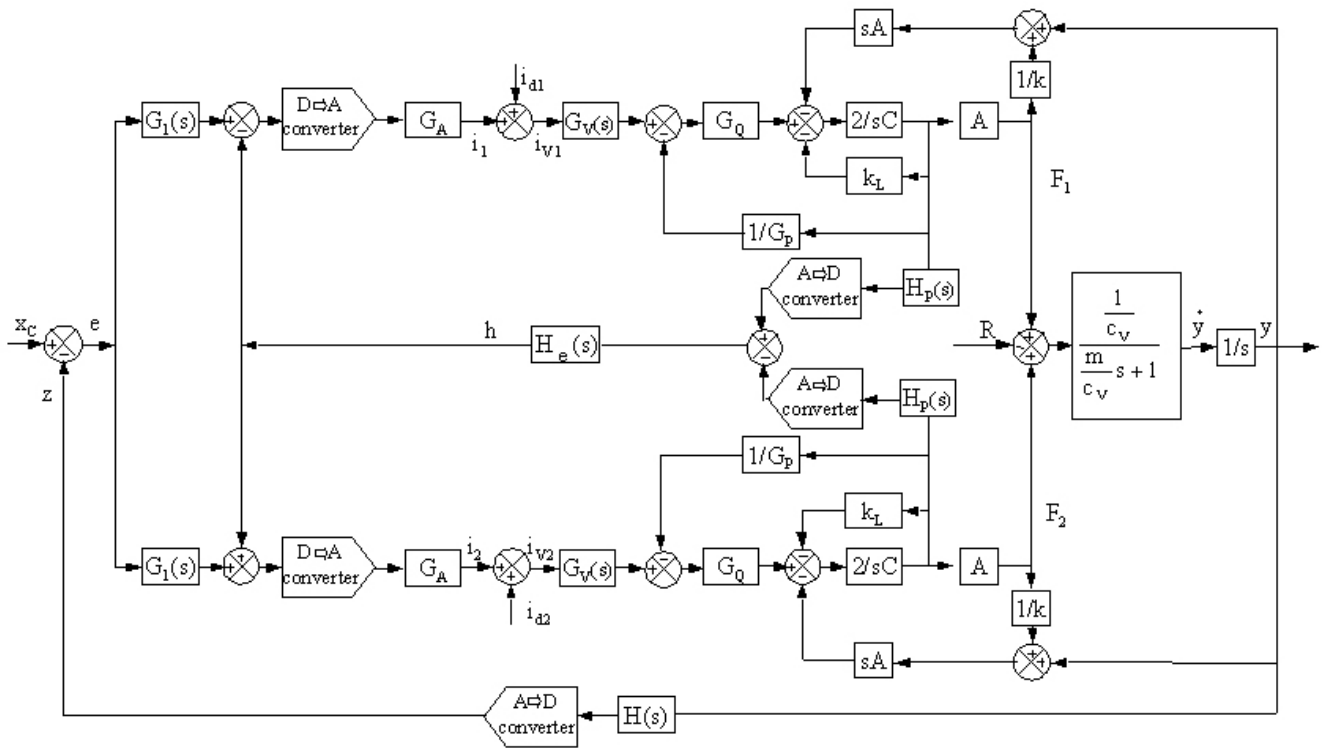


Figure 7 System block diagram.

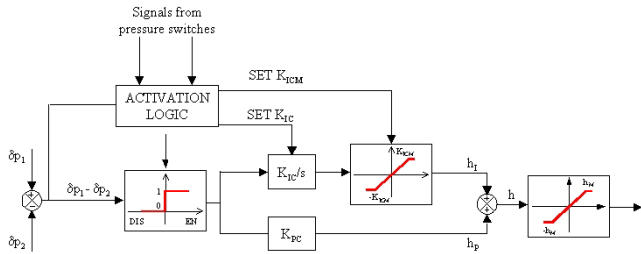


Figure 8 Block diagram of the equalization control law.

In order to better understand the rationale behind the selection of the equalization control law outlined above, it is convenient to consider a simplified case of a system in which the control transfer function $G_1(s)$ is a pure gain K_1 , the equalization transfer function $H_e(s)$ consists only of a proportional gain K_{PC} , and the system is in a stationary condition. For these simplified conditions, the two pressure differentials δp_1 and δp_2 are given by the following expressions, where e is the servoactuators position error and $K'_L = G_Q/G_P$ is the ratio between servovalve flow and pressure gains..

$$\delta p_1 = \frac{K_1 G_Q G_A}{k_L + K'_L} e + \frac{G_Q \left(\frac{k_L + K'_L}{G_A G_Q K_{PC}} + 1 \right) i_{d1} + G_Q i_{d2}}{\left(k_L + K'_L \right) \left(\frac{k_L + K'_L}{G_A G_Q K_{PC}} + 2 \right)} \quad (2)$$

$$\delta p_2 = \frac{K_1 G_Q G_A}{k_L + K'_L} e + \frac{G_Q i_{d1} + G_Q \left(\frac{k_L + K'_L}{G_A G_Q K_{PC}} + 1 \right) i_{d2}}{\left(k_L + K'_L \right) \left(\frac{k_L + K'_L}{G_A G_Q K_{PC}} + 2 \right)} \quad (3)$$

For the worst case of two servovalves with opposite offsets, $i_{d1} = -i_{d2} = i_{d0}$, equations (2) and (3) become:

$$\delta p_1 = \frac{K_1 G_Q G_A}{k_L + K'_L} e + \frac{i_{d0}}{1/G_Q \cdot (k_L + K'_L) + 2G_A K_{PC}} \quad (4)$$

$$\delta p_2 = \frac{K_1 G_Q G_A}{k_L + K'_L} e - \frac{i_{d0}}{1/G_Q \cdot (k_L + K'_L) + 2G_A K_{PC}} \quad (5)$$

The flow gain G_Q is a parameter that is selected as a function of the actuation speed to be developed by the actuator, therefore, should no equalization be present ($K_{PC} = 0$), the only possible way for reducing the difference between δp_1 and δp_2 is to increase the internal leakage (greater k_L) or reduce the pressure gain G_P . However, both these ways lead to a reduction of the value of the coefficient multiplying the servoloop error e , which implies a reduction of the servoactuator stiffness, since a greater error is necessary to obtain the same pressure differential. Introducing the pressure equalization ($K_{PC} > 0$) brings about a reduction of the effect of the offset current i_{d0} on

the pressure differentials. The difference between δp_1 and δp_2 thus decreases with increasing the value of K_{PC} , but this process cannot continue above a certain limit for it would lead to an instability of the pressure equalization loop. However, it must be considered that the servoactuator offsets are the result of different contributions, as it was outlined at the beginning of this paper. Some contributions (null bias and null shift with temperature) are steady-state or quasi-steady-state factors and their effect can thus be recovered by introducing a low gain integrator (K_{IC} in the block diagram of Figure 8), that eventually develops a signal such to compensate these contributions to the servoactuator offsets. Since the maximum null bias is about 4% of the rated servoactuator current, and the maximum null shift with temperature can take another 4% of rated servoactuator current, the saturation limit K_{ICM} of the block diagram of Figure 8 can be set such to correspond to 8% of the rated servoactuator current. However, in case the signal of one of the two pressure switches is "off", the saturation limit K_{ICM} is set to zero to fully disable the equalization logic. At the same time, the saturation limit h_M of the entire equalization control law can be set to 15% of the rated servoactuator current, which is the maximum possible offset under normal servoactuator operation.

The rationale for this control law is to use the integral control for compensating the steady-state offsets, while using the proportional control only for compensating the rapid variation of servoactuator offsets, such as those originated by variations of the return pressure due to the pressure drops originated by the flow through the return lines. Since the proportional control has to compensate only a fraction of the servoactuator offset, it can be kept lower than it would be required for entire offset compensation, and the equalization loop stability can be maintained while minimizing the residual difference between the two pressure differentials.

The gain K_{IC} of the integrator must be kept low to prevent an adverse effect on the stability of the equalization loop, but this may be a negative factor at the start-up when the equalization logic is activated, since it would lead to a long settling time. The value of the integrator gain is thus initially set high and equal to 10 times its normal value and is reduced to its normal value as the difference $\delta p_1 - \delta p_2$ is reduced to a value equal to 20% of the supply pressure. From then on, the integrator gain remains constant at that value, no matter of the variations of $\delta p_1 - \delta p_2$. This technique allows an acceleration of the initial settling time without affecting the equalization loop stability.

5 CHARACTERISTICS OF A SERVOACTUATOR FOR A PRIMARY FLIGHT CONTROL SYSTEM

The merits of the equalization control technique described in the previous paragraph have been assessed with reference to a typical fly-by-wire system for the control and actuation of a primary flight control surface of a medium-size aircraft. The system consists of two microprocessor

controlled electrohydraulic servoactuators with the main characteristics reported in table I.

Table I - Servosystem characteristics

| | |
|---|---------------------|
| Supply pressure | 28 MPa |
| Return pressure | 0.5 MPa |
| Hydraulic fluid conforming to MIL-PRF- 5606 | |
| Actuator stroke | 100 mm |
| Maximum external load | 25000 N |
| No-load speed | 100 mm/s |
| Total system inertia reflected to actuator | 90 kg |
| External damping coefficient | 10000 Ns/m |
| Stiffness of the actuator attachment point | 4×10^7 N/m |
| LVDTs excitation frequency | 3 kHz |
| Microprocessor recursion rate | 400 Hz |
| Microprocessor computation time | 1 ms |
| Analogue/digital converters resolution | 12 bit |

The design characteristics of the actuators and their components, and the system control law were defined to meet the requirements listed above. Extensive simulations were run for the ideal case of two servoactuators supplied with identical pressures and controlled by zero offset servoactuators; the results of these simulations were used as a benchmark for the performance of servoactuators with servoactuators exhibiting different offsets and for assessing the merit of the equalization control technique. The system response to different conditions was taken as representative of the system dynamic behaviour; these conditions were:

- no-load - frequency response for input commands of ± 0.1 mm (autopilot adjustments) and ± 2 mm (small amplitude pilot commands)
- no actuator command - dynamic stiffness for a load fluctuations of ± 500 N (level flight under turbulence) and ± 3000 N (level flight under gusts)
- no actuator command - half sine variation of load from 0 to 10000 N to 0 in 0.5 s (windshear).

6. DYNAMIC BEHAVIOUR OF SERVOACTUATORS WITH OFFSETS

Starting from the reference system with ideal servoactuators, a system consisting of actuators controlled by servoactuators with different offsets was analyzed. In particular, servoactuators with two opposite offsets corresponding to 10% of the rated current were considered, which case could well occur within the normal range of operating conditions. The dynamic behaviour of the system was assessed in response to the same input conditions considered for the ideal servoactuator. A system **without equalization** was first analyzed which showed as expected a large worsening of its dynamic characteristics, as clearly seen in Figures 9 through 12. When a small input command of ± 0.1 mm amplitude is given at a very low

frequency of 0.1 Hz (Figure 9a), a system with opposite servo valve offsets can respond to the command, though with a relatively large phase lag; however, if the command frequency is increased to 0.2 Hz (Figure 9b), the same system is practically not responding any longer to the small amplitude command. If the amplitude command is increased to ± 2 mm, the differences between systems with and without servo valve offsets become marginal, since the dead band in the combined pressure gain curve is negligible with respect to the command amplitude, and some differences show up only at high frequencies as it can be seen in Figure 10.

A very large difference in the system performance between the two conditions of zero servo valve offsets or maximum opposite offsets occurs for the dynamic stiffness. Since the typical frequency range for the loads fluctuations on the primary flight control surfaces is between 5 and 20 Hz, it can be seen from the diagrams of Figure 11 that a dramatic reduction of the dynamic stiffness up to 30 dB can be originated by the opposite servo valves offsets, which is clearly unacceptable.

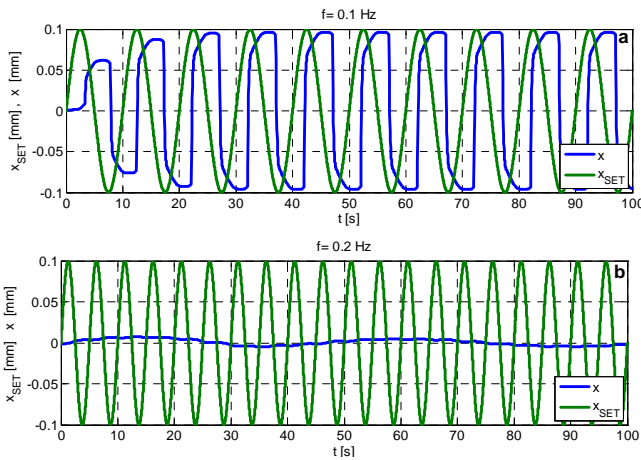


Figure 9 Servosystem without equalization: time response with no-load and input displacement of ± 0.1 mm
 (a) $f=0.1$ Hz and (b) $f=0.2$ Hz.

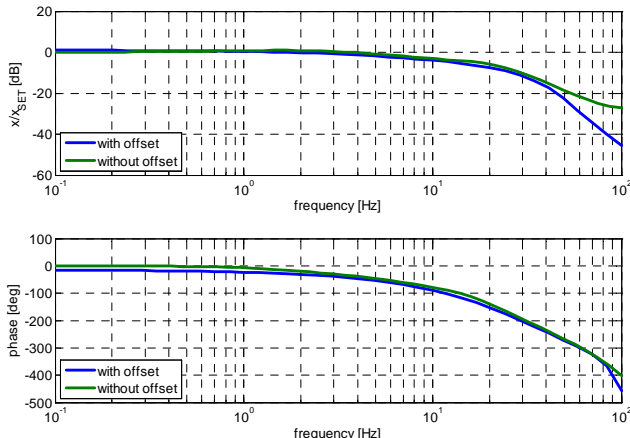


Figure 10 Servosystem without equalization: frequency response with no-load and input displacement of ± 2 mm.

This loss of dynamic stiffness is reflected into the system response to a strong gust, as shown in Figure 12. A system without offsets reacts with a minimum transient error, while a system with opposite servo valves offsets shows a large compliance and a transient disturbance up to 0.7 mm of actuators stroke.

A system **with pressure differential equalization** according to the strategy outlined at the end of paragraph 4 was then analyzed, and the system response to the different input conditions is illustrated in Figures 13 through 16. In particular, Figure 10 shows that no practical difference exists between the ideal system (no servo valve offset) and a system with maximum opposite servo valves offsets and differential pressure equalization; the curves for these two conditions are actually superimposed in the diagrams of Figures 13 and 14. Some minor difference exists in the response to a large gust (Figure 16), and the maximum transient position error is equal to 0.052 mm compared to 0.03 mm of the ideal system. However, this error is one order of magnitude lower than the error of a system with servo valve offset without differential pressure equalization, which is equal to 0.7 mm as it can be seen in Figure 12.

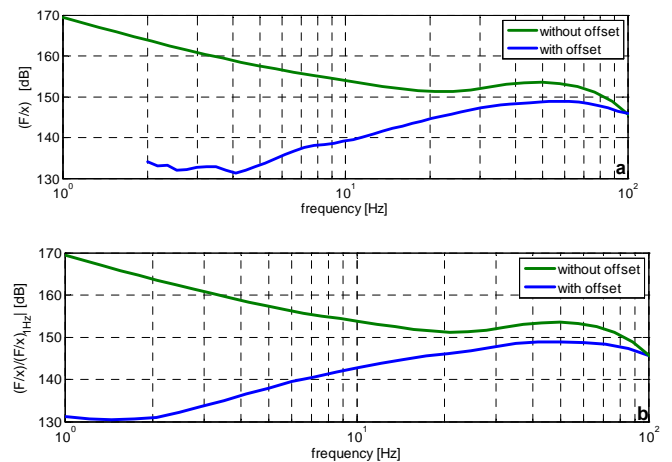


Figure 11 Servosystem without equalization: dynamic stiffness with eternal force (a) $R=\pm 500$ N and
 (b) $R=\pm 3000$ N. (Stiffness units are N/m).

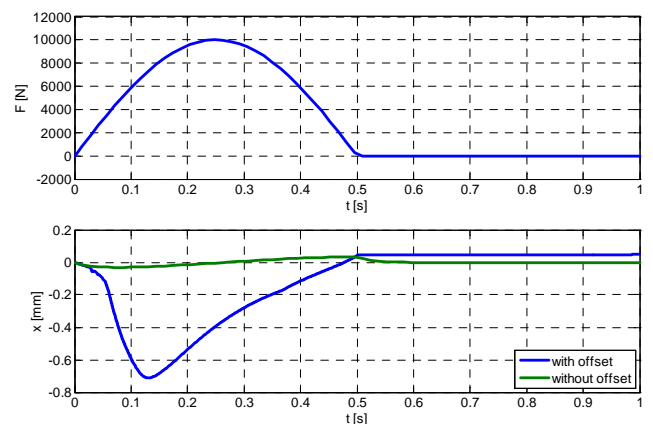


Figure 12 Servosystem without equalization: response to a half sine variation of load.

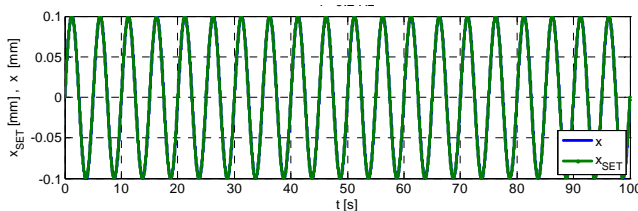


Figure 13 Servosystem with equalization: time response with no-load and input displacement of ± 0.1 mm at $f=0.2$ Hz.

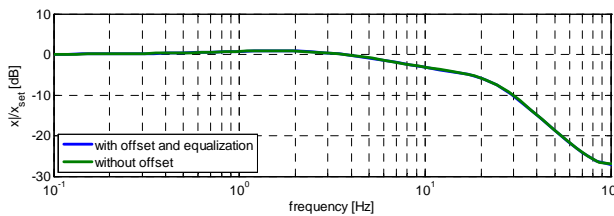


Figure 14 Servosystem with equalization: frequency response with no-load and input displacement of ± 2 mm.

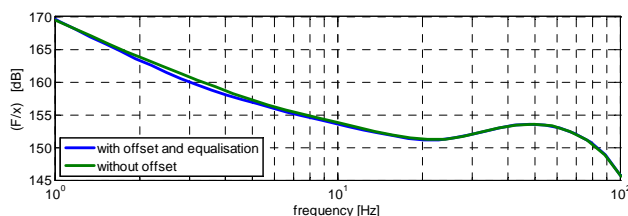


Figure 15 Servosystem with equalization: dynamic stiffness with external force $R=\pm 3000$ N. (Stiffness units are N/m).

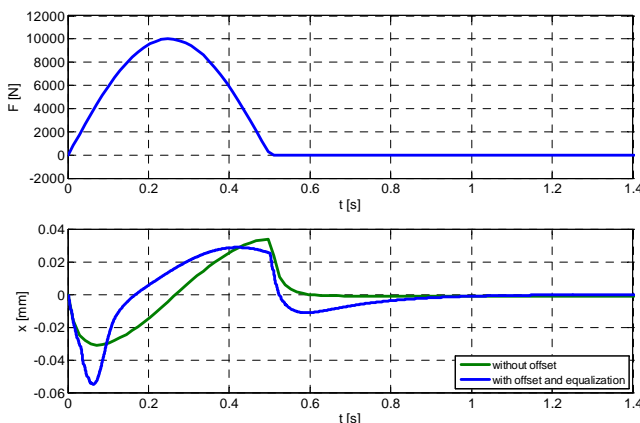


Figure 16 Servosystem with equalization: response to a half sine variation of load.

7 CONCLUSIONS

The research activity performed on the equalization techniques for dual redundant electrohydraulic servoactuators for aircraft flight controls showed that the implementation of a suitable control strategy permits to attain a good load sharing between two electrohydraulic servoactuators of the aerodynamic force acting on a flight control surface. By using in an appropriate way the signals provided by two pressure differential transducers it is possible to perform an effective compensation of variable servovalves offsets and to minimize the transient disturbances following a failure, which enables the use of servoactuators with a simple and less expensive architecture.

An accurate analytical model was prepared that clearly showed the merits of implementing the pressure differential equalization control algorithm.

REFERENCES

- [1] Thayer W.J. Redundant Electrohydraulic Servoactuators. Moog Technical Bulletin 127, May 1976.
- [2] Harschburger H.E. Development of Redundant Flight Control Actuation Systems for the F/A-18 Strike Fighter. SAE paper 831484, 1983.
- [3] Shafer W.S., Inderhees L.J. and Moynes, J.F. Flight Control Actuation System for the B-2 Advanced Technology Bomber. SAE paper 91112, 1991.
- [4] Straub, H.H. and Creswell R. The Boeing 747-400 Upper Rudder Control System with Triple Tandem Valve. SAE paper 912133, 1991.
- [5] Raymond E.T. and Chenoweth C.C. *Aircraft Flight Control Actuation System Design*. SAE, 1993.
- [6] Schmitt V.R., Morris, J.W. and Jenney G.D. *Fly-by-Wire*. SAE, 1998.
- [7] Van den Bossche D. A380 Primary Flight Control Actuation System. *Proceedings of the Int. Conference on Recent Advances in Aerospace Actuation Systems and Components*; Toulouse, France, June 2001.
- [8] Jacazio G. and Gastaldi L. Equalization techniques for dual redundant electrohydraulic servoactuators for flight control systems. *Proc. Fluid Power and Motion Control*, Bath (UK), pp. 543-557, 2008.

INSPECTION OF PRODUCTS BY MEANS OF COMPUTER VISUAL SYSTEM

Danica Janglová

Lubomír Uher

Institute of Informatics, Slovak Academy of Sciences, Bratislava, Slovakia

ABSTRACT

In this paper we present the results of application of the visual system in technological processes inspection. Principles of constructions of two different systems for data acquisition from real objects are described. The first method uses a 2D representation of the work scene snapped by CCD camera. The second method is based on 3D representation of the scene acquired by scanning the scene by structured light. Namely the light plane deflected by rotating mirror was used. For each position of the light plane a separate snap has been made by a CCD camera containing only a single spur of the light plane. Each snap was analysed separately. The 3D representation of the whole scene was obtained by superposition of all snaps.

Keywords: visual system, image processing, object recognition, depth map

1 INTRODUCTION

The visual information in various forms represents an important source of data acquired from the environment and its importance increases with the complexity of technological progress. The automatic recognition of objects present in an image may be used in technological processes as a base for decision. Visual inspection by humans represents a most important way to quality selection. In the mass production human factor represents an easy tired component and so the human inspectors become unreliable after few hours of work. That is the most important argument for development of pure computerised visual inspecting system with cameras as receptors of visual data and computer as an evaluating unit. The main adventure of the visual inspection is a nondestructive method of detection of defective products. Using the automated visual control is important not only for removing the tiresome monotonous work of human workers, but also for enhancing the reliability of the inspection. The main contribution to progress in digital processing of images is a new trend to produce cheap and high quality CCD cameras and fast

multiprocessor computers. Today the automatic visual inspection [3] propagates almost into each human activity. The object recognition problem represents a substantial and most complex part in inspection. Till now, it is not known the system able to recognize any object. There exist several specialised systems [10] for instance recognising defects on textile products, paper and photographic films, inspection of exactness of dimensions of some products of glass and ceramics, or quality of painting and processing of surfaces of cars. Producer [5] is testing fibreglass fabrics. The inspection is based on the data of defects and products sorting. Inspection phase is preceded by the learning phase. Roentgen inspection is used for inspection in multilayers electronics boards as well as inner heterogeneous inclusions in bulk materials. Here using the visual technics is important for protection of health of human operators. Another producer [15] operates on a continuous 190 cm wide band of the cord at the speed of 160 cm/sec for inspection of strings in tyres. The alarm is started when a preselected cue of defects were found. Namely interesting defects are broken ends of strings, structural defects (picks), released or deformed strings. In fabrics and paper production, e.g. photomedia, in running belt of material linear sensors application prevail. There are single row or multi row linear sensors. Multi row sensors are usually combined with optical colour filters distinguishing several thousands of colors. Four rows are frequently used to get three color components and lighting information in a single step [1].

Contact author: Danica Janglová

Institute of Informatics
Dúbravská cesta 9, 845 07 Bratislava, Slovakia
E-mail: Danica.janglova@savba.sk

Our aim was to suggest and develop a system capable to find out defective spots on the surface of rubber products, namely slide less rubber carpets. After consulting the final user we stated a problem as follows: The subject to inspection should be a one meter wide rubber carpet with slide less coin formed design. The detection of defects should distinguish approximately 25 different kinds of defects and it should register and finally print out the exact positions and densities of defects within the roll of the final product.

In section 2 we describe shortly our design and solution of this visual control system. Methods of data acquisition and processing of the image will be analysed in section 3 with giving some examples.

2 VISUAL SYSTEM IN INDUSTRIAL APPLICATION

The aim of our project was suggesting a control apparatus, which should work on a basis of computer visual system. Its aim is inspection of the surface of rubber products, namely the surface of rubber anti slide carpets for floor covers in humans transport means as busses and trains. Consulting with final user namely special coin formed design of carpets was selected as an example of experimental inspection.

This intention lead to solution of particular tasks as follows:

Preparation part: the possible different types of defects must be defined exactly and represented in a form of template images. From experience of industrial workers and controllers 25 defects were defined as given in [7]. There are e.g. bubbles, faldings, dimensional deflection, colour deviations, holes, wavy edges, chemicals, broken sites and so on as shows the Figure 4.

Construction part: there must be made a suggestion of visual system, selection of proper cameras, construction of illuminating equipment and all hardware equipment. For evaluation of defects using CCD camera as an input sensor the following possibilities were analysed: Scanning the surface using one moveable CCD camera placed close to the surface of carpet using more fix positioned cameras across the width of carpet or one high resolution CCD camera or linear one row sensor placed across the conveyor belt with running rubber carpet.

Theoretical part: an algorithm must be created distinguishing separate kinds of defects. The solution of problem should include most modern methods of visual information processing, new algorithms and original programs. Many methods and algorithms for object recognition [4], [6], [8], [14] were studied.

Software part: we checked programs for data acquisition, evaluation and objects recognition. These programs were included in a packet of cooperating system of object-oriented subprograms including set of information and instructions for final user, a set of testing programs for verification of technical means and a dynamical library of fundamental object oriented functions and methods. A

demo program enables calling and verification of all functions of the whole system, signalising all possible failures of the system or its components. It should be able of archiving history of all running tests, including help system.

Experimental part: in this part the verification of abilities of the system using pre processed templates of defects, as supplied by the final user. Then computer simulation was done. The program packet was tested using static set of templates representing different types of defects at laboratory conditions. Its application as automated identification and localization of defects should aim the more reliable and effective statistics of all types of defects, their frequencies of appearance excluding completely the human factor. Categorization and statistical processing of defects, sorted by their types and successive the more objective dividing the final products into a prescribed number of quality classes.

Experiences with the system may lead to application of similar systems in other resorts of industrial production.

3 METHODS OF THE IMAGE PROCESSING

3.1 GENERAL CONCEPT

Visual system is a complex system including visual sensor and computerised automatic operating set of methods and programs used for image analysis. Its aim is immediate visualization of work scene. Computer vision usually means a visual system with the set of methods and programs used for digital image processing running on a computer [4].

The basic model of digital image processing is presented on Figure 1. From a rough image the unit of preprocessing transforms the input visual information, extracts information into a form enabling easier classification of objects, using categorization by means of selected and computed features of objects. Such a form of image transform, which makes easier the succession deeper analysis and object recognition, represents image preprocessing.

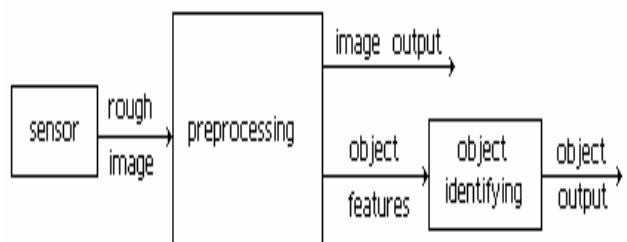


Figure 1 Digital image processing.

3.2 METHODS OF PREPROCESSING OF 2D IMAGE

In our case the aim of automated visual inspection is a nondestructive detection of defects on the surface of rubber products and obtaining complex quantitative information on the products for statistical processing purposes. The method we have developed depend on circumstances and as a rule it must be adapted to each environment and situation. In following let us introduce an algorithm used for extraction of defective parts of tested product. At the work space the rough image of working scene is snapped by CCD camera. Correction of distortions of optical system, obtaining the image close to the ideal image of the scene was done using simple calibration images, finding and correcting optical distortions. Then signal processing is applied, aiming the representation of image in a form of a depth map, used in subcessive automated measurements of dimensions and distances. In the 2D based system the whole process consists of following steps: The rough image as seen by CCD camera, see Figure 2, is transported into the memory of PC.

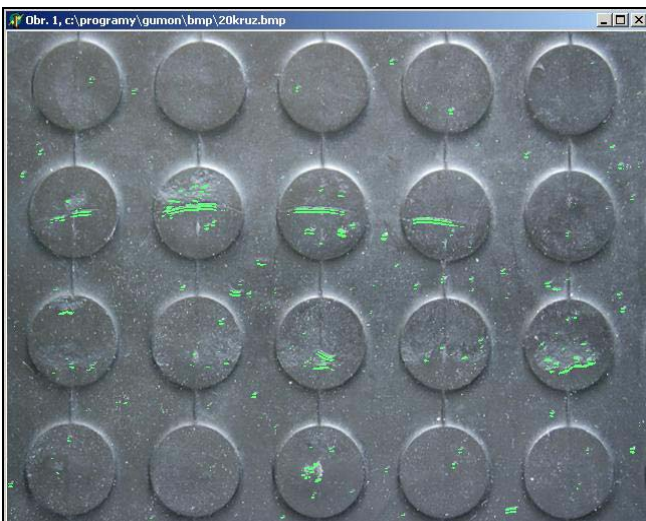


Figure 2 An image of tested product.

The routines of image pre processing follow. At first the multilevel grey scale figure is generated from a color rough image. Digital filtration enhances edges present in the image. Skewed illumination has as a result an incomplete image, so it is inevitable to complete the images of edges. For completion of images of circles and ribbons of the rubber carpet surface structure method of least squares was applied. After the last step the complete structure appears. It must be now extended by a small security reserve. Sorting the figures of circles by X or by Y coordinates; it is possible to obtain coordinates of extreme points X_{max} , X_{min} , Y_{max} , and Y_{min} , and coordinates of points of gravity of all circles. Now it is possible to remove glaze effects resulting from a skewed illumination. Then *thresholding* removes a substantial part of the noise.

The image is now prepared for cluster analysis. Then second thresholding is used to remove the clusters with sub limits dimensions. Cluster analysis was used for separation of image of defects on a real product. This method also reduces a noise background. Some products are better legible in 3D representation as spatial objects. By Besl [2] the depth information may be obtained indirectly from local changes of illumination, from which the curvatures of surface may be also calculated. We found this method as unreliable.

The number of remaining clusters is in a direct correspondence with the number of defects, present on the analysed part of surface. Now it is possible to apply a Boolean function XOR onto the images of real sample and image of ideal, defect-free sample. We obtained now the figure of defects only, as is shown in Figure 3. The relative quantity of appearance of different defects cluster analysis was used [9]. The number of clusters in tested piece and in defect less template should be zero, when testing the defect less sample canonical correlation method.

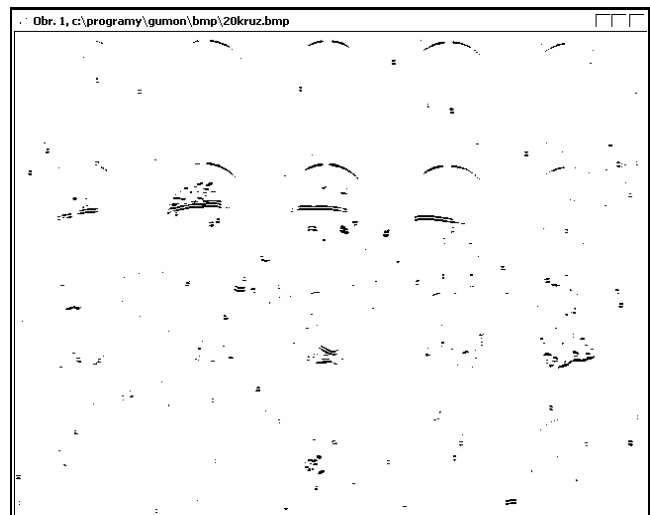


Figure 3 Defects on the tested product.

For sorting purposes a cluster analysis was applied. It is capable of finding the number of objects appearing on a scene in relative short time. The cluster analysis combined with a normalised histogram gives information of dimensions and of relative appereance of objects present in the image. The number of clusters is proportional to a number of defects found in a given snap.

In Figure 4 templates of typical defects are presented: defectless sample, filth on a surface, heterogeneous imprints, breakdowns, bubbles, waves, holes, worn spots, rough latex and chemicals. Preprocessing of templates was done by numerical filtering using edge operators, as seen in Figure 5.

In the next step analysis of types of defects must be done. The way to do it depends in comparison of the normalised histograms. It is a last step, when parameters characterising

the different defects are calculated and compared to the corresponding parameters of defect in the templates. The phase of classification is based on the analysis of resemblances, giving the type of defect as a result. The results are marked into an output statistics of defects.

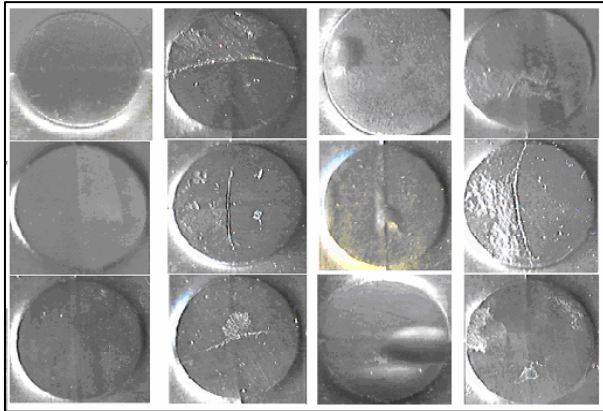


Figure 4 A survey of typical defects.

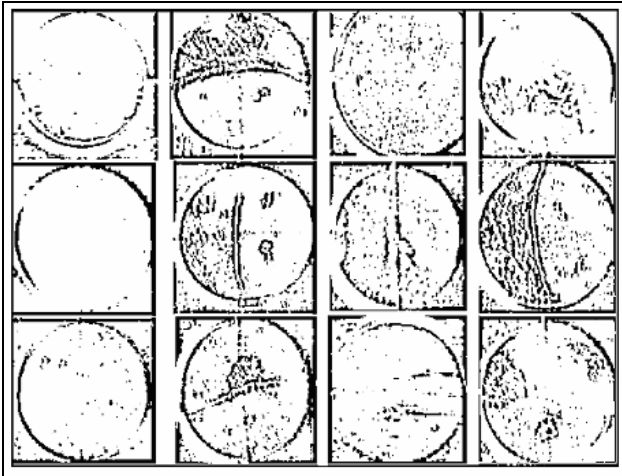


Figure 5 Image processing of the previous defects.

3.3 Methods of 3D object recognition

More reliable are methods using a structured light in form of dots or light planes, strips or moiree. Each cut of the scene by the light plane must be analysed separately, and the method is very slow, several minutes per one scene. Several hundreds of snaps are inevitable to reach good spatial resolution.

In our experimental 3D scanner we used a rotating mirror for positioning the light plane in up to 256 positions giving cca 1 mm resolution on a scene 30x30 cm and 30 cm in depth. It took 20 minutes for one scene analysis [11].

There exist many different ways of moving the structured light planes or spots by electrooptics and electromagnetic systems. In our experiment we used a computer controlled stepping motor. Wahl [12] used mechanic changes of optical masks. Very interesting is a method using a

cuneiform optical filter with graded transparency. It generates the intensity modulated light structure and the image of the whole scene is coded in only two steps: first snap done with the filter and the second one without the filter.

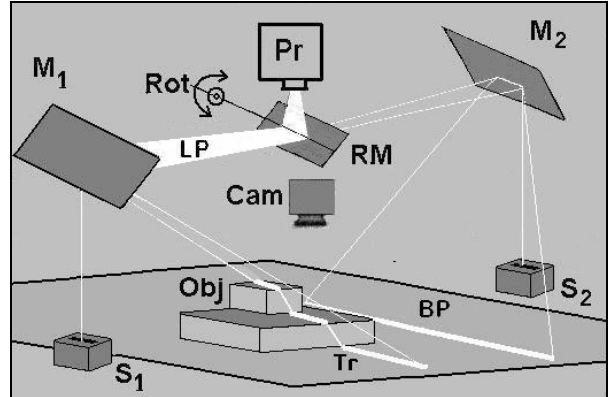


Figure 6 The 3D scanner with light plane.

The depth map is a function $z(x,y)$. In the computer memory the information of 3D scene is accumulated in a form of two dimensional field $Z(x,y)$, where at each (x,y) point the corresponding z coordinate (depth) is saved. For depth map acquisition the scanning method was chosen for its great accuracy and simple construction see Figure 6. The method is extensive, requires run conditions without time limitations. In principle it operates on a triangulation, the projector projects a light plane LP onto the scene under a known impact angle α . The "base," distance b is measured from the focus F_p of projector objective to the optical axis of camera. The camera focus is F_c , its relative position to the base plane BP is z_o . The light plane is an image of a narrow gap in opaque diaphragma projected by projector Pr onto the scene. It is deflected by the rotating mirror RM , so that the impact angle α may be continuously varied. Thus scanning of the scene is performed. For moving the light plane we used a PC controlled stepping assembly Rot rotating the mirror RM . The two static mirrors M_1, M_2 were used to reflect the LP onto the scene from two different directions, reducing thus the screened parts of testing objects. The end position sensors S_1, S_2 are used for calibration purposes and for exact stating the start and end positions of the movement of light plane.

The 3D map acquisition was divided into following steps: At a given position of light plane an image was snapped by camera. The intensity image of the snap was analysed for continuity of a trace of light plane. The break points of the trace were analysed and depth was calculated from the simple triangulation equation.

Spatial transformations were inevitable in order to obtain the representation of 3D objects (Figure 7) in the inner 2D camera coordinate system, as described in more details in [11]. The point to point transformations were performed in matrix form. The results of depth analysis are seen in Figure 8.

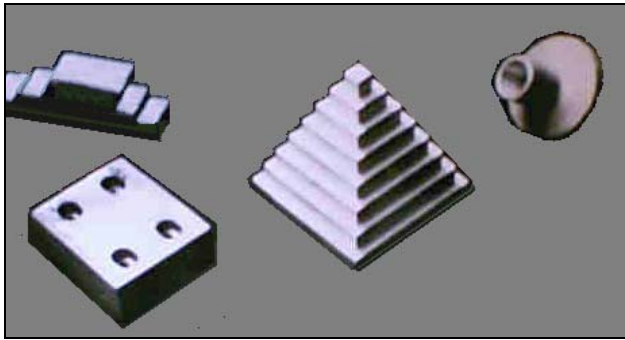


Figure 7 Testing objects.

In the Figure 8 the resulting 3D image was rotated by 180 degrees azimuth angle to show “black regions,, invisible for camera.

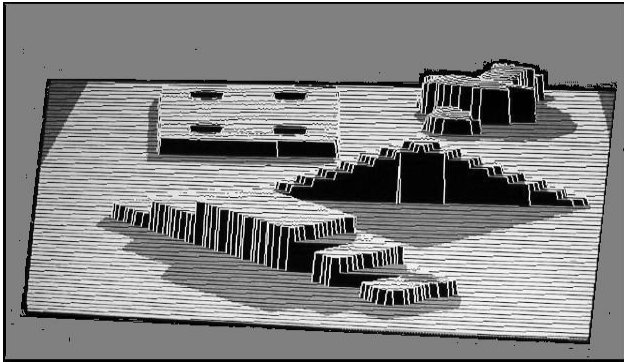


Figure 8 The depth map image.

Note, that for the whole back-half of the pyramid the depth information is missing, so that reconstruction of the invisible pyramid's back side failed. Two bundles system using reflections from two mirrors M_1, M_2 according to Figure 6 was designed for reduction of the screened parts of a scene.

The triangulation method, Figure 9, F_c camera objective focus, F_p projector focus, d depth, α angle, $\Delta\alpha$ angular increment error, Δd depth error. In principle the depth information d is calculated from image data making use of triangulation formula (1)

$$b \tan(\alpha) = z_o + d \quad (1)$$

Triangulation method uses base b and angle α , HK represent the surface of the object, Z is a point sectioned by one light beam of the light plane on the base plane of the scene, ξ is a depth or “height” of the object HK above the base plane. The image of a distance HK is measured directly in pixels on an intensity image of the scene in a CCD camera. Then following relation (2) is valid in camera frame of reference

$$\xi = const \cdot HK \tan(\alpha) \quad (2)$$

where $const$ is a calibration constant. For output transformation of data is inevitable from camera to scene frame of reference. The more detailed description of apparatus, calibration techniques and transformation of data was given in [11] where also more detailed references may be found.

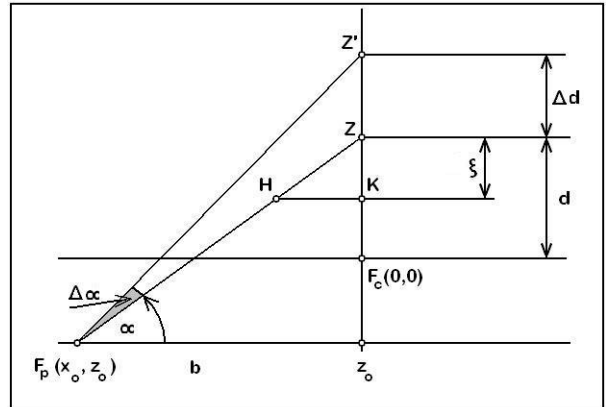


Figure 9 The triangulation method.

For calibration of camera and visual system Tsai's ideas were used [13] with some limitations. When automated calibration takes place, a singularity appears at the optical axis of the objective, chosen as a polar axis of spherical coordinates.

4 CONCLUSION

In the paper principles of constructions of two different systems are described. The first method uses a 2D representation of the work scene snapped by CCD camera. The method was used for searching the defects of periodic structures on surfaces of rubber carpets. The types of defects to be found were defined by producer in the form of templates. The image of a real rubber product was pre-processed by digital filtering and then analysed making use of clustering method. Substantial simplification of the analysed image was reached by subtraction of the ideal image of the defects free product from the real image. Thus only defective elements appeared in the resulting image and they were compared with the templates. The second method is based on 3D representation. By scanning the scene with the mobile light plane 3D representation is obtained. A projector with a narrow gap diaphragma produced the light plane. The light plane was deflected by means of mirror rotated by stepping motor. For each step the CCD camera made the extra snap. Each snap was analysed separately, using triangulation principles. After the analyses of all steps were finished, the whole set of images was added together so that it gave a 3D representation of the scene. The two static mirrors system were used for reduction of screened parts of objects, which are invisible for CCD camera when scene were illuminated from one side only.

REFERENCES

- [1] Benjema R., Schmitt F., *Fast Global Registration of 3D Sampled Surfaces Using a Multi-z-buffer technique*. Image and Vision Computing, Vol 17 (2), 1999, pp. 113-123.
- [2] Besl P.J., Jain R.C., *Three Dimensional Object Recognition*. Computing Surveys. Vol 17 (1), 1985, pp. 75-145.
- [3] Roland T.Chin, Survey. Automated Visual Inspection. *Comp.Vision Graph.Image.Proc..* 41, pp. 346-381, 1988.
- [4] Gonzalez R., C., Wintz P., *Digital Image Processing*. Addison – Wesley Publishing Company, Reading, Massachusetts, 1987.
- [5] info@evs.co.il
- [6] Jähne B., *Practical Handbook on Image Processing for Scientific Applications*. CRC Press, Boca Raton New York, 1997.
- [7] Janglová D., Britaňák V., Uher L., Považan I., Automated Inspection of Industrial Products by Computerised Visual System, Bratislava, 2003 (in slovak).
- [8] Jaroslavskij L., Bajla I., *Metódy a systémy číslicového spracovania obrazov*. Alfa, Bratislava, 1989.
- [9] Rao R.C., *Linear Statistical Inference and its Applications*. John Wiley&Sons, New York, USA, 1973.
- [10] Sorwar G., Abraham A., Dooley L. S., Texture Classification Based on DCT and Soft Computing. www.infotech.monash.edu.au
- [11] Sefcik. T., Uher L. Kopca T., Gemeranova E., Depth Map Acquisition in Laboratory Conditions. LRA, Vol. 6, 1995, pp. 223-228.
- [12] Wahl F.M., *A coded light approach for 3D vision*. IBM Research Report RZ 1452, 1984.
- [13] Wang C.C., Extrinsic Calibration of a Vision Sensor Mounted on a Robot. *IEEE Trans. on Rob. And Automation*, Vol. 8, no. 2, 1992.
- [14] Webb A., *Statistical Pattern Recognition*. Arnold, London, 1999.
- [15] www.sheltonmachines.co.uk

TEMPLATE FOR PREPARING PAPERS FOR PUBLISHING IN INTERNATIONAL JOURNAL OF MECHANICS AND CONTROL

Author1* Author2**

* affiliation Author1

** affiliation Author2

ABSTRACT

This is a brief guide to prepare papers in a better style for publishing in International Journal of Mechanics and Control (JoMaC). It gives details of the preferred style in a template format to ease paper presentation. The abstract must be able to indicate the principal authors' contribution to the argument containing the chosen method and the obtained results. (max 200 words)

Keywords: keywords list (max 5 words)

1 TITLE OF SECTION (E.G. INTRODUCTION)

This sample article is to show you how to prepare papers in a standard style for publishing in International Journal of Mechanics and Control.

It offers you a template for paper layout, and describes points you should notice before you submit your papers.

2 PREPARATION OF PAPERS

2.1 SUBMISSION OF PAPERS

The papers should be submitted in the form of an electronic document, either in Microsoft Word format (Word'97 version or earlier).

In addition to the electronic version a hardcopy of the complete paper including diagrams with annotations must be supplied. The final format of the papers will be A4 page size with a two column layout. The text will be Times New Roman font size 10.

Contact author: author1¹, author2²

¹Address of author1.

²Address of author2 if different from author1's address.

2.2 DETAILS OF PAPER LAYOUT

2.2.1 Style of Writing

The language is English and with UK/European spelling. The papers should be written in the third person. Related work conducted elsewhere may be criticised but not the individuals conducting the work. The paper should be comprehensible both to specialists in the appropriate field and to those with a general understanding of the subject. Company names or advertising, direct or indirect, is not permitted and product names will only be included at the discretion of the editor. Abbreviations should be spelt out in full the first time they appear and their abbreviated form included in brackets immediately after. Words used in a special context should appear in inverted single quotation mark the first time they appear. Papers are accepted also on the basis that they may be edited for style and language.

2.2.2 Paper length

Paper length is free, but should normally not exceed 10000 words and twenty illustrations.

2.2.3 Diagrams and figures

Figures and Tables will either be entered in one column or two columns and should be 80 mm or 160 mm wide respectively. A minimum line width of 1 point is required at actual size. Captions and annotations should be in 10 point with the first letter only capitalised *at actual size* (see Figure 1 and Table VII).

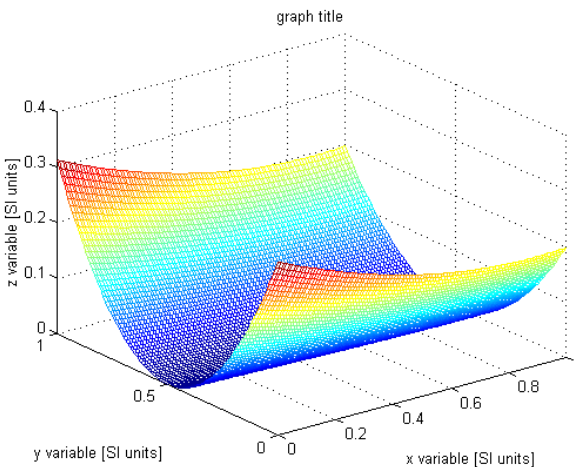


Figure 1 Simple chart.

Table VII - Experimental values

| Robot Arm Velocity (rad/s) | Motor Torque (Nm) |
|----------------------------|-------------------|
| 0.123 | 10.123 |
| 1.456 | 20.234 |
| 2.789 | 30.345 |
| 3.012 | 40.456 |

2.2.4 Photographs and illustrations

Authors could wish to publish in full colour photographs and illustrations. Photographs and illustrations should be included in the electronic document and a copy of their original sent. Illustrations in full colour ...

2.2.5 Equations

Each equation should occur on a new line with uniform spacing from adjacent text as indicated in this template. The equations, where they are referred to in the text, should be numbered sequentially and their identifier enclosed in parenthesis, right justified. The symbols, where referred to in the text, should be italicised.

- point 1
 - point 2
 - point 3
1. numbered point 1
 2. numbered point 2
 3. numbered point 3

$$W(d) = G(A_0, \sigma, d) = \frac{1}{T} \int_0^{+\infty} A_0 \cdot e^{-\frac{d^2}{2\sigma^2}} dt \quad (1)$$

3 COPYRIGHT

Authors will be asked to sign a copyright transfer form prior to JoMaC publishing of their paper. Reproduction of any part of the publication is not allowed elsewhere without permission from JoMaC whose prior publication must be cited. The understanding is that they have been neither previously published nor submitted concurrently to any other publisher.

4 PEER REVIEW

Papers for publication in JoMaC will first undergo review by anonymous, impartial specialists in the appropriate field. Based on the comments of the referees the Editor will decide on acceptance, revision or rejection. The authors will be provided with copies of the reviewers' remarks to aid in revision and improvement where appropriate.

5 REFERENCES (DESCRIPTION)

The papers in the reference list must be cited in the text. In the text the citation should appear in square brackets [], as in, for example, “the red fox has been shown to jump the black cat [3] but not when...”. In the Reference list the font should be Times New Roman with 10 point size. Author's first names should be terminated by a ‘full stop’. The reference number should be enclosed in brackets.

The book titles should be in *italics*, followed by a ‘full stop’. Proceedings or journal titles should be in *italics*. For instance:

REFERENCES (EXAMPLE)

- [1] Smith J., Jones A.B. and Brown J., *The title of the book*. 1st edition, Publisher, 2001.
- [2] Smith J., Jones A.B. and Brown J., The title of the paper. *Proc. of Conference Name*, where it took place, Vol. 1, paper number, pp. 1-11, 2001.
- [3] Smith J., Jones A.B. and Brown J., The title of the paper. *Journal Name*, Vol. 1, No. 1, pp. 1-11, 2001.
- [4] Smith J., Jones A.B. and Brown J., *Patent title*, U.S. Patent number, 2001.

International Journal of Mechanics and Control – JoMaC
Published by Levrotto&Bella
TRANSFER OF COPYRIGHT AGREEMENT

NOTE:
Authors/copyright holders are asked to complete this form signing section A, B or C and mail it to the editor office with the manuscript or as soon afterwards as possible.

Editor's office address:
Andrea Manuello Bertetto
Elvio Bonisoli
Dept. of Mechanics
Technical University – Politecnico di Torino
C.so Duca degli Abruzzi, 24 – 10129 Torino – Italy
e-mail: jomac@polito.it
fax n.: +39.011.564.6999

The article title:

By: _____

To Be Published in *International Journal of Mechanics and Control JoMaC*
Official legal Turin court registration Number 5320 (5 May 2000) - reg. Tribunale di Torino N. 5390 del 5 maggio 2000

- A Copyright to the above article is hereby transferred to the JoMaC, effective upon acceptance for publication. However the following rights are reserved by the author(s)/copyright holder(s):
1. All proprietary rights other than copyright, such as patent rights;
2. The right to use, free or charge, all or part of this article in future works of their own, such as books and lectures;
3. The right to reproduce the article for their own purposes provided the copies are not offered for sale.

To be signed below by all authors or, if signed by only one author on behalf of all co-authors, the statement A2 below must be signed.

A1. All authors:

SIGNATURE_____ DATE_____ SIGNATURE_____ DATE_____

PRINTED NAME_____ PRINTED NAME_____

SIGNATURE_____ DATE_____ SIGNATURE_____ DATE_____

PRINTED NAME_____ PRINTED NAME_____

A2. One author on behalf of all co-authors:

"I represent and warrant that I am authorised to execute this transfer of copyright on behalf of all the authors of the article referred to above"

PRINTED NAME_____

SIGNATURE_____ TITLE_____ DATE_____

B. The above article was written as part of duties as an employee or otherwise as a work made for hire. As an authorised representative of the employer or other proprietor. I hereby transfer copyright to the above article to Editel-Pozzo Gros Monti effective upon publication. However, the following rights are reserved:

1. All proprietary rights other than copyright, such as patent rights;
2. The right to use, free or charge, all or part of this article in future works of their own, such as books and lectures;
3. The right to reproduce the article for their own purposes provided the copies are not offered for sale.

PRINTED NAME_____

SIGNATURE_____ TITLE_____ DATE_____

C. I certify that the above article has been written in the course of employment by the United States Government so that no copyright exists, or by the United Kingdom Government (Crown Copyright), thus there is no transfer of copyright.

PRINTED NAME_____

SIGNATURE_____ TITLE_____ DATE_____

CONTENTS

3 Robots Driven by Parallel Bicycles

K. Yamafuji, M.Q. Feng, T. Kawamura

13 Locomotion Performance Evaluation of an All-Terrain Rover

M.M. Foglia, G. Reina

27 Input Shaping for Slosh-Free Moving Containers with Liquid

P. Hubinský, T. Pospiech

35 Improving the Dynamic Performance of Redundant Electrohydraulic Servoactuators

G. Jacazio, L. Gastaldi

47 Inspection of Products by means of Computer Visual System

D. Janglová, L. Uher

next number scheduled titles:

A Three-Step Procedure for the Modelling of Human Diarthrodial Joints

R. Franci, V. Parenti-Castelli, N. Sancisi

Workspace Enlargement Merging Assembly Modes. Application to the 3-RRR Planar Platform

E. Macho, O. Altuzarra, V. Petuya, A. Hernandez

Lot Size One in the Mass Production and Precision Assembly of Cylinder Locks

W. Mann, G. Peschl, A. Sieber, C. Wögerer.

Calibration and Testing Issues of the Vision, Inertial Measurement and Control System of an Autonomous Indoor Quadrotor Helicopter

L. Kis, Z. Prohaszka, G. Regula

Fractional-Order Derivatives and their Application to the Position Control of Robots

L. Bruzzone, G. Bozzini.

Robotics Techniques for Data Acquisition in Underwater Archeology

G. Conte, S. M. Zanoli, D. Scaradozzi, A. Caiti, L. Gambella